2017

Studies of Hydrogen Defects and Free-Carrier Absorption in Transparent Conducting Oxides using Fourier Transform Infrared Spectroscopy

Philip Michael Weiser
Lehigh University

Recommended Citation

Weiser, Philip Michael, "Studies of Hydrogen Defects and Free-Carrier Absorption in Transparent Conducting Oxides using Fourier Transform Infrared Spectroscopy" (2017). *Theses and Dissertations*. 2872.
http://preserve.lehigh.edu/etd/2872

Studies of Hydrogen Defects and Free-Carrier Absorption in Transparent Conducting Oxides using Fourier Transform Infrared Spectroscopy

by

Philip M. Weiser

A Dissertation

Presented to the Graduate and Research Committee

of Lehigh University

in Candidacy for the Degree of

Doctor of Philosophy

in

Physics

Lehigh University

May 2017

Certificate of Approval

Approved and recommended for acceptance as a dissertation in partial fulfillment of the requirements for the degree of Doctor of Philosophy in Physics.

Philip M. Weiser

"Studies of Hydrogen Defects and Free-Carrier Absorption in Transparent Conducting Oxides using Fourier Transform Infrared Spectroscopy"

Defense Date

Dr. Michael J. Stavola
Dissertation Director, Chair

Approved Date

Committee Members

Dr. W. Beall Fowler
Member

Dr. Gary DeLeo
Member

Dr. Ivan Biaggio
Member

Dr. Gregory S. Ferguson
External Member (Dept. of Chemistry)

Acknowledgements

I cannot believe that the journey towards my Ph.D. is finally complete. There are no words that describe how grateful I am for the support from my family, friends, and mentors during this journey. I hope these acknowledgements will convey my gratitude to all of the individuals who have supported me over years.

First, I would like to thank my advisor, Michael Stavola. Michael has taught me so much about research in condensed matter physics and vibrational spectroscopy, and I will never forget his guidance, patience, and perfectly-timed pieces of advice ("If you have time to do it fast, you better have time to do it twice."). I am very fortunate to have had him as an advisor and a mentor. Second, I would like to thank my "co-advisor", Beall Fowler. Beall's theoretical calculations have been invaluable for the interpretation of my experimental data. I am also very grateful to the three remaining members of my Ph.D. committee: Gary DeLeo, Ivan Biaggio, and Gregory Ferguson, for all of their thoughtful comments, questions, and conversations.

In addition to my Ph.D. committee, I am fortunate to have had many mentors, at both Lehigh University and Moravian College, who were always willing to talk with me about my teaching and/or research struggles. My thanks goes out to them for their time. I would especially like to thank Kathleen Hutnik for helping me grow as a leader during my service on the Graduate Student Senate.

I am lucky to have known and worked with many excellent graduate students. While there are far too many to fit in these acknowledgements, there are several individuals who deserve recognition. Both Figen Bekisli and Weikai Yin trained me how to operate the Bomem spectrometer, and Weikai was an outstanding collaborator for the indium oxide experiments. Ying Qin has been an excellent research partner and a good friend, and I wish her the best of luck as she finishes her dissertation over the next year. I would also like to acknowledge Vinnie Zoutenbier, Natalie Hernandez, Jason Haaga, Michael Erickson, and Thienbao Nguyen for their constant support. I would like to thank Vinnie specifically for editing select chapters from this dissertation.

None of this work would have been possible without the support and love of my family. I would like to thank my parents, Michael and Wanda Weiser, my parents-in-law, Jeff and Agnes Haddad, my aunt, Marybeth McAfee, and my cousin, Ciara McAfee.

Last, but certainly not least, I want to thank my wife, Dr. Gaby Haddad-Weiser. I would never have made it to this point without your constant love and encouragement. Thank you for making sure I stayed sane during this last year! It means a lot to me that we are closing the Lehigh chapter of our lives together, and I cannot wait to see what comes next.

Table of Contents

List of Figures

List of Tables

Abstract

Transparent conducting oxides (TCOs) are wide-band-gap, metal-oxide semiconductors that combine high electrical conductivity with transparency to visible light. These properties have made TCOs attractive candidates for many optoelectronics applications. Although the origin of the conductivity of TCOs has traditionally been attributed to native defects such as oxygen vacancies and cation interstitials, theoretical calculations show that these defects are deep-level defects and therefore cannot be responsible for the *n*-type conductivity. Recent reports have shown that hydrogen, often incorporated unintentionally into the sample during crystal growth, acts as a shallow donor and is likely a source of the unexpected conductivity. Understanding the physical and chemical properties of hydrogen-related defects in these materials is vital for controlling the conductivity, and for the continued development of transparent electronic devices.

Fourier Transform Infrared (FTIR) spectroscopy is a powerful tool for studying the vibrational properties of hydrogen-related defects in semiconductors, and can reveal information about the atomic composition, microscopic structure, and thermal stability of a defect. Measurement of the absorption in the IR spectral region due to free carriers provides a contact-free method for probing the electrical conductivity of a material. This dissertation presents three different studies of defects in TCOs.

Experimental methods were developed to quantitatively measure the transmission spectra of materials in the near-infrared and mid-infrared spectral regions at different temperatures using an FTIR spectrometer. This technique was used to study the free

carrier absorption and the carrier scattering mechanisms in *n*-type, hydrothermally grown, ZnO single crystals.

Previous IR studies have assigned the 3306 cm^{-1} O-H vibrational line observed in as-grown and hydrogenated In_2O_3 single crystals to the interstitial hydrogen shallow donor (H_i^+). Polarized IR absorption measurements of In_2O_3 single crystals under [001] and [110] uniaxial stresses reveal that the H_i^+ defect has [110] monoclinic symmetry, which is consistent with that predicted by theory. A stress-induced alignment has been observed in samples under [001] stress. The reorientation process giving this alignment corresponds to a diffusion jump. The combination of diffusivities determined at low temperature from uniaxial stress experiments and high temperatures from bulk out-diffusion experiments (Ying Qin) reveal the diffusivity of H_i^+ across 10 decades.

Monoclinic gallium oxide ($\beta\text{–}Ga_2O_3$) is a TCO that has received renewed interest due to its large band gap of 4.9 eV, which makes it transparent at ultra-violet wavelengths. Hydrogenated $\beta\text{–}Ga_2O_3$ samples show a strong O-H vibrational line at 3437 cm^{-1} comprising two equivalent hydrogens. The line has a high thermal stability (~ 900 °C) and exhibits interesting polarization properties. The combination of experimental data and first principles calculations using CRYSTAL06 suggest that the 3437 cm^{-1} O-H line originates from a gallium vacancy complexed with two hydrogens.

Chapter 1

Introduction

1.1: Defects in Semiconductors

> *"One shouldn't work on semiconductors, that is a filthy mess; who knows whether any semiconductors exist." – Wolfgang Pauli*

Semiconductors are an incredibly versatile group of materials that are primarily responsible for the technological advances seen in the last 60 years. As the name suggests, the properties of a "semi" conductor fall between those of an insulator and a conductor. The ability to vary the electrical conductivity over 12 orders of magnitude *and* maintain control of the conductivity has made semiconductors indispensable in modern technology. Semiconductors are the basis for many electronic and optoelectronic devices: diodes, transistors, LEDs, laser diodes, and detectors, to name a few.[1]

The defining characteristic of a semiconductor is its band gap, which is the energy difference between the highest energy completely occupied band (valence band) and the lowest energy completely unoccupied band (conduction band). Pure, or intrinsic, semiconductors are insulators. Control over the conductivity of a semiconductor is typically obtained by adding impurity atoms that contain one additional or one fewer electron than the host atom to the crystal. This process, referred to as doping, has been highly successful in creating semiconductors that are conductive at room temperature because they contain either an excess (*n*-type) or a deficiency (*p*-type) of electrons. Atoms that promote *n*-type conductivity are called donors, and atoms that promote *p*-type conductivity are called acceptors. An impurity atom substituting for an atom of the host crystal is just one example of the many types of defects, or imperfections, which can occur in a material.

The presence of one type of defect or several types of different defects can have profound effects on the physical and chemical properties of a material. The substitutional impurities discussed above that lead to *n*-type or *p*-type conductivity need only to be present with a concentration of one impurity atom for every million host atoms to vary the electrical conductivity by orders of magnitude.

Although defect formation increases the enthalpy of the crystal , the configurational entropy of the crystal is increased by its presence, which results in a net decrease in the total free energy of the crystal. In other words, defects are unavoidable and will always be present in materials.

The simplest types of defects, point defects, come in several different forms. Vacancies are created when host atoms are removed from the host crystal. For crystals composed of two or more types of host atoms, anti-sites refer to one atom occupying a lattice site that is normally occupied by a different atom. Substitutional defects are created when an impurity replaces a host atom at a normal lattice site. Impurities that incorporate at sites that are not normally occupied by a host atom are called interstitial defects. Intrinsic, or native, defects refer to those that are created by atoms that belong to the host crystal. For example, vacancies, anti-sites, and interstitial defects of oxygen and zinc are all native defects in zinc oxide (ZnO). Substantial research over the past several decades have led to an improved understanding of defects in the “classic” semiconductors, silicon (Si), germanium (Ge), and gallium arsenide (GaAs). It is well-known how to dope Si *p*-type using boron (B) or *n*-type using phosphorous (P). The ability to create *p*-type and *n*-type conductivity in the same material is the first key step for creating transistors, which are the basis for most electronic devices.

1.2: Transparent Conducting Oxides: Motivation

Most materials that are highly conductive, such as metals or narrow band-gap semiconductors, are opaque to visible light. However, materials such as SiO_2 are transparent to visible light but are electrical insulators. Many applications, such as in photovoltaics and solid-state lighting, require a material that possesses both a strong electrical conductivity and the optical transparency to visible light.

Transparent conducting oxides (TCOs) form a class of wide-bandgap, metal-oxide semiconductors that successfully combine these two properties in a single material and, as a result, have found a wealth of applications as transparent contacts for photovoltaic cells and in flat-panel displays, and electrochromatic (smart) windows, to name a few.[2] Tin-doped indium oxide (ITO) has dominated the TCO market for years, but the scarcity of indium has significantly increased the price of this material.[3] Consequently, there has been extensive research to identify alternative materials that are both comparable in performance to ITO and economically viable. Thin films of cadmium oxide (CdO) outperform commercial ITO thin films in all aspects: the electrical conductivity and the carrier mobility are significantly higher and its transparency in the visible range is wider.[4] However, the toxicity of Cd has prevented its use in industrial-level production, which limits the studies of CdO to small-scale laboratory research.[5] Table 1.2.1 lists the TCOs that have been and continue to be studied extensively as alternatives to ITO. These materials are earth-abundant and therefore relatively cheap compared to ITO. None of these materials present major toxicity concerns, and high quality single crystals can be readily produced by various growth techniques.[6]

Table 1.2.1: Commonly studied TCO alternatives to ITO, their crystal structures, and their band gaps (at 293 K).

Material	**Formula**	**Crystal Structure**	**Band gap E_g,(eV)**
Zinc oxide	ZnO	wurtzite	3.4
Tin dioxide	SnO_2	rutile	3.6
Titanium dioxide	TiO_2	rutile	3.0
Strontium titanate	SrTiO3	cubic	3.25
Gallium oxide	Ga_2O_3	monoclinic	4.9

Interestingly, all of the TCOs listed in Table 1.2.1 exhibit *n*-type conductivity even in their undoped, as-grown state. This *n*-type conductivity was typically attributed to native defects, such as oxygen vacancies and cation interstitials. This conclusion was based on experimental trends where a decrease in the oxygen partial pressure in the growth environment was accompanied by an increase in the electrical conductivity. For example, Tomlins and coworkers[7] observed this trend in undoped ZnO single crystals. This evidence, however, is circumstantial, as there are usually other impurities present during the growth of the crystals. Advances in first principles calculations for point defects in solids[8] have allowed theorists to explore the behavior of oxygen vacancies in TCOs. These calculations show that oxygen vacancies are deep donors in many TCOs, including ZnO,[9] and therefore they cannot be responsible for the unintentional *n*-type conductivity observed in the as-grown materials.

Hydrogen has emerged as a key candidate to explain the unintentional *n*-type conductivity in undoped TCOs. Hydrogen is a common and often unintentional contaminant present in as-grown crystals because it is difficult to remove from the growth environment.[2] First-principles calculations performed by Van de Walle[10] for ZnO found that hydrogen acts exclusively as a donor in these materials. That is, the incorporation of hydrogen into an *n*-type material results in even stronger *n*-type conductivity. This result is in direct contrast to the behavior in traditional semiconductors, where hydrogen exhibits an amphoteric behavior and acts as an acceptor (donor) in *n*-type (*p*-type) semiconductors.

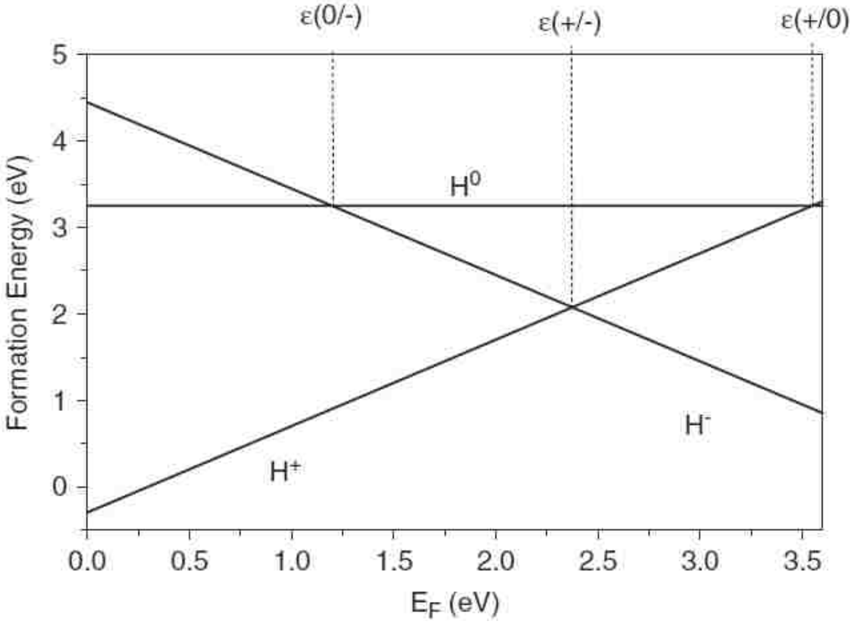

[redacted]

Theoretical calculations can help explain the amphoteric behavior of hydrogen in classic semiconductors vs. the donor behavior observed in most TCOs. (These explanations follow those found in Van de Walle, *Physica B*, 2006.)[11] Figure 1.2.1 shows the calculated formation energies for hydrogen in its different charge states in GaN (3.4 eV band gap) as a function of the Fermi level (E_F). The valence-band maximum (VBM) is set at $E_F = 0$ eV. The intersection of the formation energies of two different charge states, which are indicated by the $\varepsilon(a/b)$ terms at the top of the figure, show the Fermi level for which two different charge states, H^a and H^b, have equal formation energies. Under thermodynamic conditions, the defect with the lowest formation energy will be predominantly formed for a particular value of E_F. In *p*-type GaN, for example, E_F is close to the VBM and therefore hydrogen will enter as a donor (H^+), whereas in *n*-type GaN, E_F is close to the conduction band maximum (CBM) and will enter as an acceptor (H^-). Since hydrogen will only exist in GaN as H^+ or H^- (the formation energy of the neutral charge state H^0 is higher than the formation energies of H^+ or H^- for all E_F), the only relevant transition level is $\varepsilon(+/-)$. Therefore, in *n*-type GaN, $E_F > \varepsilon(+/-)$ and hydrogen will enter the crystal as an H^- acceptor, whereas in *p*-type GaN, $E_F < \varepsilon(+/-)$ and hydrogen will enter the crystal as an H^+ donor. This result effectively "pins" E_F at $\varepsilon(+/-)$ and prevents H from acting as only an acceptor or only a donor in this material.

Conversely, the position of $\varepsilon(+/-)$ relative to CBM gives a different behavior for hydrogen in TCOs. Figure 1.2.2 shows the location of the hydrogen energy level relative to the VBM and CBM for different semiconductors.[11] (The valence and conduction bands of each material have been offset from one another on an absolute energy scale). The thick lines indicate the position of the hydrogen energy level, $\varepsilon(+/-)$, predicted by first-principles calculations in each material, and the dashed line at -4.5 eV shows the universal alignment level for hydrogen in these materials. For materials where $\varepsilon(+/-)$ lies within the band gap, hydrogen is predicted to exhibit an amphoteric behavior. However, for materials such as ZnO, In_2O_3, and SnO_2, $\varepsilon(+/-)$ lies just below or near the CBM.

Thus, even in *n*-type TCOs, hydrogen will act exclusively as a donor and will contribute to the *n*-type conductivity. Both theory and experiment have shown that hydrogen acts as a shallow donor in ZnO,[12,13] SnO_2,[14,15] and In_2O_3.[16]

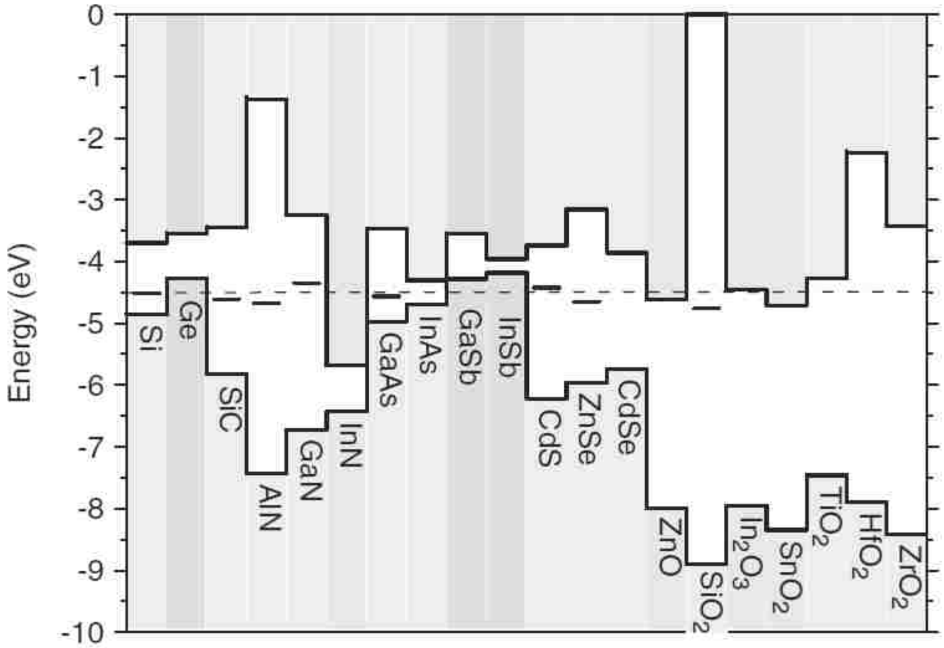

[redacted]

1.3: Studying Hydrogen Defects in TCOs

The overarching goal of the scientific community that studies defects is to understand the effect of different defects on the chemical and physical properties of a material. Success in understanding defect structures and properties, particularly for hydrogen defects in TCOs, requires the ability to directly compare theoretical calculations and experimental measurements. Examples for which theory and experiment have provided unambiguous results, including the inability to dope ZnO *p*-type using nitrogen, the Si *DX* center in $Al_xGa_{1-x}As$, and the effect of substitutional carbon impurities on the photoluminescence (PL) in GaN, are summarized by Alkauskas, McCluskey, and Van de Walle.[17] This paper and the references therein provide an overview of the first principles calculations and the most common experimental techniques used to study defects.

The focus of the Stavola group's research is to understand the structures and properties of hydrogen-related defects in semiconductors. Infrared (IR) spectroscopy is a powerful tool for studying the vibrational properties of light-element impurities. Since the vibrational frequency of a defect is sensitive to small changes in the masses of the constituent atoms, isotopic substitution experiments, in which hydrogen is exchanged with deuterium, can provide an unambiguous confirmation of the presence of H in a defect. The absorption arising from free charge carriers also occurs in the IR spectral region, which provides a contact-free method for probing the electrical conductivity of a sample. These experimental efforts are assisted by the theoretical calculations performed by Professor W. Beall Fowler using CRYSTAL06.[18] These first-principles calculations are used to determine the most energetically favorable hydrogen-related defects in a material, their approximate vibrational frequencies, and their thermal stabilities.

The content of this dissertation is as follows: Chapter 2 provides a survey of the vibrational properties of impurities in solids, their effect on the electrical and optical properties of the crystal, and the basics of Fourier Transform Infrared (FTIR) spectroscopy. Chapter 3 presents the development of a quantitative technique for studying the temperature-dependent, free-carrier absorption in TCOs using an FTIR spectrometer. Chapter 4 reports experiments where FTIR spectroscopy performed in conjunction with uniaxial stress has been used to study the microscopic structure and diffusion properties of the shallow hydrogen donor in In_2O_3. Chapter 5 discusses the properties of hydrogen centers and the free carrier absorption in $\beta-Ga_2O_3$.

1.4 References

1. J. Singh. Electronic and Optoelectronic Properties of Semiconductor Structures. (Cambridge University Press, 2003).

2. P. D. C. King & T. D. Veal. Conductivity in transparent oxide semiconductors. *J. Phys. Condens. Matter* **23,** 334214 (2011).

3. T. Minami. Transparent conducting oxide semiconductors for transparent electrodes. *Semicond. Sci. Technol.* **20,** S35 (2005).

4. A. Wang, *et al.* Indium-cadmium-oxide films having exceptional electrical conductivity and optical transparency: clues for optimizing transparent conductors. *P.N.A.S. U.S.A.* **98,** 7113 (2001).

5. S. C. Dixon, *et al.* *n*-type doped transparent conducting binary oxides: an overview. *J. Mater. Chem. C* **419,** 462 (2016).

6. Z. Galazka, "Growth Measures to Achieve Bulk Single Crystals of Transparent Semiconducting and Conducting Oxides.", Chapter 6 in *Handbook of Crystal Growth: Bulk Crystal Growth* (eds. T. Nishinga & P. Rudolph) (Elsevier, 2015).

7. G. W. Tomlins, *et al.* Zinc self-diffusion, electrical properties, and defect structure of undoped, single crystal zinc oxide. *J. Appl. Phys.* **87,** 117 (2000).

8. C. Freysoldt. *et al.* First-principles calculations for point defects in solids. *Rev. Mod. Phys.* **86,** 253 (2014).

9. A. Janotti & C. G. Van de Walle. Native point defects in ZnO. *Phys. Rev. B* **76,** 165202 (2007).

10. C. G. Van de Walle. Hydrogen as a cause of doping in zinc oxide. *Phys. Rev. Lett.* **85,** 1012–1015 (2000).

11. C. G. Van De Walle. Universal alignment of hydrogen levels in semiconductors and insulators. *Physica B Condens. Matter* **376–377,** 1–6 (2006).

12. M. D. McCluskey, *et al*. Infrared spectroscopy of hydrogen in ZnO. *Appl. Phys. Lett.* **81,** 3807 (2002).

13. E. V. Lavrov, *et al.* Hydrogen-related defects in ZnO studied by infrared absorption spectroscopy. *Phys. Rev. B* **66,** 165205 (2002).

14. W. M. Hlaing Oo, *et al.* Hydrogen donors in SnO_2 studied by infrared spectroscopy and first-principles calculations. *Phys. Rev. B* **82,** 193201 (2010).

15. F. Bekisli, *et al.* Hydrogen impurities and shallow donors in SnO_2 studied by infrared spectroscopy. *Phys. Rev. B* **84,** 035213 (2011).

16. W. Yin, *et al.* Hydrogen centers and the conductivity of In_2O_3 single crystals. *Phys. Rev. B* **91,** 075208 (2015).

17. A. Alkauskas, *et al*. Tutorial: Defects in semiconductors - Combining experiment and theory. *J. Appl. Phys.* **119,** 181101 (2016).

18. R. Dovesi, *et al. Crystal06 User's Manual*. (University of Torino, Torino, 2006.)

Chapter 2

Experimental Method: Infrared Spectroscopy of O-H Defects

2.1: Effects of Point Defects on Vibrational and Optical Properties of a Host Crystal

2.1.1: Local Vibrational Modes (LVMs)

In order to understand the behavior of point defects and impurities in a crystal, the vibrational properties of the host lattice must first be understood. A simple classical model,[1] shown at the top of Fig. 2.1.1(a), treats the atoms as point masses and the chemical bonds as harmonic springs with spring constant k. The equation of motion for a one-dimensional periodic, binary chain, with masses M and m, composed of N atoms and with unit cell length a, is given by,

$$\begin{aligned} M\ddot{u}_s &= k(u_s - v_s) - k(u_s - v_{s-1}) \\ m\ddot{v}_s &= k(v_s - u_s) - k(v_s - u_{s+1}) \end{aligned} \qquad \textbf{Eq. (2.1.1)}$$

This eigenvector-eigenvalue problem can be solved by writing Eq. (2.1.1) in matrix form and then diagonalizing the matrix. The standard solutions for the sth atoms (of type u or v) in the chain are given by,

$$u_s(t) = u \exp[i(qsa - \omega t)];\ v_s(t) = v \exp[i(qsa - \omega t)]$$

$$\omega_{\pm}(q) = k\left\{\left(\frac{1}{m} + \frac{1}{M}\right) \pm \sqrt{\left(\frac{1}{m} + \frac{1}{M}\right)^2 - \frac{4\sin^2(qsa/2)}{mM}}\right\}. \qquad \textbf{Eq. (2.1.2)}$$

The function $\omega_{\pm}(q)$ is the dispersion curve because it relates the speed of propagation of the waves as they travel through the crystal to the wave vector q. Barker and Sievers[1] have calculated the dispersion curves for a 48 atom chain of GaP (24 atoms each of Ga and P), which are shown at the bottom of Fig. 2.1.1(a). There are 48 allowed modes: 24 low-frequency (acoustic) modes and 24 high-frequency (optic) modes.

[redacted]

[redacted]

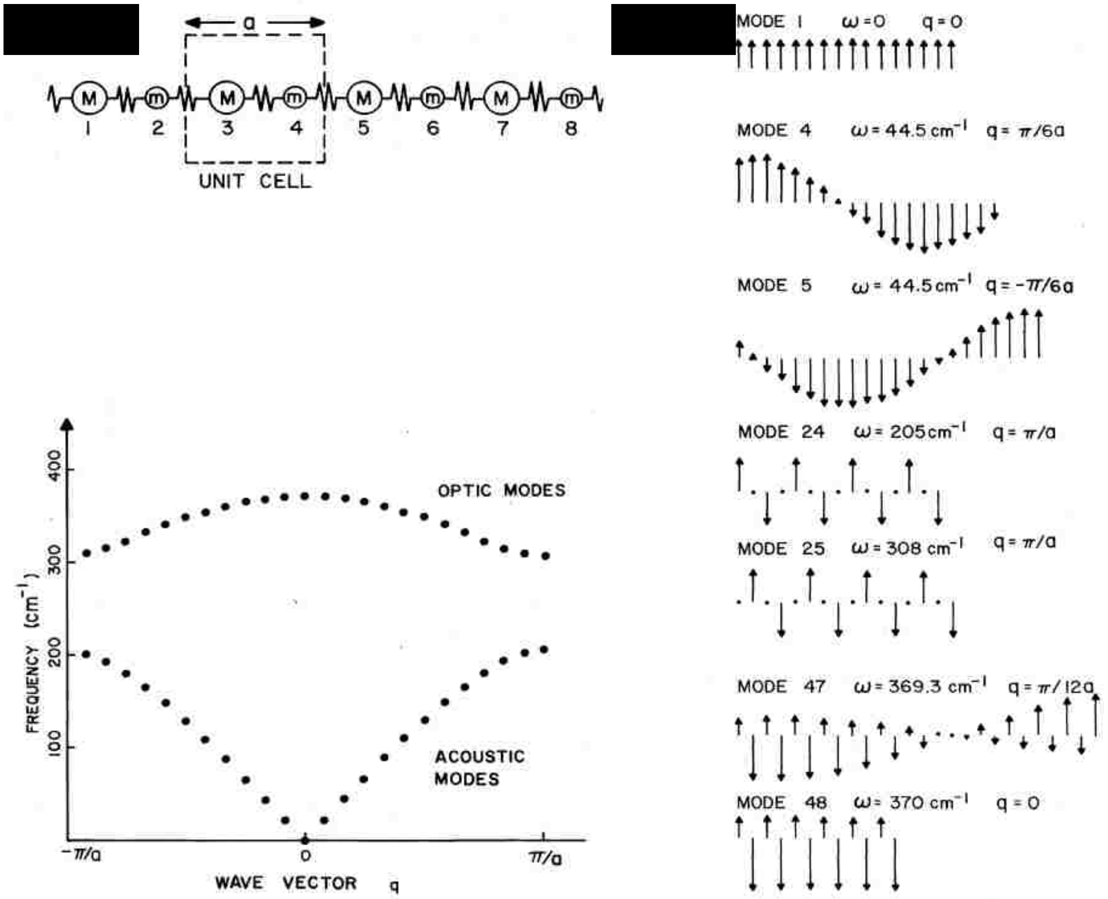

[redacted]

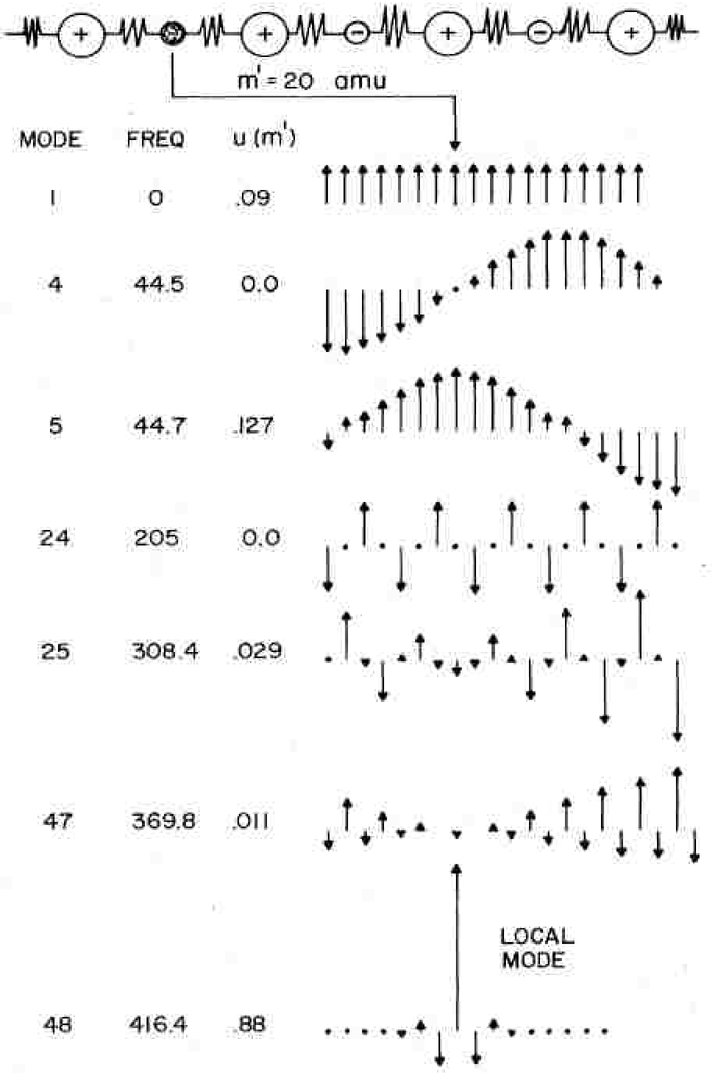
m' = 20 amu
MODE
FREQ
u (m')
1
0
.09
4
44.5
0.0
5
44.7
.127
24
205
0.0
25
308.4
.029
47
369.8
.011
LOCAL MODE
48
416.4
.88

[redacted]

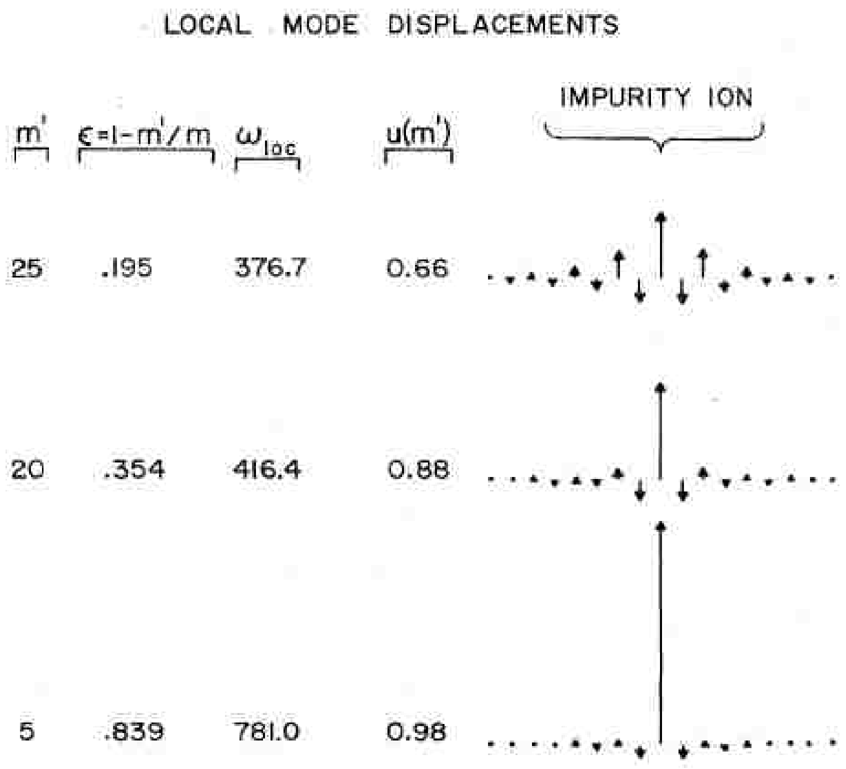

[redacted]

Figure 2.1.1(b) shows how the difference between the two types of modes stems from the motion of the neighboring atoms. Acoustic modes have the neighboring atoms moving in phase with each other. Optic modes have the neighboring atoms moving out of phase with each other.

To consider the effect of defects in this chain model, one of the atoms of mass m is replaced with an impurity atom with mass m' $(m' < m)$. For simplicity, the spring constant k between M and m' is assumed to have the same value as that between M and m. The effect of the new atom on the vibrational modes of the host crystal is shown in Fig. 2.1.2. Most of the acoustic and optic modes show little or no perturbation except for the highest frequency optic mode (mode 48). This mode has a higher frequency than the modes of the pure binary crystal; in the GaP model, an m' of 20 amu results in a frequency shift from 370 cm^{-1} to 416.4 cm^{-1}. This modified vibrational mode is not sinusoidal and is confined to the impurity atom and its first and second neighbors. As the mode is unable to propagate through the crystal, it is called a localized vibrational mode (LVM). Figure 2.1.3 shows how m' controls both the frequency and the degree of localization of the LVM. Leigh and Newman[2] found that the frequency of the LVM due to this light atom impurity with nearest neighbors of mass M and unchanged force constant k is approximately given by,

$$\omega^2 \sim k\left(\frac{1}{m'} + \frac{1}{\chi M}\right) = \frac{k}{\mu}. \qquad \textbf{Eq. (2.1.3)}$$

The parameter χ is usually approximately 2 and accounts for the coupling of the local vibrational mode with the host crystal.[3] Although Eq. (2.1.3) was derived assuming a substitutional impurity, the general idea that an impurity atom modifies the optical properties of crystal by creating a LVM with a frequency higher than any of the host modes is applicable to all point defects, including interstitial configurations.

2.1.2: Free Carrier Absorption

Metals and doped semiconductors can contain large densities of “free” electrons (or holes) that are not bound to any particular atoms. As a result, they do not feel a restoring force when interacting with an external electric field. The classical Drude-Lorentz model predicts the effect of these free-charge carriers on the optical properties of a material. The material is modeled as a plasma composed of an equal number of fixed positive ions and free electrons. Under the influence of an external electric field, the electrons will accelerate for some average time τ until they scatter back to a state with zero velocity and are again accelerated by the field. The scattering time τ is assumed to be independent of the frequency of the incident light. The one-dimensional differential equation of motion for the oscillations of the free electrons induced by the incident AC electric field $E(t)$ is given by,

$$m_0\ddot{x} + m_0\gamma\dot{x} = -eE(t), \qquad \textbf{Eq. (2.1.4)}$$

with m_0 and ω_0 as the mass and natural resonant frequency of the free electrons, respectively, and γ is the frictional damping rate in the medium. Assuming a solution in the form of a traveling wave, the relative permittivity ϵ_r of the material is,

$$\epsilon_r(\omega) = 1 - \frac{Ne^2}{\epsilon_0 m_0}\frac{1}{(\omega^2 + i\gamma\omega)} = 1 - \frac{{\omega_p}^2}{(\omega^2 + i\gamma\omega)}. \qquad \textbf{Eq. (2.1.5)}$$

The plasma frequency ω_p corresponds to the collective oscillation of the entire free-carrier "gas", and N is the carrier concentration (in cm^{-3}). For $\omega \leq \omega_p$, the material is completely reflective, and no light is transmitted. The reflectivity decreases and asymptotically approaches zero for$\omega > \omega_p$. Equation (2.1.4) can be solved in terms of the velocity instead of the position, in which case the damping rate γ is replaced with the reciprocal scattering time $1/\tau$. Substitution of the expression for the velocity is into Ohm's law gives,

$$\boldsymbol{j}(t) = -Ne\boldsymbol{v}(t) = \frac{-Ne^2\tau}{m_0}\frac{1}{1 - i\omega\tau}\boldsymbol{E}(t) = \sigma\boldsymbol{E}(t),$$

and obtain the AC electrical conductivity,

$$\sigma(\omega) = \frac{Ne^2\tau}{m_o}\frac{1}{1 - i\omega\tau} = \frac{\sigma_0}{1 - i\omega\tau}. \qquad \textbf{Eq. (2.1.6)}$$

A comparison of Eqs. (2.1.5) and (2.1.6) reveals that the AC conductivity and the dielectric constant are related to each other by,

$$\epsilon_r(\omega) = 1 + \frac{i\sigma(\omega)}{\epsilon_0 \omega}.$$

Thus, optical measurements of $\epsilon_r(\omega)$ for a metal or doped semiconductor in the free-carrier spectral region (typically 5 – 30 μm) are equivalent to electrical measurements of $\sigma(\omega)$. For a doped semiconductor, there are two modifications that need to be made to the above derivation. First, the mass of the free electron (hole) m_o is replaced by the effective mass m^* since the carrier is moving in the conduction (valence) band of the material. Second, the dielectric constant ϵ_0 must be multiplied by $\epsilon_{\text{optical}}$ to account for the background polarizability of the undoped semiconductor. Here, $\epsilon_{\text{optical}} = n^2$ where n is the index of refraction of the undoped semiconductor in the spectral region where it is transparent. With these modifications, Eq. (2.1.5) becomes,

$$\epsilon_r(\omega) = \epsilon_{\text{optical}} \left[1 - \frac{{\omega_p}^2}{(\omega^2 + i\gamma\omega)}\right], \text{and}$$

$${\omega_p}^2 = \frac{Ne^2}{\epsilon_{\text{optical}} \epsilon_0 m^*}.$$

Eq. (2.1.7)

The term “free carrier absorption” refers to the absorption of light with frequencies above ω_p. The absorption coefficient for the free carriers, α_{FC}, can be shown to have a frequency dependence given by,

$$\alpha_{\text{FC}}(\omega) = \frac{Ne^2}{n\epsilon_0 m^* c\tau} \frac{1}{\omega^2}.$$

Eq. (2.1.8)

Equation (2.1.8) shows that α_{FC} should depend on the carrier density and have an ω^{-2} dependence. However, this relation was derived under the assumption that the relaxation time τ is independent of ω. As will be discussed in Chapter 3, α_{FC} for many *n*-type doped semiconductors shows an $\omega^{-\beta}$ dependence where β is approximately 2 to 3, which arises from the fact that different scattering processes have different characteristic scattering times. Figure 2.1.4 shows the conduction band of a heavily doped *n*-type semiconductor and the free carrier absorption process that takes place within the conduction band.[4] Free electrons occupy energy levels up to the Fermi level, E_F, which is set by the doping concentration N. These electrons undergo phonon-assisted intraband transitions to a higher energy state, and then relax back down to a state below E_F.

[redacted]

[redacted]

The most important point of the derivations of Eqs. (2.1.7) and (2.1.8) is to show the crucial role the carrier concentration plays in TCOs. As α_{FC} and ω_p show a N and $N^{1/2}$ dependence, respectively, increasing the carrier concentration reduces the overall transmission in the transparent spectral region and also decreases the window of transparency of the semiconductor. These effects can be detrimental in TCOs because a carrier concentration that is too large eliminates the visible transparency that is required for a TCO's successful application.

2.2 Identifying Defect Structures Using IR Spectroscopy

2.2.1: Elementary Spectroscopy

Infrared (IR) radiation has wavelengths between 0.7 and 1000 μm and can be used to probe vibrational transitions in a material. Spectroscopists prefer to discuss the energy of transitions using the reciprocal wavelength, called the wavenumber and designated $\bar{\nu}$, since it is directly proportional to energy as shown in Eq. (2.2.1),

$$E = \frac{hc}{\lambda} = hc\bar{\nu} \qquad \textbf{Eq. (2.2.1)}$$

In terms of wavenumbers, IR radiation falls roughly between 10 and 10,000 cm^{-1}, and the frequencies of O-H and O-D stretching modes appear in the range fall between 2900-3500 cm^{-1} and 2000-2600 cm^{-1}, respectively.

The Beer-Lambert law expresses the strength of the interaction of light with matter and is given in Eq. (2.2.2),

$$dI = -I \cdot \alpha \cdot dx. \qquad \textbf{Eq. (2.2.2)}$$

A simple expression can be obtained for a uniform sample of thickness d with an absorption coefficient α, which includes the intrinsic absorption of the sample and the absorption arising from impurities. The absorption coefficient α is the intrinsic quantity that is measured because it is independent of the sample length. The light beam is also assumed to be normally incident upon the front surface of the sample. Finally, reflections at the front and back surfaces and scattering from rough surfaces are ignored. Integrating Eq. (2.2.2) over the thickness of the sample then yields,

$$\ln(I_d/I_0) = -\alpha d.$$

In IR spectroscopy, I_d is a raw sample spectrum and I_0 is a reference spectrum, typically of the empty sample holder or of an identical sample, which does not contain the signal of interest. The transmission, *T*, is defined by,

$$T = \frac{I(d)}{I_0} = \exp(-\alpha d). \qquad \textbf{Eq. (2.2.3)}$$

It is often more convenient to analyze spectral results in terms of the absorption of light by the sample rather than by the light that is transmitted. For a uniformly absorbing sample which neglects surface reflections (as shown in Fig. 2.2.1(a)), the absorbance *A*, is defined as,

$$A = -\log_{10}(T) = -\log_{10}\big(\exp(-\alpha d)\big) = \alpha d \log_{10} e. \qquad \textbf{Eq. (2.2.4)}$$

Figure 2.2.1(b) considers reflections at the front and back surfaces of the sample but neglects interference effects of the multiply reflected beams. The transmission for this sample becomes,

$$T = \frac{(1-R_1)(1-R_2)\exp(-\alpha d)}{1-R_1R_2\exp(-2\alpha d)}, \qquad \textbf{Eq. (2.2.5)}$$

in which R_1 and R_2 are the reflection coefficients at the front and back surfaces, respectively. Since most IR measurements are made on a uniform single crystal, $R_1 = R_2 = R$. In the limit of a strongly absorbing medium $(\alpha d \gg 1)$, the transmission reduces to,

$$\lim_{\alpha d \gg 1} T = (1-R)^2 \exp(-\alpha d), \qquad \textbf{Eq. (2.2.6)}$$

and for a transparent medium ($\alpha = 0$),

$$\lim_{\alpha \to 0} T = \frac{1 - R}{1 + R}.$$ **Eq. (2.2.7)**

[redacted]

[redacted]

[redacted]

The reflection coefficient R is determined by the real and imaginary parts of the complex index of refraction of the material. The real part of the index, n, determines the refraction and reflection of light at a discontinuity between two mediums, while the imaginary part, κ, accounts for the absorption of light as it passes through the material. Equation (2.2.8) shows the reflection coefficient when written in terms of n and κ,

$$R = \frac{|\tilde{n} - 1|^2}{|\tilde{n} + 1|^2} = \frac{(n - 1)^2 + \kappa^2}{(n + 1)^2 + \kappa^2}.$$ **Eq. (2.2.8)**

The calculation of the absorption coefficient from the transmission using Eq. (2.2.3) introduces an error of approximately 10%. Using Eq. (2.2.8) to correct for surface reflections reduces this error to 1-2%. The calculation of absorption coefficients will be discussed in more detail in Chapter 3.

2.2.2: Selection Rules in IR Spectroscopy

Light impurities, such as hydrogen, give a vibrational mode that is localized near the impurity atom and its nearest neighbors. For an interstitial hydrogen defect, the motion approximately involves only the hydrogen atom and its nearest neighbor, which can be treated as an anharmonic oscillator. In the harmonic approximation, there are two selection rules for a vibrational mode to be IR active. First, the motion of the oscillator must give rise to a non-zero change in the electric-dipole moment so that it can interact with the oscillating electric field of the incident light. In quantum mechanics, this statement is equivalent to there being a non-zero transition probability W between the initial (i) and final (f) vibrational states,

$$W \propto \left|\hat{e} \cdot \mu_{if}\right|^2. \qquad \textbf{Eq. (2.2.9)}$$

for which $\hat{e}$ is the unit vector in the direction of polarization of the incident light, and μ_{if} is the electric-dipole moment matrix element of the defect center. The second selection rule states that allowed transitions give rise to a change in the vibrational quantum number between the initial and final states of $\Delta n = n_f - n_i = 1$. At room temperature, most materials are in the vibrational ground state, so IR spectroscopy observes fundamental transitions (0 → 1) of these defects.

2.2.3: Atomic Composition: Isotope Effect

Equation (2.1.3) shows that a change to the mass of the host or impurity atom results in corresponding shift in the vibrational frequency. IR measurements taken with high spectral resolution can detect the spectral features associated with different atomic isotopes, which reveal important information about the composition of the defect and its neighboring atoms. An excellent example of the effect of isotopic substitution is the Li-OH complex in ZnO, which was studied by Shi *et al.*[5] Figures 2.2.2(a) and (b) show the IR absorbance spectra of Li-containing ZnO single crystals that were annealed in H_2 and D_2 ambients, respectively. The ratio of the H-to-D frequencies of the strong lines at 3577.3 and 2644.5 cm^{-1} is 1.35. Using Eq. (2.1.3), the ratio of the vibrational frequencies for H and D is predicted to be approximately $\sqrt{2}$,

$$r = \frac{\omega_{\mathrm{H}}}{\omega_{\mathrm{D}}} \sim \sqrt{\frac{\left(\frac{1}{m_H} + \frac{1}{\chi M}\right)}{\left(\frac{1}{m_D} + \frac{1}{\chi M}\right)}} \approx \sqrt{\frac{m_{\mathrm{D}}}{m_{\mathrm{H}}}}\left[1 + \frac{m_H}{2\chi M} - \frac{m_D}{2\chi M} + \cdots\right] \qquad \textbf{Eq. (2.2.10)}$$

$$\approx \sqrt{2}\left[1 - \frac{m_H}{2\chi M}\right],$$

which confirms that the defect includes a hydrogen atom. The weaker pairs of H and D lines at 3566.6(2629.2) cm^{-1} and 3571.7(2636.4) cm^{-1} show similar H-to-D frequency ratios. The relative intensities of these lines are consistent with the natural abundances of the three stable O isotopes (^{16}O:^{17}O:^{18}O = 99.757:0.038:0.205). In the O-D spectrum, the strong 2644.5 cm^{-1} line shows a weak shoulder at 2644.7 cm^{-1} (The isotopic partner of this shoulder in the O-H spectrum is unresolved from the 3577.3-cm^{-1} line.) The relative intensity of these two O-D lines matches the ratio of the natural abundances of the two stable isotopes of Li, (^{7}Li:^{6}Li = 92.41:7.59). Thus, the seven vibrational lines correspond to the different isotopic configurations of the same defect.

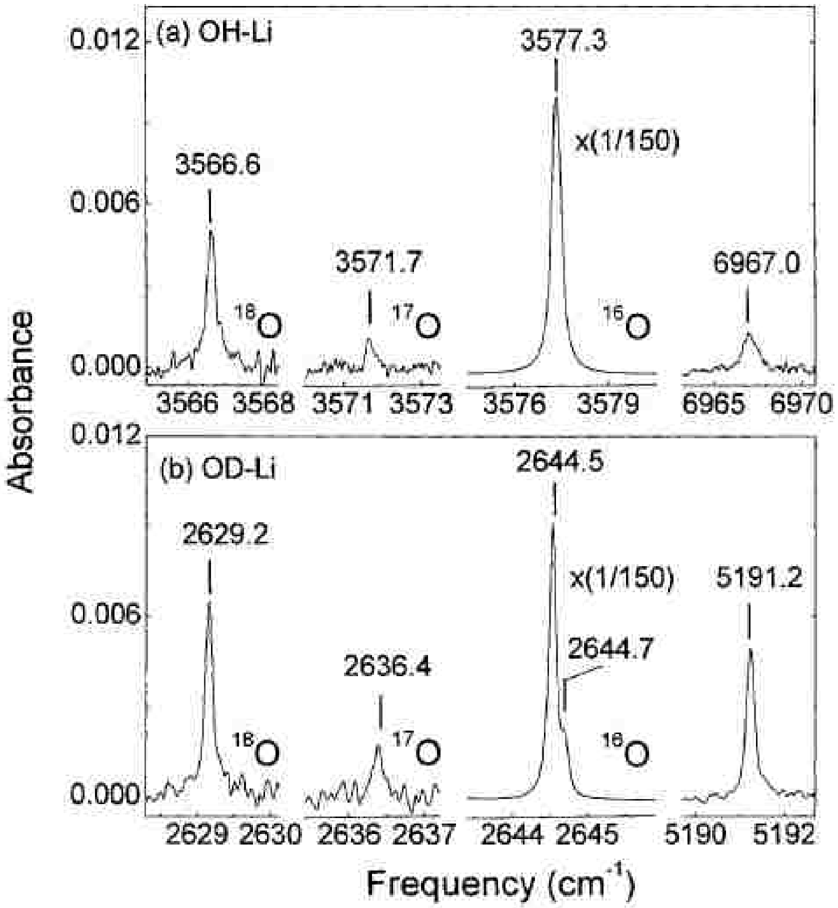

[redacted]

2.2.3: Absorption Line Strength: Concentration and Thermal Stability

Dawber and Elliott[6] have shown that the integrated absorption coefficient of a defect LVM is proportional to the concentration of the defect in the sample, as shown by Eq. (2.2.11),

$$\int \alpha(\bar{\nu})d\bar{\nu} = \frac{\pi q^2 N}{mnc^2}, \qquad \textbf{Eq. (2.2.11)}$$

in which N is the defect concentration (in cm^{-3}), q is the effective charge of the defect mode (in esu), m is the mass of the defect, n is the refractive index of the host crystal, and c is the speed of light (in cm/s). Solving Eq. (2.2.11) for N leads to an equation which determines the defect concentration from the integrated absorption coefficient,

$$N = \frac{mnc^2}{\pi q^2}\int \alpha(\bar{\nu})d\bar{\nu} = A\int \alpha(\bar{\nu})d\bar{\nu} \qquad \textbf{Eq. (2.2.12)}$$

The calibration factor A is typically determined from other experimental techniques, such as secondary ion mass spectrometry (SIMS) or the Hall effect.[7] However, a technique like SIMS measures the total impurity concentration in a material, even though the impurity may be involved in several defect structures besides the LVM of interest. Thus, A can vary by a factor of two or more depending on the method of determination. The lower limit for the defect concentration that can be detected with IR absorbance measurements is roughly 10^{18} cm^{-3} in a 1-μm-thick layer or 10^{14} cm^{-3} in a 1-cm-thick sample. Due to the availability of highly sensitive detectors at frequencies near 2,000 cm^{-1}, the detection limit for hydrogen-containing defects is closer to 10^{17} cm^{-3} in a 1-μm-thick layer.[7]

The relationship between the defect concentration and the integrated absorption coefficient offers a method to study both the reaction chemistry between different defects and the thermal stability of the individual centers. If the temperature is sufficiently high during a heat treatment, a defect or defect complex can migrate through the lattice. These anneals are terminated by rapidly cooling the sample to room temperature, typically by quenching in water, which “freezes” in the distribution of defects present at the end of the anneal. The changes in the integrated absorbances of the vibrational lines of the annealed sample reflect the changes in the defect populations. Anneals are typically performed in a tube furnace under the flow of inert gas (He or N_2) to ensure any changes in the integrated absorbance are from defect reactions within the sample and not from reactions with the annealing environment.

As stated in Chapter 1, theory predicts that hydrogen defects often act as shallow donors in TCOs. Infrared spectroscopy can be used to verify this hypothesis by checking if the changes in the free carrier absorption due to thermal annealing are correlated with corresponding changes to the integrated absorbance of a particular O-H LVM.

2.2.4: Anharmonicity: Overtones

Anharmonic contributions to the potential energy have several effects on vibrational spectra. First, the LVM frequency of a fundamental transition is modified compared to the frequency from the harmonic approximation. The Morse potential energy function[8] given in Eq. (2.2.13) is a common model used to understand this effect.

$$U(r-r_e) = D_e(\exp[-2\alpha(r-r_e)] - 2\exp[-\alpha(r-r_e)])^2. \qquad \textbf{Eq. (2.2.13)}$$

Here, D_e is the dissociation energy, r is the internuclear distance, r_e is the equilibrium nuclear distance (i.e., bond length), and α is a parameter given by,

$$\alpha = \sqrt{\frac{k}{2D_e}}.$$

The non-relativistic Schrödinger equation for a diatomic molecule can be solved analytically for the Morse potential. The energy difference between vibrational energy levels 0 and *n* is given by,

$$\Delta E_{n0} = E_n - E_0 = n\left[A\mu^{-1/2} - (n+1)B\mu^{-1}\right]$$

$$A = \alpha\sqrt{\frac{\hbar D_e}{\pi c}}; \quad B = \frac{\hbar\alpha^2}{4\pi c}. \qquad \textbf{Eq. (2.2.14)}$$

In terms of the fundamental frequency ω_e and the degree of anharmonicity χ_e, Eq. (2.2.14) becomes,

$$\Delta E_{n0} = n\omega_e[1 - (n+1)\chi_e], \qquad \textbf{Eq. (2.2.15)}$$

where $\omega_e\chi_e$ is known as the anharmonicity constant. The anharmonicity of a vibrational mode is important when an experimentally observed LVM frequency is compared with a predicted frequency based on first-principles calculations.

Anharmonicity also breaks the Δ*n* = 1 selection rule and permits transitions where Δ*n* > 1. In the harmonic approximation, overtones (if they were allowed) would occur at twice the frequency of the corresponding fundamental transition. As seen in Eq. (2.2.16), the anharmonicity will also affect the frequency of the overtone line,

$$\Delta E_{20} = 2\omega_e[1 - 3\chi_e]. \qquad \textbf{Eq. (2.2.16)}$$

Overtone transitions are usually two orders of magnitude weaker than their fundamental counterparts, which makes them difficult to detect. Shi *et al.*[9] observed the first overtones of the fundamental transitions of the ^{16}O-H and ^{16}O-D modes of the Li-OH and Li-OD complexes in ZnO, which are shown in Figs. 2.2.2(a) and (b). From the fundamental and first overtone lines for both the hydrogen- and deuterium-containing defects, they determined ω_e = 3770.0 cm^{-1} and χ_e = 0.0253, which allowed a complete characterization of the vibrational properties of this defect.

2.2.5: Local Symmetry: Polarization Properties and Uniaxial Stress

[redacted]

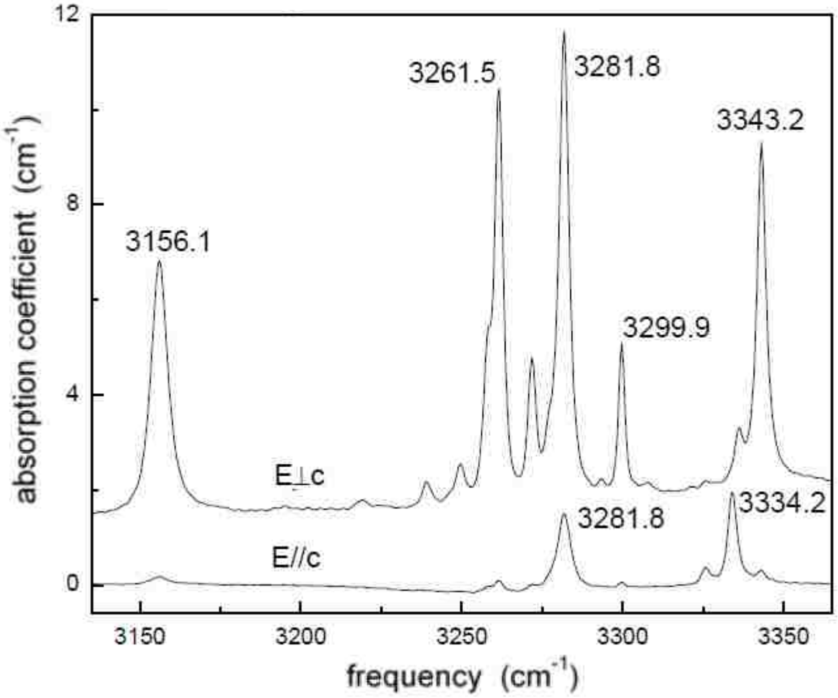

[redacted]

Equation (2.2.9) shows that the transition probability amplitude between vibrational states is proportional to the square of the projection of the polarization vector of the incident light on the electric dipole moment of the defect center. Thus, polarized light can be used to probe the orientation of a bond within the defect structure. Bekisli *et al.*[10] used the polarization properties of O-H LVMs observed in hydrogenated rutile SnO_2

single crystals to help assign possible microscopic structures predicted by theory to the vibrational lines. Figure 2.2.3 shows that the transition moments of the vibrational modes at 3156.1, 3261.5, 3299.9, and 3343.2 cm^{-1} are perpendicular to the c axis, within error.

For crystals with high symmetry, such as those with diamond or zinc blende lattices, defect centers can exist in several crystallographically-equivalent orientations, making it difficult to determine the bond orientation from polarized IR spectra alone. Although electric and magnetic perturbations are useful for studying electronic transitions arising from defects, uniaxial compression of a crystal is the preferred technique for lifting the orientational degeneracy in vibrational spectroscopy.[7] The energy levels of crystallographically inequivalent centers undergo different shifts depending on the axis of compression, P. Therefore, compression changes the transition frequencies of differently oriented defects and splits the vibrational lines. The stress-induced perturbation of the transition energy, Δ, of a specifically oriented defect can be written in terms of a symmetric piezospectroscopic tensor, A_{ij}, as,

$$\Delta = \sum_{ij} A_{ij}\sigma_{ij}, \qquad \textbf{Eq. (2.2.17)}$$

where $\sigma_{ij} = \sigma\cos(P,i)\cos(P,j)$ is the product of the magnitude of the stress and the direction cosines of the stress vector with respect to the coordinate axes i and j. These effects can lead to the reversible splittings of a vibrational line into several components, as compared to an unstressed center. Polarized light can be used to selectively excite transitions for defect centers with different orientations under uniaxial stress. The samples can be cooled to sufficiently low temperature (4.2 K) such that the defect is unable to reorient on the timescale of the IR measurement. In crystals with high symmetry, it is usually sufficient to compare the observed splitting patterns for stress applied along the [001], [110] and [111] directions with patterns tabulated in the literature[11–13] to determine the defect symmetry and the direction of its transition moment.

The orientation-dependent shifts of the ground-state energy levels create energy differences between the inequivalent defect sites. The relative occupations of defects at these different sites are determined from the Boltzmann factors associated with the different sites. Furthermore, in favorable cases, there will be a temperature range over which the defect can reorient among its stress-split configurations via thermally activated jumps, which manifests itself as an anisotropy of the polarized absorption, called a dichroism. A convenient way to express this anisotropy is through the dichroic ratio $\mathcal{D}$, as defined by Eq. (2.2.18),

$$\mathcal{D} = \frac{\alpha_{\perp} - \alpha_{||}}{\alpha_{\perp} + \alpha_{||}}. \qquad \textbf{Eq. (2.2.18)}$$

Here, $\alpha_{||}$ and $\alpha_{\perp}$ are the absorption coefficients for the parallel and perpendicular polarized light beams relative to the stress direction.

There are two approaches for using polarized IR spectroscopy combined with uniaxial stress to probe the kinetics of the reorientation of a defect among its stress-split configurations. In the first type of experiment, a net alignment of the defect is obtained by applying stress to the sample at a temperature that is sufficiently high for the defect to freely reorient among its different configurations. The sample is then cooled under stress to low temperature so that the alignment becomes “frozen in” and will persist even after stress is removed. Annealing the sample in the absence of stress will redistribute the defects randomly among their equivalent orientations, removing the stress-induced alignment. The kinetics of the disappearance of the stress-induced alignment can be related to the reorientation kinetics of the defect center. In the second type of experiment, stress is applied to the sample after it has been cooled to low temperature. Annealing the sample under stress at a temperature that is sufficiently high for the defect to reorient among its different configurations creates a stress-induced alignment due to the preferential occupation of the defect orientation with the lowest ground-state energy.

In both types of experiments, changes in $\mathcal{D}$ result from changes in the stress-induced alignment. If the reorientation is assumed to follow first order kinetics, the production (or decay) of the stress-induced alignment at temperature T is given by Eq. (2.2.19) [or (2.2.20)],

$$\mathcal{D} = \mathcal{D}_0 \, [1 - \exp(-k_d t)] \qquad \textbf{Eq. (2.2.19)}$$

$$\mathcal{D} = \mathcal{D}_0 \, \exp(-k_d t). \qquad \textbf{Eq. (2.2.20)}$$

In both cases, the rate of change of the dichroism, k_d is given by,

$$k_d = \nu_0 \, \exp(-E_A/k_B T), \qquad \textbf{Eq. (2.2.21)}$$

in which E_A is the activation energy for the reorientation, ν_0 is an attempt frequency and k_B is the Boltzmann constant. The defect reorientation involves a jump from one specific site to another with a rate is proportional to k_d; the proportionality constant depends on the configuration of the defect in the lattice. The change in $\mathcal{D}$ can be measured either by annealing the sample for the same length of time at several different temperatures (isochronal annealing) or by annealing the sample at the same temperature for increasing lengths of time (isothermal annealing). In both cases, the activation energy and the attempt frequency can be extracted from fits to the data.

Polarized IR spectroscopy combined with uniaxial stress is a powerful tool for determining the microscopic properties of point defects. An excellent example is the study of the H-B acceptor complex in Si by Bergman *et al.*[14] and Cheng and Stavola.[15] This complex gives rise to a LVM at 1903 cm^{-1}.

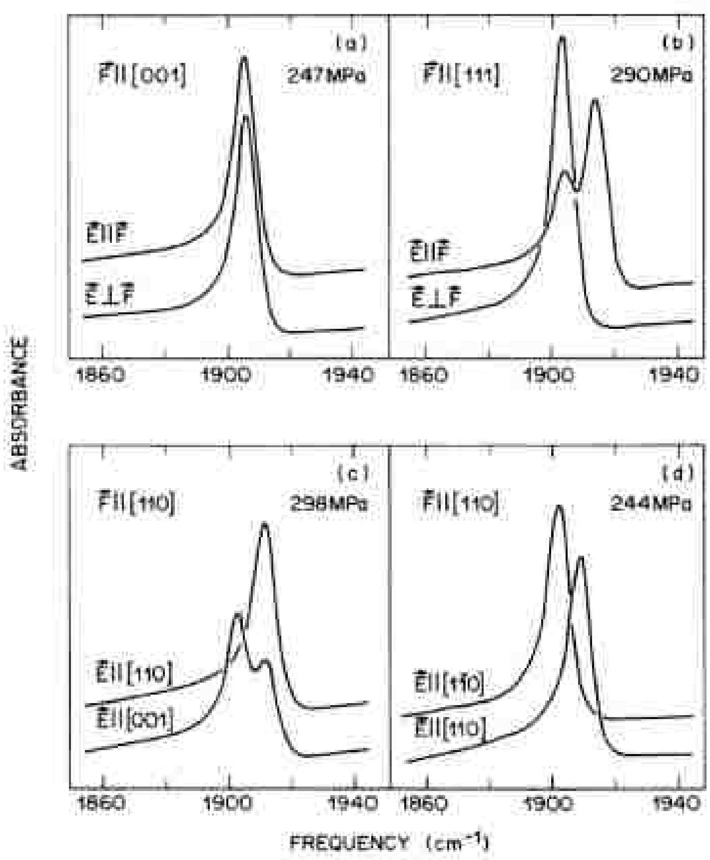

[redacted]

Figure 2.2.4 shows the polarized IR absorbance spectra of this vibrational line with stress applied along the [001], [111], and [110] directions. Under [001] stress, the spectrum shows a single component present in both polarizations. The spectra of the sample under

[111] stress show two components. One component is seen for $\mathbf{E} \parallel \boldsymbol{\sigma}$, and another component is seen in both polarizations. Under [110] stress and a viewing axis along the $[1\bar{1}0]$ direction, there are two components: one is seen in both polarizations and the other is only seen for $\mathbf{E} \perp \boldsymbol{\sigma}$. With a viewing axis along the [001] direction, one component is seen in each polarization. This splitting pattern is consistent with a defect that has trigonal symmetry, i.e., the transition moment of the defect is along a [111] direction of the crystal.

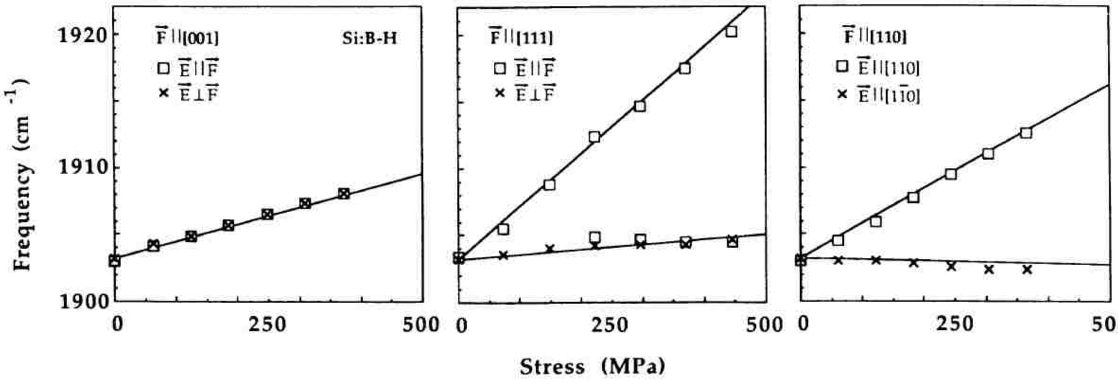

[redacted]

Figure 2.2.5 shows the LVM frequency of the stress-split components as a function of the applied stress. For a trigonal center with its primary axis along the [111] direction, the piezospectroscopic tensor has two independent components: A_1 and A_2. The fits to the shift rates are in excellent agreement with the data, which also supports the assignment of trigonal symmetry to the defect. Furthermore, a stress-induced dichroism was observed in H and D implanted samples subjected to [110] stress. For this defect, the jump rate k_j is related to k_d by,

$$k_j = 4k_d.$$

Figure 2.2.6 shows a semi-log plot of the jump rates vs. 100/T for both hydrogen and deuterium determined from the decay of the stress-induced alignment at several different temperatures. The slope of the best-fit line through the data is related to the activation energy of reorientation shown in the inset of the figure.

[redacted] [redacted]

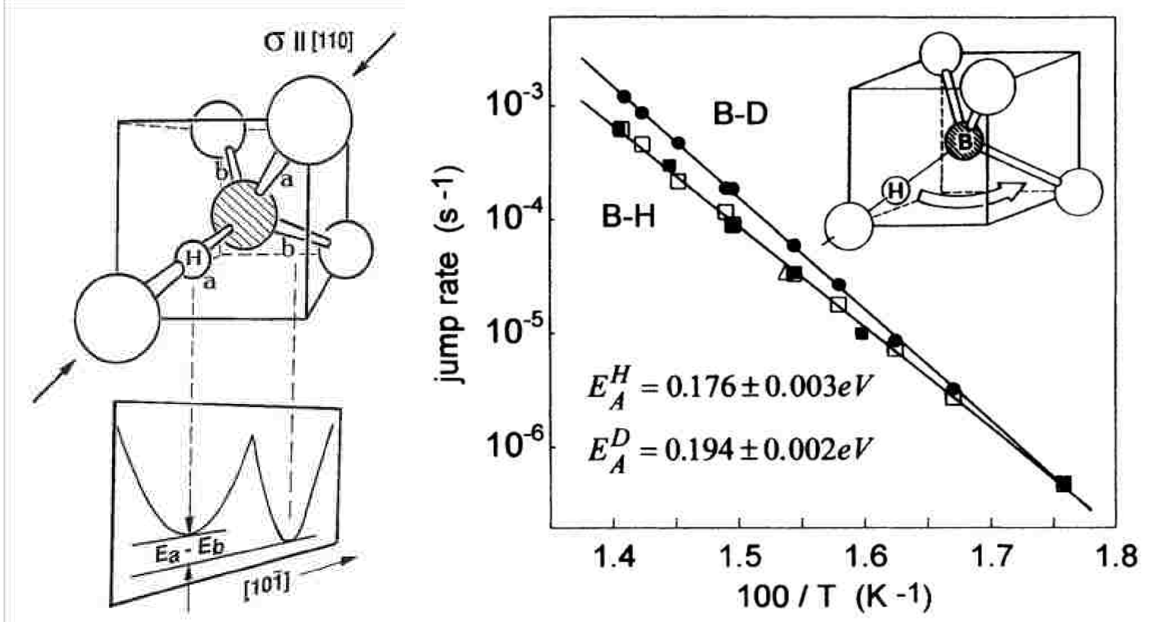

[redacted]

The Si:B-H complex is quite puzzling: the reorientation rate of the B-D complex is faster than that of the B-H complex, whereas one would have expected it to be slower because

D is heavier than H. In addition, the B-H defect does not obey a simple Arrhenius behavior with a single activation energy. Internal friction measurements (not shown) by Canneli *et al*.[16] find an activation energy of 0.223±0.006 eV compared to the value of 0.176±0.003 eV found in uniaxial stress experiments performed at lower T. The non-Arrhenius behavior indicates that the reorientation occurs a mechanism other than simple hopping over a barrier.[17]

In some cases, the process by which the defect reorients is also a diffusion jump. In this case, the rate of production (or decay) of the stress-induced alignment determines the diffusion constant D, which is related to the time constant for the diffusion jump from one specific site to another. The technique of using uniaxial stress to determine a defect's diffusion coefficient was pioneered by Corbett *et al*.[18] in their investigation of the diffusion of the interstitial oxygen defect in Si. Further discussion of the diffusion of point defects will be presented in Chapter 4.

2.3: Fourier Transform Infrared (FTIR) Spectroscopy

Ordinary spectrometers in which the exciting light is dispersed suffer from low signal-to-noise (S/N) ratios, long scan times, poor resolution, and a lack of an internal calibration standard. Fourier transform infrared (FTIR) spectroscopy overcomes many of these difficulties by indirectly measuring the frequency domain spectrum. Figure 2.3.1 shows the working principles of the core of an FTIR spectrometer, the Michelson interferometer.[19] Light from a source (here, monochromatic) is incident on a beam splitter, which, under ideal circumstances, reflects and transmits equal portions of light to the fixed mirror M1 and moving mirror M2. The beam splitters have a thin antireflective layer covering the surface to minimize power loss. The two beams travel path lengths of OM1 and OM2, respectively, to and from the highly reflective mirrors. The beams recombine at the beamsplitter and continue through the sample compartment and to the detector. The intensity of light measured by the detector is a function of optical path length difference between the two beams, $\delta = 2(\mathrm{OM1} - \mathrm{OM2})$. At $\delta = n\lambda; n = 0, 1, 2 \ldots \mathbb{Z}$, the path lengths are equivalent; the beams are completely in phase and interfere constructively to yield a maximum detector signal. When $n = (1 + m)/2\,; m = 1, 2, \ldots \mathbb{Z}$, the path lengths differ by a half wavelength; the beams are completely out-of-

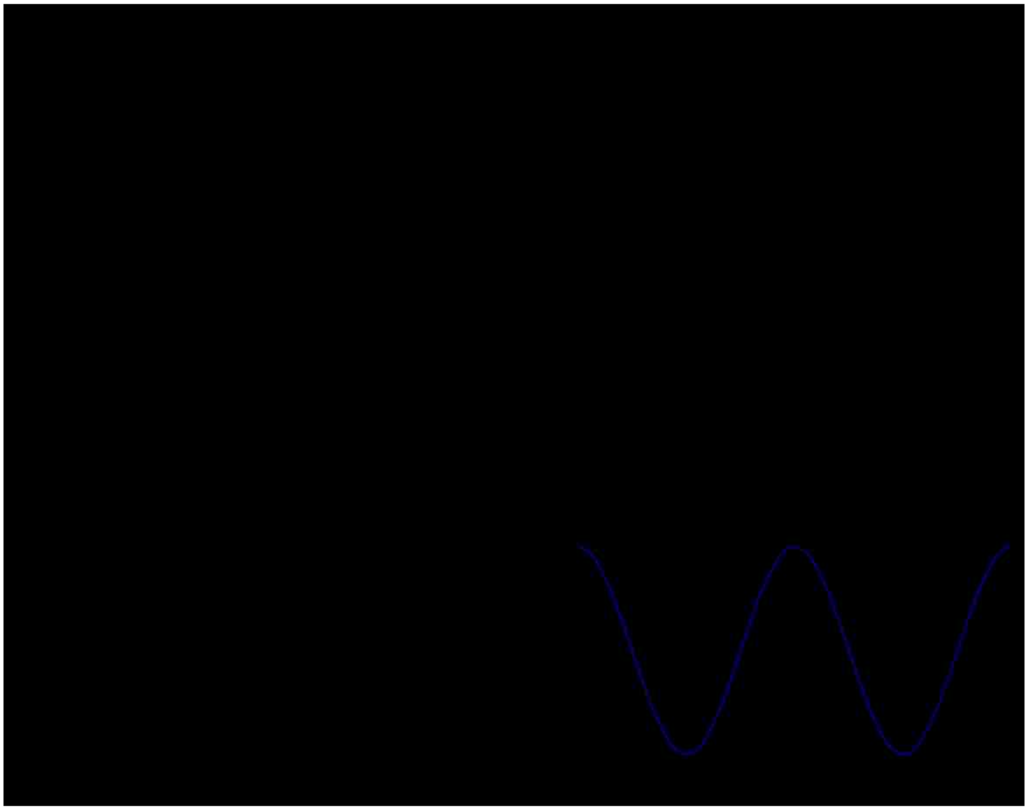

[redacted]

phase and interfere destructively to yield zero signal on the detector. This alternating pattern of constructive and destructive interference leads to a variation in the beam intensity, $I(\delta)$, which is given by Eq. (2.3.1),

$$I(\delta) = B(\bar{\nu}) \cos(2\pi\bar{\nu}\delta) \quad \text{monochromatic source,} \tag*{\textbf{Eq. (2.3.1)}}$$

in which $B(\bar{\upsilon})$ is the frequency-domain spectrum. Lord Rayleigh was the first to realize that $B(\bar{\nu})$ could be recovered by taking the Fourier transform of $I(\delta)$. Thus, $B(\bar{\nu})$ and $I(\delta)$ represent a complex Fourier transform pair. For a broadband (polychromatic) source, Eq. (2.3.1) is modified to,

$$\begin{gathered} I(\delta) = \int_{-\infty}^{\infty} B(\bar{\nu}) \exp(i2\pi\bar{\upsilon}\delta)\, d\bar{\nu} \\ B(\bar{\nu}) = \int_{-\infty}^{\infty} I(\delta) \exp(i2\pi\bar{\nu}\delta)\, d\delta. \end{gathered} \tag*{\textbf{Eq. (2.3.2)}}$$

The use of complex exponentials accounts for any asymmetry introduced into the interferogram, i.e., non-perfect compensation leads to sine components in the interferogram. Additional corrections to Eq. (2.3.2) result from the finite scan length, the apodization of the interferogram, and phase errors from the optical and electronic responses of the various instrument components. Figures 2.3.2(a) and (b) show the interferogram and the corresponding raw frequency spectrum, respectively, of the internal ambient of our lab's spectrometer. The raw spectrum is composed of the responses from (i) the spectrometer: the light source, beam splitter, optical components, and ambient; (ii) the cryostat: the optical windows, sample holder, and sample; and (iii) the detector.

There are two important advantages of FT techniques over dispersive instruments, both of which ultimately arise from the time needed to conduct a measurement. The first advantage comes from the fact that the entire spectral output of a source is measured in the FT setup and is encoded in the interferogram. Since dispersive instruments measure a finite portion of the spectrum, there is a significant reduction in the amount of time required by the FT method to measure the entire spectrum with a desired S/N ratio. The gain in the S/N ratio of $n^{1/2}$, where n is the number of scans, of FT measurements over dispersive measurements is referred to as Fellgett's or the multiplex advantage. The second advantage, known as Jacquinot's or the throughput advantage, concerns the power of the signal measured at the detector. The diffraction gratings and slits used to separate

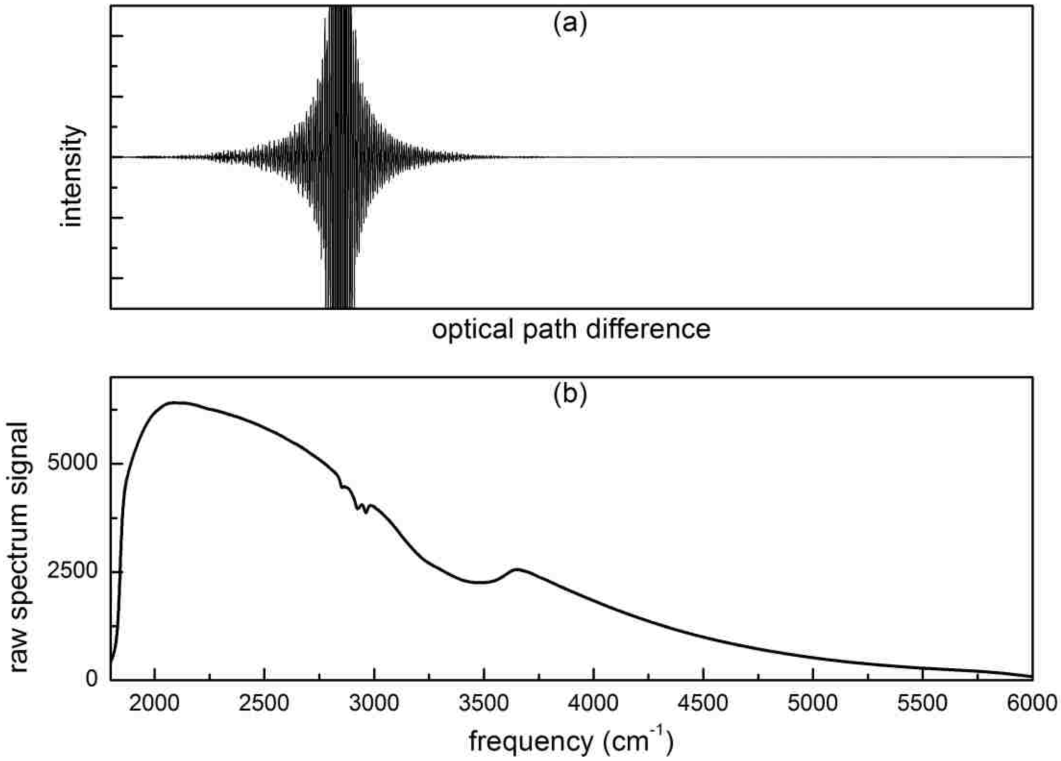

[redacted]

spectral regions in a dispersive instrument result in a large power loss and subsequently a decreased S/N ratio. Fourier transform instruments do not suffer from these power losses, which means a S/N ratio comparable to the best dispersive measurement can be achieved in a fraction of the time.

2.4: Instrumentation

2.4.1: Bomem DA3.16 FTIR spectrometer

All of the IR spectra presented in this dissertation were measured with a Bomem DA3.16 Fourier Transform Infrared (FTIR) spectrometer. The optical diagram of this instrument, shown in Fig. 2.4.1, is more complicated than the simple Michelson interferometer shown in Fig. 2.3.1. Light emitted by the source first passes through a variable diameter aperture (0.5 to 10 mm) to a flat transfer mirror and then to a collimating mirror. The collimated beam travels to the beam splitter and is split into the two beams, which travel to the fixed and moving mirrors. The position of the moving mirror as it traverses the scan tube is determined from the interferograms produced by a He-Ne laser and a white light source. The He-Ne laser also serves as a reference source for the frequency calibration of the instrument. A small prism directly below the center of the beam splitter passes light to a diode array on the outside of the instrument, which is used in the dynamic alignment process. The recombined beam is reflected by a mirror into either the left or right side of the source compartment, focused by another mirror onto the sample, and is finally focused onto the detector by a final mirror. The signal is sent to a preamplifier board, which uses a variable gain instrumentation amplifier to amplify the signal and selectively filter unwanted frequency components.

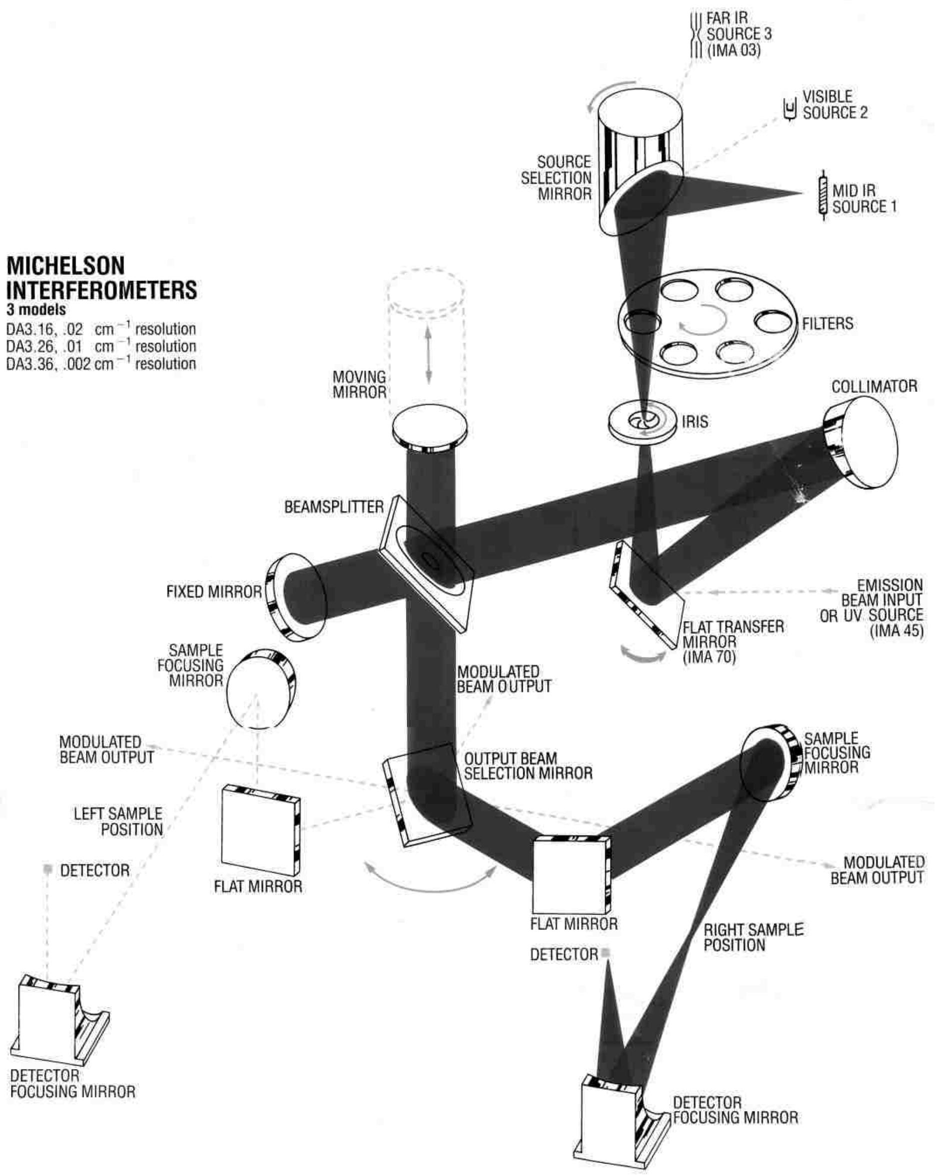

[redacted]

The Fast Fourier Transform (FFT) of the interferogram is performed on a Bomem PC-DA 3INT interface computer. All interferograms collected for this dissertation were apodized with the Hamming function and transformed. Transmission and absorbance spectra were calculated using Bomem’s GRAMS/AI software. Quantitative peak fitting was performed using Thermo Scientific’s PeakFit (version 4) software.

The Bomem DA3.16 FTIR spectrometer can be equipped with a variety of sources, beam splitters, and detectors for measurements in the far-IR (FIR), mid-IR (MIR), or near-IR (NIR) visible regions. The most common measurements of O-H and O-D LVMs use a globar source, a KBr beam splitter, and a liquid nitrogen cooled InSb detector. A roughing pump is used to evacuate the spectrometer to < 1.00 Torr, which reduces the background absorption by oil, water, and carbon dioxide vapors. The spectrometer pressure is further reduced by a liquid nitrogen cold trap present in one of the sample compartments.

The LVMs of defects can be broad at room temperature, with full-widths-at-half-maxima (FWHM) greater than 4 cm^{-1}, due to interactions with lattice phonons of the host crystal, which makes them difficult to detect. The raw spectra of (O-H)-defect-containing samples held at cryogenic temperatures (< 77 K) exhibit narrower line widths (FWHM ~ 0.5 cm^{-1}), which makes it easier to detect weak LVMs. Our lab is equipped with two different cryostats for obtaining IR spectra between 4.2 and 300 K. The Air Products Heli-Tran LT-3 cryostat, shown in Fig. 2.4.2, is a continuous flow cryostat and is relatively easy to operate. The sample is mounted on a Mo plate (to reduce mounting stress) using vacuum grease, and the plate is held on a cold finger at the bottom of the cryostat. The temperature of the sample is measured using a chromel/Au: 0.7 atomic % Fe thermocouple which is mounted just below the sample holder. A stainless-steel radiation shield surrounds the cold finger and blocks thermal radiation from the sample to help stabilize its temperature. Holes on either side of the shield permit light to pass through the sample. The cryostat sits in a stainless steel shroud, which is equipped with either a set of polished and wedged CaF_2 or CsI windows for MIR/NIR and FIR measurements, respectively.

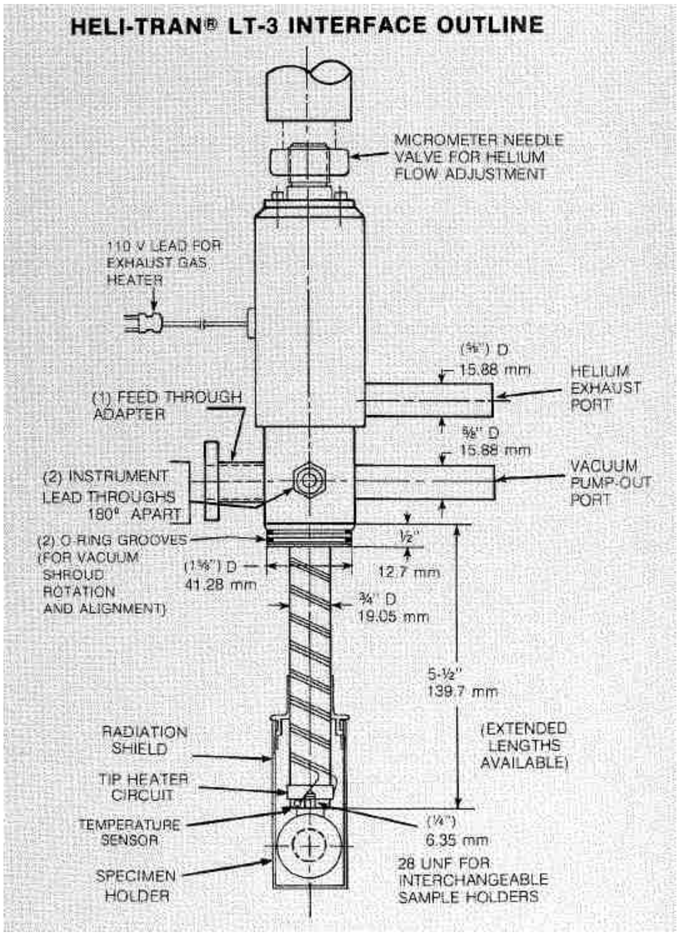

[redacted]

The 1-2° wedge of the windows eliminates the interference from multiply reflected beams that would be present with flat windows. The second cryostat, shown in Fig. 2.4.3, is an Oxford CF1204 continuous-flow model. The cryostat consists of an inner jacket, which contains the sample chamber surrounded by a radiation shield, and an outer jacket, which isolates the cryostat from the spectrometer. The space between the radiation shield and the outer jacket is evacuated to high vacuum (10^{-6} Torr). The sample is cooled directly with the liquid cryogen.

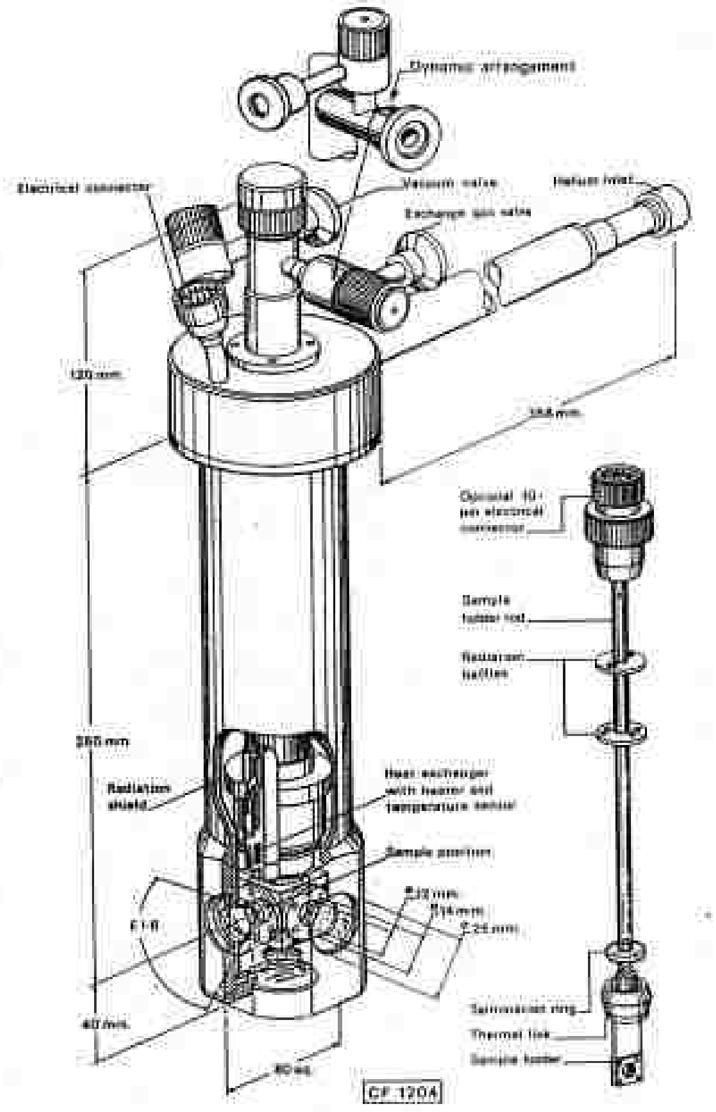

[redacted]

All of these factors allow this cryostat to stabilize its temperature to within ±0.1 K of a set temperature, which is invaluable for experiments in which such precision is necessary. The sample is mounted on a sample stick, usually with varnish, and sits in the sample chamber. The cryostats are evacuated using a two-stage pump system: an oil-roughing pump followed by a turbo pump, which can achieve high vacuum (< 10^{-6} Torr). A liquid-nitrogen-filled cold trap is placed in the line after the turbo pump to prevent contamination of the cryostats by oil vapor.

2.4.2: Uniaxial Stress Setup

Uniaxial stress measurements are performed in the Oxford cryostat using the custom built stress apparatus shown in Fig. 2.4.4. A pneumatic cylinder is pressurized with nitrogen gas, which creates the force that is applied to the sample. The gas pressure (in psi) is measured using a Marsh Master Test gauge and can be determined to within ±0.25 psi. A 3-inch diameter pneumatic cylinder applies stress to a stainless-steel rod which pushes on the sample. The gas pressure P_{gauge} and the sample stress P_{sample} are related by,

$$P_{\text{gauge}}A_{\text{cyl}} = P_{\text{sample}}A_{\text{sample}}. \qquad \textbf{Eq. (2.4.1)}$$

Thus, the stress applied to the sample can be calculated from,

$$P_{\text{sample}}(\text{MPa}) = \frac{P_{\text{gauge}}(\text{psi}) \times \pi r_{\text{cyl}}{}^2(\text{in.}) \times g(\text{m/s}^2)}{A_{\text{sample}}(\text{m}^2) \ \times 2.205 \text{ lbs/kg}}. \qquad \textbf{Eq. (2.4.2)}$$

The cross-sectional area of the sample can be measured with a micrometer to within 0.005 mm. Sample stresses can be as large as 500 MPa for GaAs and 1 GPa for Si. Figure 2.4.5 shows a more detailed view of the sample compartment of the stress apparatus. A good stress sample is a rectangular bar that has dimensions of 2 x 2 x 8 mm^3, with the long axis parallel to the push rod. It is crucial that the ends of the sample are flat and parallel or an inhomogeneous stress will result during measurements, which can alter the results of the experiment and break the sample.

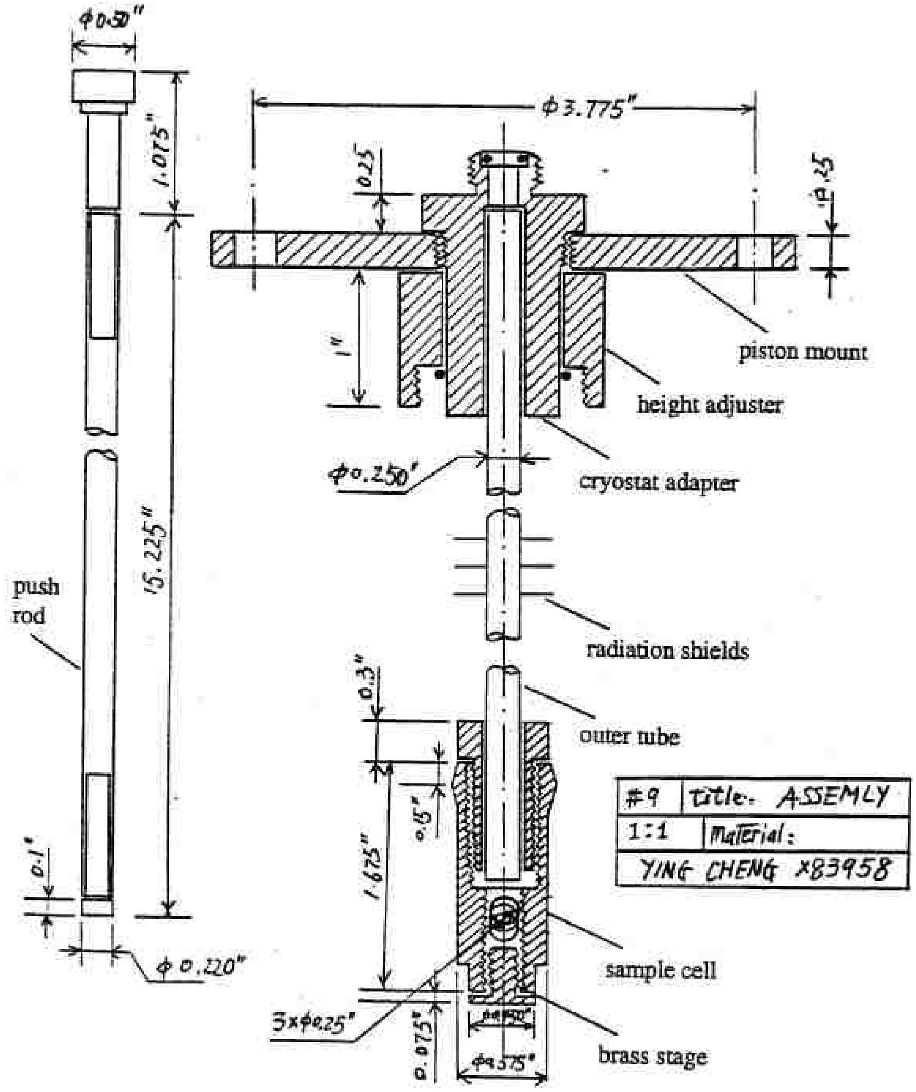

[redacted]

The sample is mounted on a copper cylinder, which is attached to the brass stage. The copper piece prevents the deformation of the brass stage. Similarly, a small copper cylinder is mounted to the end of the push rod to prevent the deformation of the rod during high stress experiments. A thin piece of indium foil is varnished onto the copper cylinder on the push rod to ensure that the stress is applied uniformly throughout the sample. Despite these precautions to ensure homogeneous stress, the top and bottom surfaces of the sample may experience some small inhomogeneities. Masking the top third and bottom third of the sample surface with Al foil or electrical tape prevents illumination of these regions. The mask decreases the intensity of the signal reaching the detector but also ensures that regions of the sample where the stress is most homogeneous are being examined.

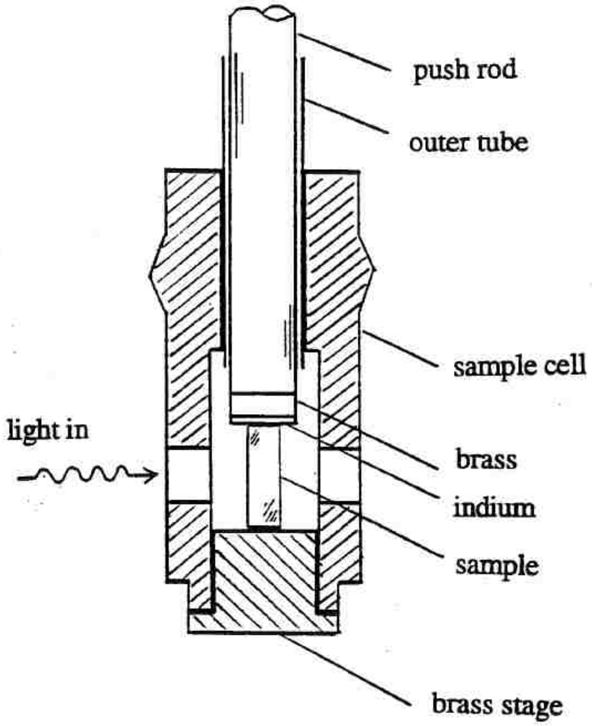

[redacted]

2.5: References

1. A. S. Barker & A. J. Sievers. Optical studies of the vibrational properties of disordered solids. *Rev. Mod. Phys.* **47,** S1 (1975). https://doi.org/10.1103/RevModPhys.47.S1.2

2. R. S. Leigh & R. C. Newman. An approximate treatment of localised vibrational modes. *Semicond. Sci. Technol.* **3,** 84 (1988).

3. R. C. Newman. Infra-red studies of crystal defects. (Taylor and Francis, 1973).

4. M. Fox. Optical Properties of Solids. 2nd ed. (Oxford University Press, 2010).

5. G. A. Shi. Physics of H in ZnO and H_2 in Si from Vibrational Spectroscopy. (Lehigh University, 2006).

6. P. Dawber & R. Elliot. Theory of Optical Absorption by Vibrations of Defects in Silicon. *Proc. Phys. Soc.* **81**, 453 (1963).

7. M. Stavola (ed.), Vibrational Spectroscopy of Light Element Impurities in Semiconductors, Chapter 3 in Identification of Defects in Semiconductors (ed. M. Stavola), Vol. 51B in *Semiconductors and Semimetals* (Academic Press, Boston, 1999).

8. P. Morse. Diatomic Molecules According to the Wave Mechanics. II. Vibrational Lines. *Phys. Rev.* **34,** 57 (1929).

9. G. Shi, *et al.* Identification of an OH-Li center in ZnO: Infrared absorption spectroscopy and density functional theory. *Phys. Rev. B* **73**, 081201(R) (2006).

10. F. Bekisli, *et al.* Bond angles for O-H defects in SnO_2 from polarization properties of their vibrational modes. *Phys. Rev. B* **85,** 205202 (2012).

11. A. A. Kaplyanskii. Computation of deformation splitting of spectral transision in cubic crystals. *Opt. Spectrosc.* **16,** 557 (1963).

12. A. A. Kaplyanskii. Noncubic centers in cubic crystals and their piezospectroscopic investigation. *Opt. Spectrosc.* **16,** 329 (1964).

13. A. E. Hughes & W. A. Runciman. Uniaxial stress splitting of doubly degenerate states of tetragonal and trigonal centres in cubic crystals. *Proc. Phys. Soc.* **90,** 827 (1967).

14. K. Bergman, *et al.* Structure of acceptor-hydrogen and donor-hydrogen complexes in silicon from uniaxial stress studies. *Phys. Rev. B* **38,** 9643 (1988). https://doi.org/10.1103/PhysRevB.35.2755

15. Y. M. Cheng & M. Stavola. Non-Arrhenius Reorientation Kinetics for the B-H Complex in Si: Evidence for Thermally Assisted Tunneling. *Phys. Rev. Lett.* **73**, 3419 (1994). https://doi.org/10.1103/PhysRevLett.73.3419

16. G. Cannelli, *et al.* Reorientation of the B-H complex in silicon by anelastic relaxation experiments. *Phys. Rev. B.* **44**, 486 (1991).

17. C. P. Flynn & A. M. Stoneham. Quantum Theory of Diffusion with Apllication to Light Interstitials in Metals. *Phys. Rev. B* **1**, 3966 (1970).

18. J. W. Corbett, *et al.* The configuration and diffusion of isolated oxygen in silicon and germanium. *J. Phys. Chem. Solids* **25**, 873 (1964).

19. D. C. Harris. Quantitative Chemical Analysis. 7th ed. (W. H. Freeman, 2006).

20. Bomem Spectrometer System and Software User's Manual. (1993).

21. Operating manual for Air Products Liquid Transfer LT-3 Helitran cryostat.

22. Operations manual for Oxford Instruments CF1204 continuous flow cryostat. (1988).

23. Y. Chen. Symmetry, Alignment, and Reorientation Mechanism for Hydrogen-Acceptor Complexes in Silicon and Gallium Arsenide. (Lehigh University, 1994).

Chapter 3

Quantitative Measurements of Free-Carrier Absorption

3.1: Introduction

Infrared absorption in semiconductors can arise from several different processes. The four most common of these are: (i) intrinsic absorption, in which an electron is excited from the valence band to any of the higher-energy conduction bands; (ii) absorption in which an impurity atom or lattice defect experiences an electronic or a vibrational excitation; (iii) phonon absorption, which involves the excitation of a vibrational mode (or multiple vibrational modes) of the host lattice; and (iv) free carrier absorption, in which an electron (hole) within the conduction (valence) band is excited to a higher energy state within the same band. The last process, free-carrier absorption, inhibits the successful application of TCOs for transparent contacts and flat-panel displays.

The classical Drude-Lorentz model for free-carrier absorption, which was given in Chapter 2 by Eq. (2.1.8), predicts that the free carrier absorption coefficient is proportional to the carrier concentration N and has a ω^{-2} dependence. The experimental studies in the 1950's and 1960's of free-carrier absorption in the elemental semiconductors, Si and Ge, and various III-V semiconductors show that the angular frequency dependence is,

$$\alpha = A'\omega^{-\beta}, \qquad \textbf{Eq. (3.1.1)}$$

or in terms of the wavelength λ,

$$\alpha = A\lambda^{\beta}. \qquad \textbf{Eq. (3.1.2)}$$

The coefficient β can vary between 1.5 and 3.5, and depends on the scattering process for the free carriers. A review of infrared absorption processes by Fan[1] shows that β is 1.5 for acoustic phonon scattering, 2 for neutral impurity scattering, 2.5 for optic phonon scattering, and 3-3.5 for ionized impurity scattering. Thus, free-carrier absorption can provide valuable information about both the carrier concentration and the dominant scattering mechanism.

Equation (2.2.5) from Chapter 2 gives an expression for the absolute transmission of a sample that accounts for the intrinsic absorption of the sample and reflections at the sample surfaces,

$$T = \frac{(1-R)^2 \exp(-\alpha d)}{1 - R^2 \exp(-2\alpha d)}; \quad R = \frac{|\tilde{n}-1|^2}{|\tilde{n}+1|^2}. \qquad \textbf{Eq. (3.1.3)}$$

One can solve for the absorption coefficient α by rearranging Eq. (3.1.3) into the form of a quadratic equation, $ax^2 + bx + c = 0$, which is given by,

$$TR^2 \exp(-2\alpha d) + (1-R)^2 \exp(-\alpha d) - T = 0.$$

Here, $x = \exp(-\alpha d)$. The positive solution to this equation yields a real value for *x*, from which one can solve for α,

$$\alpha = -\frac{1}{d} \ln\left\{\frac{A^2}{T}\left[\sqrt{1 + \left(\frac{T}{A^2 R}\right)^2} - 1\right]\right\}; \quad A^2 = \frac{(1-R)^2}{2R^2} \qquad \textbf{Eq. (3.1.4)}$$

Equation (3.1.4) can be used to calculate the absorption coefficient of a sample of thickness *d* using the complex refractive index $\tilde{n}$ and the transmission *T* at a specific wavelength λ. For TCOs, the imaginary part of the refractive index, *κ,* is usually much smaller than the real part, *n*, in the transparent spectral region and is therefore negligible. In this case, the reflectivity of a sample is given by,

$$R = \frac{|n-1|^2}{|n+1|^2}, \qquad \textbf{Eq. (3.1.5)}$$

and the transmission in the transparent spectral region is given by,

$$T = \frac{1-R}{1+R}. \qquad \textbf{Eq. (3.1.6)}$$

Early studies of free-carrier absorption in III-V semiconductors and TCOs used dispersive setups to measure the transmission of samples with different doping densities. The absorption coefficient was calculated using Eq. (3.1.4), and the dependences of the free carrier absorption coefficient (α_{FC}) on the wavelength of the incident radiation and the carrier density were determined. The free-carrier absorption in different *n*-type TCOs was studied by Baer[2] in reduced $SrTiO_3$, by Summitt and Borrelli[3] in SnO_2, and by Thomas[4] in ZnO single crystals doped with indium. This chapter presents the results of free carrier absorption measurements for ZnO single crystals using a FTIR spectrometer, so the results from the study by Thomas in ZnO are discussed in more detail below. The ZnO single crystals studied by Thomas had carrier concentrations between 3.7 x 10^{17} and 2.3 x 10^{19} cm^{-3}, as measured by the Hall effect. At room temperature, α_{FC} shows a wavelength dependence of $\beta = 3.0$, which suggests that ionized impurity scattering is the dominant scattering mechanism in these samples. On the other hand, α_{FC} shows a linear dependence on the carrier concentration N at a fixed wavelength, which suggests ionized impurity scattering cannot completely account for the scattering process. Additionally, α_{FC} shows the same wavelength dependence at 78 K as it does at 300 K, which suggests the scattering mechanism is independent of temperature.

Several groups have used FTIR spectroscopy to study the free-carrier absorption arising from hydrogen shallow donors in different TCOs. Bekisli *et al.*,[5] Yin *et al.*,[6] and

Lavrov[7] monitored the changes in the electrical conductivity of SnO_2, In_2O_3, and anatase-TiO_2 single crystals, respectively, using the fact that the strength of the absorption at a given frequency is proportional to the free-carrier concentration. There are many studies of the free-carrier absorption in ZnO due to the availability of large single crystals with surfaces of high optical quality. Shi *et al.*[8] calibrated the strength of the free carrier absorption in hydrogen-doped ZnO using Hall measurements. Emelie *et al.*[9] studied the free-carrier absorption between 700 and 4,000 cm^{-1} in bulk ZnO crystals grown by pressurized melt-growth (Cermet, Inc.) or hydrothermal growth (SPC Goodwill). Their fits to their absorption coefficient vs. wavelength data yielded $\beta = 2.3\pm0.1$ and 3.4 ± 0.1 for the melt-grown and hydrothermally grown samples, respectively, which implies the two crystals have different scattering mechanisms: polar optic phonon scattering and ionized impurity scattering. It is well known that different growth techniques can introduce different defects into the same type of sample. The scattering due to polar optic phonons indicates that the melt growth process introduces fewer impurities into the crystal than the hydrothermal growth process, where the scattering is due to ionized impurities. During the hydrothermal growth process, Li ions are incorporated into the crystal to act as acceptors and suppress the free-carrier absorption, which is consistent with the scattering mechanism determined by free carrier absorption. Saadatkia *et al.*[10] carried out FTIR measurements on ZnO films that were grown via two different methods (ALD vs. sol-gel); both films were intentionally doped with Al. The values of β for both films are less than 2, which indicate that LO phonon scattering is the dominant scattering mechanism in these materials.

As described in the previous paragraph, several groups have attempted to use FTIR spectroscopy to characterize free carrier absorption in TCOs, specifically ZnO. However, most of these studies do not address the actual measurement of the transmission spectra in enough detail for the experiments to be reproduced by other groups. The spectral range of the free-carrier absorption is usually limited between 400 and 5000 cm^{-1} due to the use of a MCT or an InSb detector. This limitation prevents the authors from comparing the measured sample transmission in the near IR (NIR) spectral region (~10,000 cm^{-1}) with the maximum transmission predicted by Eq. (3.1.3).

Kaplan and coworkers[11] investigated the possible sources of error on the radiometric (absolute transmission) accuracy for transmission measurements made on a FTIR spectrometer at room temperature. These sources include: (i) inter-reflections between the sample, the cryostat’s optical windows, and the spectrometer’s optical components; (ii) heating of the source aperture heating, and (iii) non-equivalence/non-linearity of the detector. Inter-reflections between the optical windows, the sample, and the mirrors in the sample compartment send light back into the interferometer, which interferes with the recombined beam. This effect is more prominent in samples with a high reflectivity. Heating of the source aperture causes the instrument aperture to emit blackbody radiation, thereby acting as a “second” source. This effect is inversely proportional to the diameter of the aperture, i.e., the smaller the aperture diameter, the larger the effect of its heating. Non-equivalence of the detector refers to the non-uniform response of the detector element to incident light. That is, two different areas on the same detector element may not generate the same response when illuminated with the same intensity of light. In most FTIR setups, light that has passed through a sample is focused onto the detector by a *f*/4 parabolic mirror, which reduces the area of the beam by a factor of four. Most of the detectors in the Stavola lab have active areas of 1.0 mm^2. Therefore, non-equivalence effects should be considered if the instrument aperture diameter is less than 3.5 mm or if the path length of the beam is significantly altered by the presence of the sample. Non-linear responses on detectors are generated when the amplitude of the interferogram is no longer linearly proportional to the intensity of the incident light. This effect is especially important for photoconductive detectors, such as MCT, InSb, and InGaAs detectors, where a large light flux can easily force the detector into a non-linear response.[12]

To better understand the effect of defects on the electrical conductivity of TCOs, it is important to have a procedure for measuring the transmission spectra (and therefore the absorption coefficient spectra) of these materials with high accuracy. This chapter presents the experimental methods that were developed for making quantitative transmission measurements across a broad spectral range (1000 to 12,500 cm^{-1}), at either 293 or 77 K, using an FTIR spectrometer. These methods are applied to several different hydrothermally grown ZnO samples to gain insight into the scattering mechanisms and the temperature dependence of the free-carrier absorption in this material.

3.2: Experimental Procedure

Hydrothermally grown zinc oxide (HT ZnO) samples from two different suppliers and with varying conductivities were provided by Professor Bengt Svensson from the Department of Physics at the University of Oslo, Norway. These samples, which were purchased from Tokyo Denpa Co., had carrier concentrations of 10^{15}, 10^{17}, and 2×10^{17}

cm^{-3}, with Al as the main *n*-type dopant. These samples are identified in subsequent sections as samples #1, #3, and #4, respectively. An as-grown sample from MTI Corporation, which was annealed at 1200°C in air to obtain a carrier concentration of ~2x10^{16} cm^{-3}, is identified as sample #2. Table 3.2.1 lists the thickness of each sample and summarizes their relevant electrical properties. To minimize reflections due to rough surfaces, the front and back surfaces of each sample were polished to optical quality on a Buehler Ecomet III polisher using a nylon cloth imbued with diamond paste. The sample surfaces were typically polished for at least 30 minutes to reach optical quality.

Table 3.2.1: Properties of the HT ZnO samples used for the free carrier absorption experiments.

Sample ID	Treatment	Thickness (mm)	Carrier density (cm^{-3})	Resistivity (Ω-cm)
#1: XGZ-0182-3 a.g.	as grown, Al-doped	0.545	1 x 10^{15}	82
#2: 1611011	as grown, 1200 °C anneal in air	0.505	2 x 10^{16}	n/a
#3: XGZ-0181-2 a.g.	as grown, Al-doped	0.530	1 x 10^{17}	0.1
#4: XGZ-0181-2 Zn	as grown, Al-doped Zn annealed	0.505	2 x 10^{17}	0.07

Table 3.2.2: Instrument settings used to acquire transmission spectra in different IR spectral ranges.

Spectral Range (cm^{-1})	Optical Window	Source	Beamsplitter	Detector
1000 – 2500	CsI	Globar	KBr	MCT
2500 – 5000	CaF_2	Globar	KBr	InSb
5000 – 9000	CaF_2	Quartz	Quartz	InSb
9000 – 12,500	CaF_2	Quartz	Quartz	Si p-d

Infrared transmission spectra were measured using a Bomem DA3.16 spectrometer under vacuum. Table 3.2.2 gives the combinations of the different light sources, beam splitters, and detectors used to analyze the mid infrared (MIR) and near infrared (NIR) spectral regions between 1000 and 12,500 cm^{-1}. A spectral resolution of 2 cm^{-1} was used for all measurements. Some of the suggestions by Kaplan *et al.*[11] were used to reduce the effects due to inter-reflections, heating of the source aperture, and non-equivalence of the detector the transmission spectra. Both the cryostat and the sample were tilted by several degrees relative to normal incidence to eliminate inter-reflections. The size of the samples limited the maximum diameter of the source aperture to 1.0 mm. To reduce the effect of source aperture heating, the light source was started an hour prior to transmission measurements to allow the radiation from both the source and the heated aperture to equilibrate. With the instrument aperture diameter set to 1.0 mm and no sample in the beam path, both the MCT and InSb detectors exhibited stable, linear responses. The signal generated by light incident as measured by the analog-to-digital converter (ADC) was 10% for the MCT detector and ~20% for the InSb detector. The ADC value on the Si p-d detector was saturated with the instrument aperture set to 1.0 mm. Therefore, measurements on this detector required a metal-mesh attenuator, tilted at ~10° to reduce interreflections, to be placed in the beam path, which gave an ADC value of 25%.

The HT ZnO samples were mounted on a Mo plate using vacuum grease, which was then attached to the cold finger of an Air Products Helitran cryostat. For all measurements, the spectrum of the empty Mo plate was used as the reference spectrum to calculate the transmission. The raw spectral signal of the empty Mo plate varied by as much as 5-10% over the course of one or two hours. To account for this “long term” drift in the signal, a reference spectrum was measured for each sample. At room temperature

(293 K), approximately 10 minutes elapsed between the measurements of the reference and the sample. Measurements at low temperature used liquid nitrogen to cool the sample. The process of cooling a sample from 293 to 77 K, measuring the spectrum, and warming the sample from 77 to 293 K, takes about 90 minutes.

The transmission measurements are specified by the detector/source/beamsplitter combination. For the InSb/Quartz/Quartz and Si/Quartz/Quartz measurements, there was no measurable difference between the raw spectra taken at 293 K vs. the raw spectra taken at 77 K. On the InSb/Glob/KBr setup, the signal for the raw spectrum at 77 K was found to be smaller than the signal for the raw spectrum at 293 K by almost 10%. Therefore, for low temperature transmission measurements on the InSb/Glob/KBr setup, the reference spectrum was also measured at 77 K, whereas on the InSb/Quartz/Quartz and Si/Quatz/Quartz setups, the reference spectra were measured at 293 K.

The transmission vs. wavenumber spectra were converted to transmission vs. wavelength (in microns) spectra using a routine in GRAMS/AI. The absorption coefficient (in m^{-1}) at each wavelength was calculating according to Eq. (3.1.4) using a program written in MATLAB by Andrew Shapiro (Lehigh University, Class of 2016). This program is included in Appendix A. The input parameters for the program are the transmission vs. wavelength spectra in the different spectral regions for a single sample, the real and complex parts of the refractive index in the transparent spectral region, and the sample thickness (in mm). For samples that show free-carrier absorption, the wavelength dependence of the absorption coefficient was determined from a least squares fit to the log-log plot of the absorption coefficient vs. wavelength. The user defines the starting and ending wavelengths for the fit region.

3.3: Experimental Results

3.3.1: Room-Temperature (293 K) Measurements

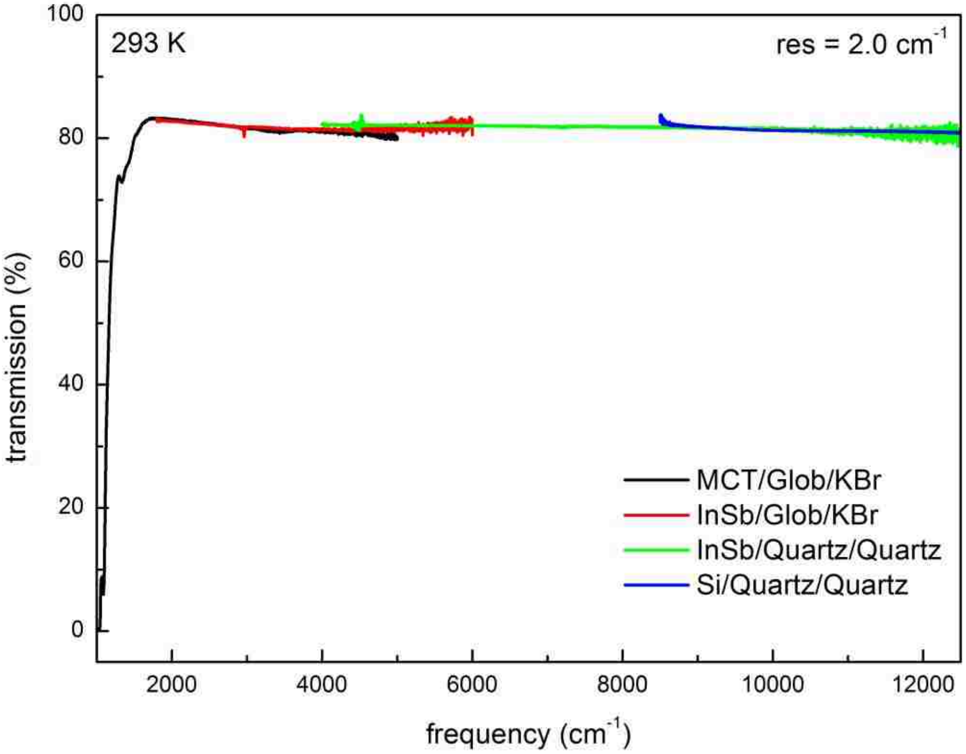

[redacted]

Figure 3.3.1 shows the transmission spectra of a HT ZnO sample (N~10^{15} cm^{-3}) for the four different setups listed in Table 3.2.2. The sample did not show free-carrier absorption in the MIR or NIR spectral regions. The transmission spectrum for each setup is presented “as-measured”, meaning no vertical offsets have been applied to align the spectra on top of one another. The manufacturer of our FTIR spectrometer, ABB Bomem, evaluates the stability of an FTIR spectrometer by using the 100% open-beam response, which is the transmission spectrum calculated from two successive measurements of the empty, evacuated spectrometer. Ideally, the transmission spectrum should have an average value of 100%, and the fluctuations in this value are indicative of the accuracy of the measurement. For a DA3.16 instrument equipped with a MCT detector, a globar source, and a KBr beam splitter, ABB Bomem specifies a minimum stability of ±0.3% stability at 3000 cm^{-1}. The “as-measured” transmission spectra can be used to estimate the accuracy of the experimental technique presented in Section 3.2. ZnO crystallizes into the wurtzite structure, which is characterized by two different indices of refraction that are ∥ and ⊥ to the *c*-axis. The HT ZnO crystals used in these experiments are *c*-cut, which means the *c*-axis is normal to the sample surface. Therefore, the samples should be birefringent at visible wavelengths of light. However, in the transparent region, the refractive indices $n_{\parallel}$ and $n_{\perp}$ are approximately the same and have a value of 1.95. Substituting this value into Eq. (3.1.6) gives a maximum theoretical transmission for ZnO of 81.2%. All of the experimental transmission spectra fall within ±1 % of this value, which shows that the technique described in Section 3.2 can be used to measure the frequency-dependence of the transmission of a sample at room temperature accurately using an FTIR spectrometer.

Figure 3.3.2 shows the transmission spectra in Fig 3.3.1 but with a small vertical offset (<1%) applied to measurements using an InSb/Glob/KBr, an InSb/Quartz/Quartz, and a Si/Quartz/Quartz setups. The transmission spectra presented in the remainder of this chapter are aligned across the entire spectral region by offsetting the spectra measured using the InSb/Quartz/Quartz and Si/Quartz/Quartz setups with respect to spectra measured using the MCT/Glob/KBr or InSb/Glob/KBr setups.

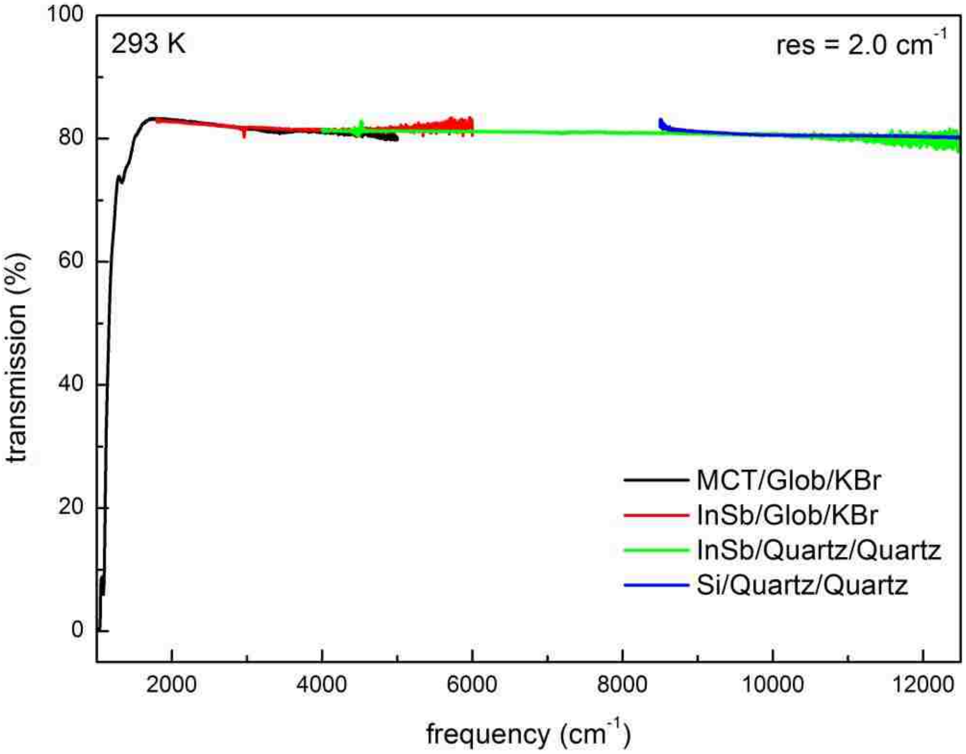

[redacted]

The transmission vs. frequency spectra of four different HT ZnO samples measured at 293 K are shown in Fig 3.3.3. Samples #2, #3, and #4, which have carrier concentrations of 2x10^{16}, 10^{17}, and 2x10^{17} cm^{-3}, show free carrier absorption between 1000 and 8000 cm^{-1}. The absorption in samples #3 and #4 is stronger than the absorption in sample #2. The maximum transmission of sample #2 is slightly larger (84.5%) than the expected 81.2%; samples #3 and #4 have transmission maxima that are slightly lower (~76%) than the expected value.

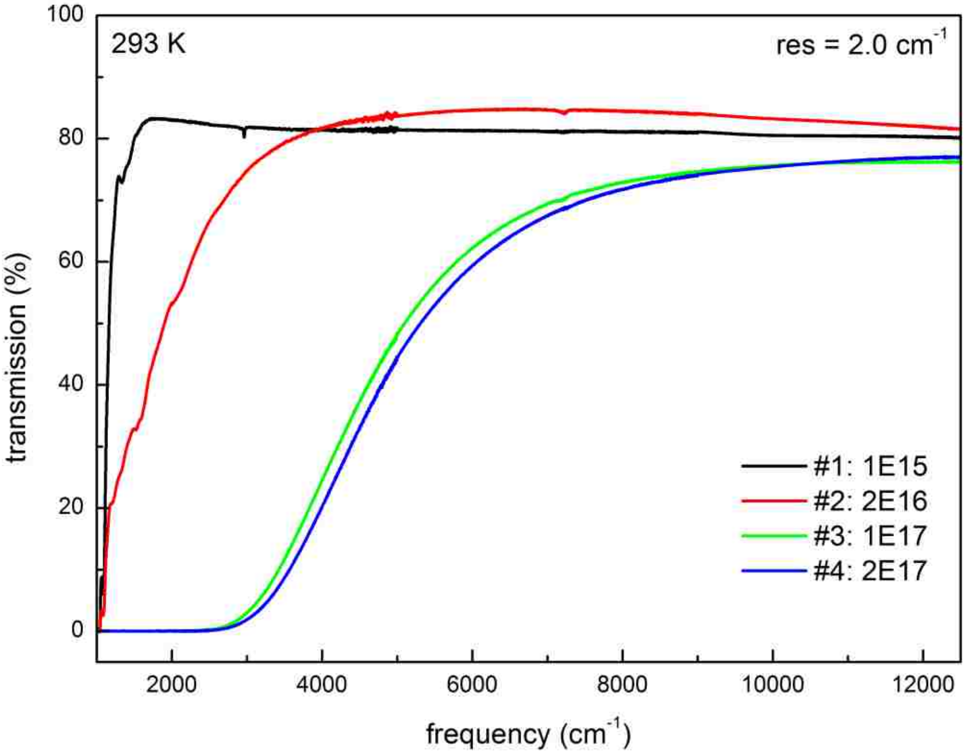

[redacted]

These measurements show that a typical deviation from the theoretical maximum transmission of ~4-5% can be expected for these measurements.

The *x*-axes of the transmission spectra shown in Fig. 3.3.3 were converted from wavenumber to wavelength (μm), and the absorption coefficient (cm^{-1}) vs. wavelength spectra were calculated according to Eq. (3.3.4) using the MATLAB program. For these calculations, the imaginary part of the refractive index (the extinction coefficient κ) was set equal to zero. The transmission vs. wavelength spectra and the absorption coefficient vs. wavelength spectra are presented in the left and right panels of Fig. 3.3.4.

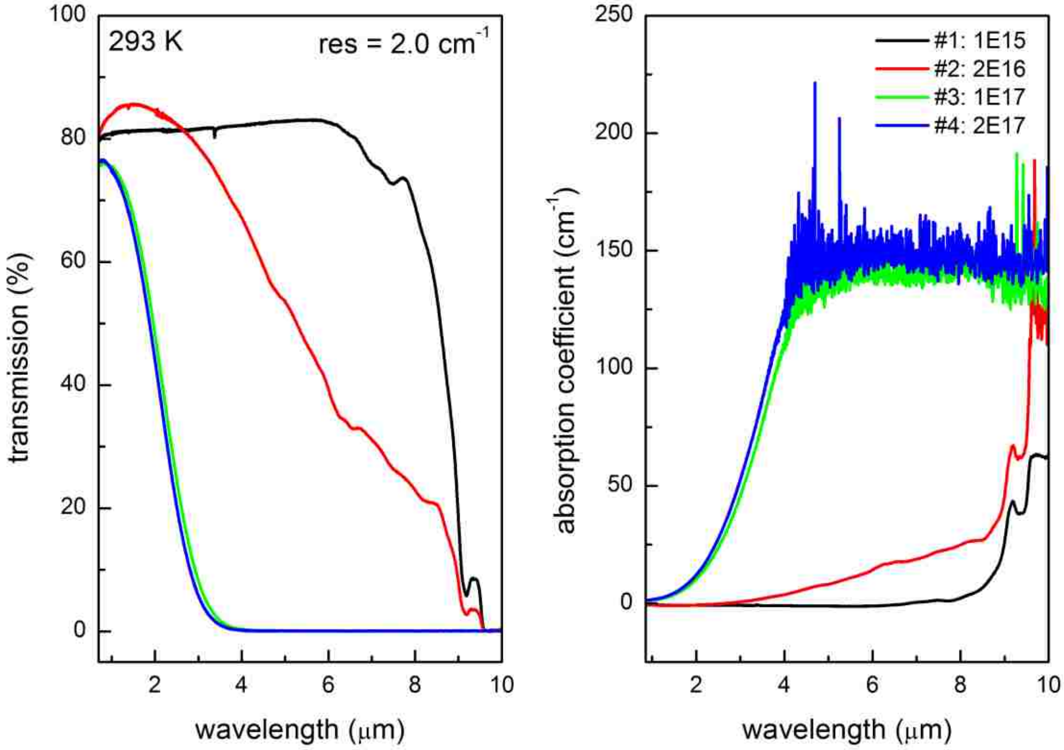

[redacted]

Samples #1 and #2 show two broad absorption features at λ = 9.17 and 9.70 μm; these features are completely masked by the free-carrier absorption in samples #3 and #4. These peaks have been observed in previous FTIR studies[9,10] of ZnO and were attributed to lattice absorption due to two different multi-phonon absorption modes. Additional weak features are present between 4 and 9 μm. Thomas observed similar features in an as-grown ZnO crystal, and hypothesized that the peaks could originate from lattice absorption.[4] These peaks are completely masked by the strong free carrier absorption samples #3 and #4. Although their identity was not investigated further, care was taken to not let these peaks affect the fits to the absorption coefficient vs. wavelength data for sample #2.

Both samples #3 and #4 show strong free-carrier absorption that increases starting at 1 μm and achieves a constant value for wavelengths beyond 3 μm, (The data are quite noisy at this value due to the small amount of light transmitted). The absorption coefficient spectra can be used to check the validity of setting κ = 0 for the initial calculation. The relationship between κ and α is given by Eq. (3.3.1),

$$\kappa = \frac{\alpha\lambda}{4\pi}. \qquad \textbf{Eq. (3.3.1)}$$

From Fig. 3.3.4, it can be seen that $\alpha \sim 100\ \text{cm}^{-1}$ at $\lambda = 4.0$ μm. Substituting these values into Eq. (3.3.1) gives,

$$\kappa \sim \frac{100\ \text{cm}^{-1} \cdot 4 \times 10^{-4}\text{cm}}{4\pi} = 0.003.$$

The extinction coefficient can be neglected if $\kappa^2 \ll 1$. Samples #3 and #4 both satisfy this condition.

The frequency- or wavelength-dependence of the absorption coefficient in the spectral region, where free-carrier absorption is the dominant absorption process, gives insight into the primary scattering mechanism of the carriers. The dependence of the absorption coefficient on the wavelength was given in Section 3.1 by Eq. (3.1.2),

$$\alpha = A\lambda^{\beta}. \qquad \textbf{Eq. (3.1.2)}$$

To investigate the carrier-scattering mechanisms in these samples, the absorption coefficient vs. wavelength data were plotted on a log-log scale reveal the power-law relationship between α and λ. The slope of the fit through the free carrier data is equal to β, and the y-intercept is equal to log(*A*).

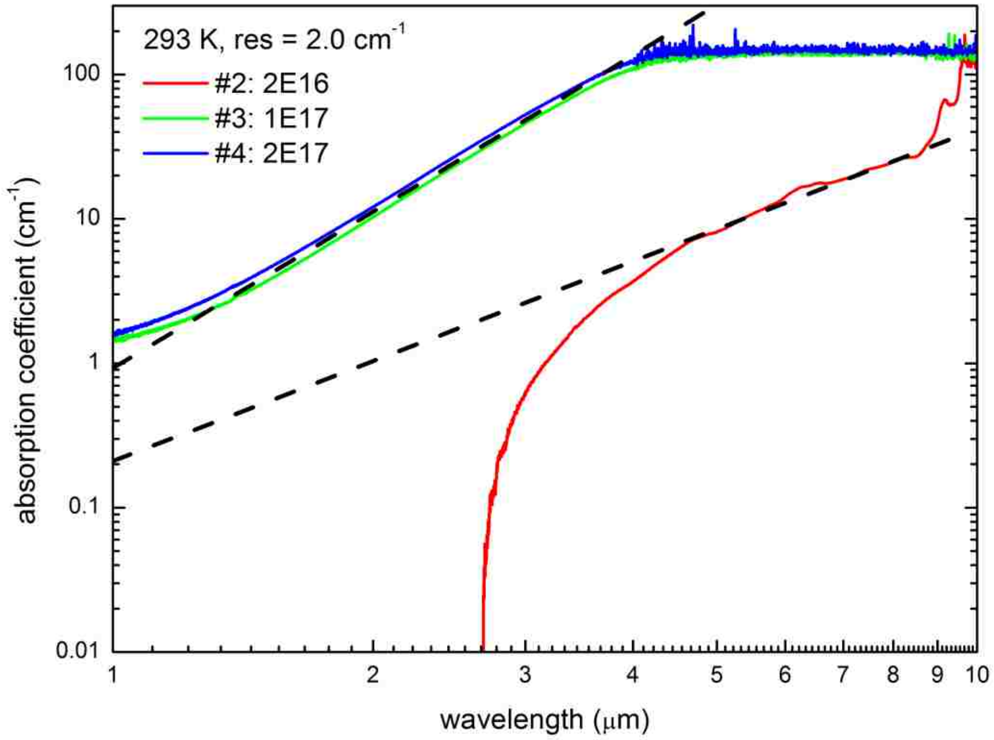

[redacted]

Figure 3.3.5 shows a log-log plot of the absorption coefficient vs. wavelength spectra for samples #2, #3, and #4. The fit regions and the fit parameters, A and β, for each of the three samples are listed in Table 3.3.1. The dashed lines shown in the figure have slopes equal to the values of β listed in Table 3.3.1. The values of β are 3.7 for samples #3 and #4 and 2.3 for sample #2.

Table 3.3.1: Fit parameters for absorption coefficient vs. wavelength spectra of HT ZnO samples #2, #3, #4 at 293 K.

Sample	Temperature (K)	λ_{start} (μm)	λ_{end} (μm)	A (cm^{-1})	β
#2	293	5.0	8.0	0.224	2.3±0.1
#3	293	1.5	3.0	0.763	3.7±0.1
#4	293	1.5	3.0	0.960	3.7±0.1

The values of $\beta = 3.7$ for samples #3 and #4 suggest that scattering of ionized impurities is the dominant scattering mechanism in these samples. These samples are *n*-type and doped with Al, which is consistent with this scattering mechanism. This result could be confirmed by measuring additional Al-doped HT ZnO samples from Tokyo Denpa with carrier concentrations ranging between 10^{16} and 10^{19} cm^{-3}. The value of β for sample #2 suggests that the carrier scattering in this sample is primarily due to the interactions of the carriers with optic phonons. Sample #2 was annealed in air at 1200 °C to obtain a carrier density of 2×10^{16} cm^{-3}. The difference in β between the two sets of samples indicates that the donor(s) that are responsible for the free-carrier absorption in samples #3 and #4 have substantially higher concentration than the donor(s) that are responsible for the free-carrier absorption in sample #2.

In summary, the experimental procedure developed in Section 3.2 was successfully used to characterize the transmission of a set of HT ZnO single crystals across the spectral range from 1000 to 12,500 cm^{-1} at 293 K. The dominant scattering mechanisms in samples showing free-carrier absorption were determined by analyzing the dependence of the absorption coefficient on the wavelength.

3.3.2: Low-Temperature (77 K) Measurements

Of the four HT ZnO specimens, samples #3 and #4 show the strongest free carrier absorption. To investigate the temperature dependence of the free carrier absorption in these samples, transmission spectra were measured at 77 K as described in Section 3.2.

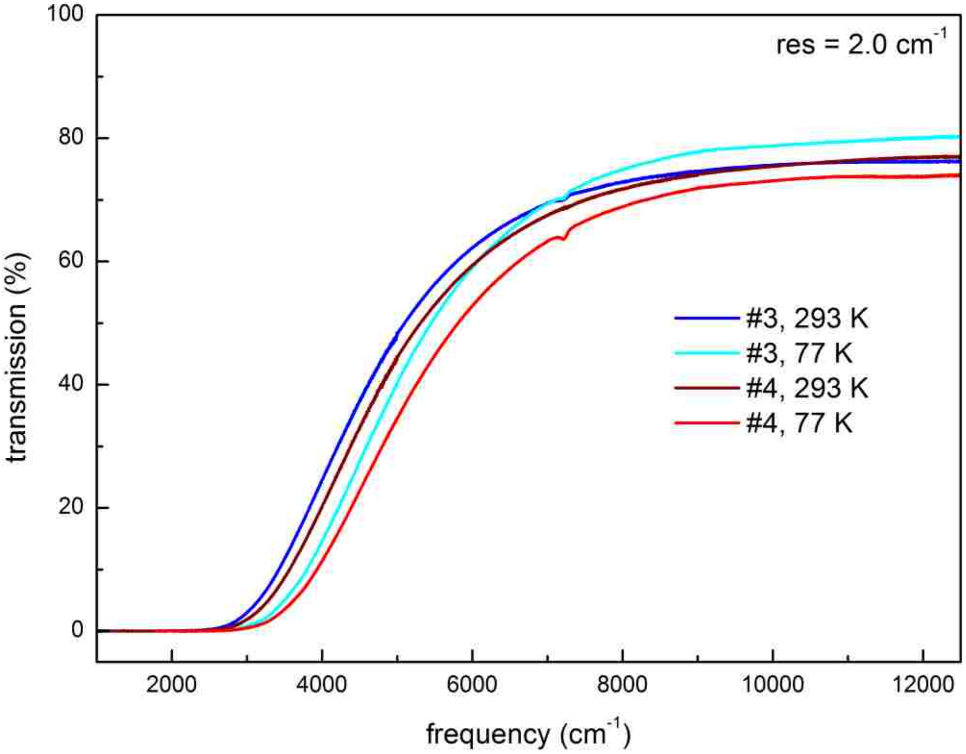

[redacted]

Figure 3.3.6 shows the transmission vs frequency spectra of samples #3 and #4 at both 293 and 77 K from 1000 to 12,500 cm^{-1}. In the high wavenumber limit, the maximum transmission values of both of the samples fall within 5% of the room temperature values. Thus, even with the additional 80 minutes required to warm the empty sample holder from 77 to 293 K, mount the sample and evacuate the cryostat, and cool the sample from 293 to 77 K, an accuracy of about 5% was maintained. The weak feature present at 7000 cm^{-1} is due to absorption by the quartz beam splitter and is an artifact seen for the InSb/Quartz/Quartz setup.

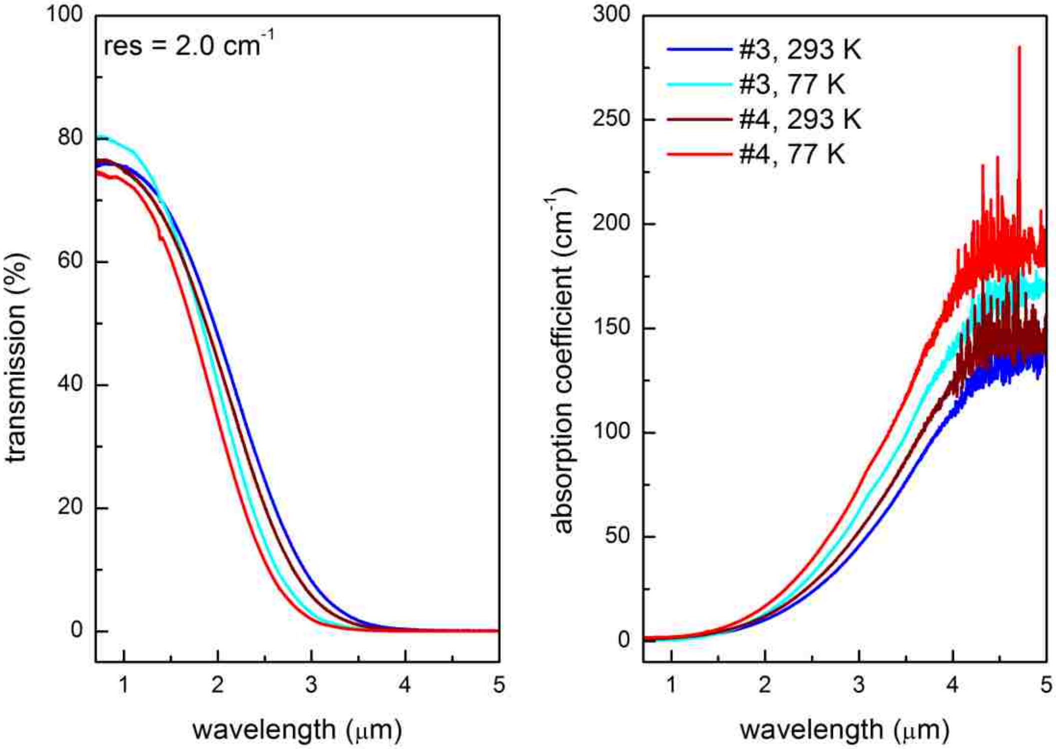

[redacted]

Figure 3.3.7 shows spectra of the transmission vs. wavelength and absorption coefficient vs. wavelength for samples #3 and #4 at both 293 and 77 K. Interestingly, both of the samples show a *smaller* transmission (*larger* absorption) at 77 K than at 293 K in the free-carrier absorption region. This effect is large enough in magnitude (~10%) to be outside experimental error and is reproducible in both samples across multiple days. The increased absorption is most apparent in the right panel of Fig 3.3.7 in the free-carrier spectral region between 2 and 4 μm.

The decrease in the transmission upon cooling the sample from 293 to 77 K seems counter-intuitive. By definition, the electronic energy levels of an *n*-type shallow donor are located just below the conduction band minimum of the host crystal. There is usually enough energy available at room temperature to thermally excite an electron of the donor into the conduction band, giving rise to electrical conductivity, and thus free-carrier absorption. If a sample is cooled to a sufficiently low temperature such that the thermal energy $k_B T$ is small compared to the energy difference between the conduction band minimum and the shallow donor state, then the electron will remain localized at the donor and will not contribute to the electrical conductivity. Therefore, one would expect the absorption due to free carriers to decrease, and consequently, the transmission in this region should *increase* by cooling the sample to 77 K.

The situation is, however, more complicated than simply freezing out the free carriers. When electrons become bound to their positive-ion cores at low temperature, the free-carrier absorption is replaced by the hydrogenic continuum absorption associated with a neutral donor center. So, broad low-frequency absorption persists even below freeze-out. Thomas noted a similar effect in his studies of ZnO single crystals; cooling the samples from 293 to 77 K decreased the electrical conductivity (and therefore the carrier concentration) by a factor of 100 but increased the transmission in the free-carrier absorption spectral region only by ~10%.[4] Even though the electrical conductivities for samples #3 and #4 at 77 K are not known, the increases in the transmission of both samples are on the order of 10%. Thomas speculated that the donor electrons, which are bound at low temperatures, could absorb IR radiation and undergo transitions to a higher energy band, as was observed in Si.[13] However, it is difficult to draw a conclusion concerning the nature of the temperature dependence of the absorption coefficient based on these data alone.

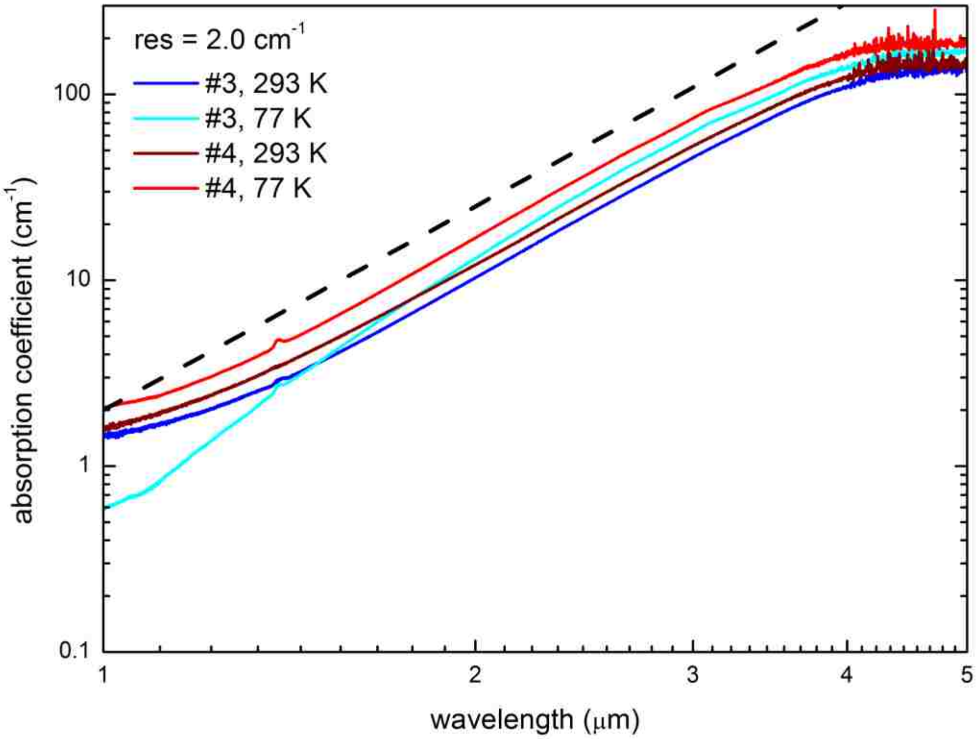

[redacted]

Table 3.3.2: Fit parameters for absorption coefficient vs. wavelength spectra of HT ZnO samples #3 and #4 at 77 K.

Sample	Temperature (K)	λ_{start} (μm)	λ_{end} (μm)	A (cm^{-1})	β
#3	77	2.0	3.0	0.949	3.8±0.1
#4	77	2.0	3.0	1.37	3.6±0.1

Figure 3.3.8 shows a log-log plot of the absorption coefficient vs. wavelength spectra shown in the right panel of Fig. 3.3.7. The dashed line shown above the spectra has a slope of 3.7, which is consistent with the slopes of the absorption coefficient vs. wavelength data between 2.0 and 3.0 μm for sample #3 at 293 K and sample #4 at both 293 and 77 K. The slope of sample #3 at 77 K is larger in magnitude (~3.8) than the slope at 293 K, because its maximum transmission value is about 5% higher than the other measurements. Within error, this slope is still consistent with ionized impurity scattering being the dominant scattering mechanism at 77 K.

In summary, the free carrier absorption of two Al-doped HT ZnO samples has been successfully measured quantitatively at 77 K. The dominant scattering mechanism is unchanged at both 293 and 77 K. However, cooling the sample to 77 K increases the strength of the transmission by about 10% relative to 293 K in the free carrier absorption spectral region.

3.4: Discussion

Up to now, FTIR measurements of free-carrier absorption in *n*-type TCOs in the literature have been hindered by limited spectral ranges (< 5000 cm^{-1}), or have omitted critical details about the experiment. The experimental procedure described in Section 3.2 is easy to implement in a standard FTIR instrument can be used to measure transmission spectra of TCOs quantitatively between 1000 and ~12,000 cm^{-1} at temperatures between 4.2 and 293 K. In principle, it is possible to extend the spectral range of these measurements to both lower and higher wavenumbers by using other combinations of detectors, sources, and beam splitters. For example, a setup containing a Si photodiode detector, a quartz source, and an Al-coated UV quartz beam splitter can be used to measure spectra between 15,000 and 25,000 cm^{-1}. However, the boundary between NIR radiation and visible radiation is around 15,000 cm^{-1} (red-wavelengths); thus, it might be more practical to measure the UV/VIS spectral range on a dispersive spectrophotometer rather than on a FTIR instrument.

The transmission vs. frequency spectra of bulk, *n*-type HT ZnO samples were converted to absorption coefficient vs. wavelength spectra and analyzed to determine the dominant scattering process in these samples. Samples #3 and #4, which were grown by Tokyo Denpa, showed β=3.7, which suggests the carriers undergo scattering by ionized impurities. As these samples are bulk doped with Al to obtain the *n*-type conductivity, this carrier-scattering mechanism determined by experiment is consistent with a simple model in which Al substitutes into the lattice at a Zn site and donates its electron to the conduction band. The value of β remains the same, within error, for the measurements at both 293 and 77 K, so scattering by ionized impurities is likely the dominant scattering mechanism at both temperatures. The values of β determined by these experiments are higher than those determined by Thomas[4] (3.0±0.1) and close to those determined by Emelie *et al.*[9] (3.4±0.1). Emelie *et al.*[9] purchased their HT ZnO sample from a commercial source (SPC Goodwill), but the crystals used by Thomas were grown in his own laboratory. The details of how he grew the ZnO crystals used in these experiments are absent from his paper. Without these details, it is difficult to determine the cause of the difference between the values of β determined from his dispersive experiments and our FTIR measurements. Sample #2 from MTI Corporation, which has a lower carrier density of 2x10^{16} cm^{-3}, showed β=2.3, which suggests the dominant scattering mechanism in this sample is scattering by polar optic phonons.

For samples #3 and #4, the strength of the free-carrier absorption at 77 K increased relative to the strength of the free-carrier absorption at 293 K. Thomas observed a similar result in his experiments and speculated that electrons bound in impurity states could be excited to a higher energy band in the crystal, giving rise to the observed increase in the absorption strength.

3.5: Conclusion

Experimental procedures were developed for quantitatively measuring the transmission of a material in different spectral ranges and at different temperatures using an FTIR spectrometer equipped with different detectors (MCT, InSb, and Si), light sources (globar and quartz sources), and beam splitters (KBr and quartz). This procedure is simple to implement and achieves an accuracy of ±5% by reducing the effects of inter-reflections, heating of the source aperture, and non-equivalence/non linearities on the spectral response of the detector. The carrier-scattering mechanisms of several HT-grown ZnO samples were determined at 293 and 77 K using this procedure. Future projects could investigate the wavelength dependence of the absorption coefficient on a larger set of samples for a single material, e.g., single crystal ZnO produced by melt-growth, chemical vapor transport, and hydrothermal growth, or across several different TCOs with similar doping concentrations. These data would be invaluable for theorists who are using first-principles calculations to predict the free-carrier-absorption spectra.

3.6: References

1. H. Y. Fan, H. "Effects of Free Carriers on the Optical Properties", Chapter 9 in Optical Properties of III-V Compounds, Vol. 3 in the series *Semiconductors and Semimetals* (eds. R. K. Willardson & A. C. Beer) (Academic Press, 1967).

2. W. S. Baer. Free-carrier absorption in reduced $SrTiO_3$. *Phys. Rev.* **144**, 734 (1966).

3. R. Summitt & N. F. Borrelli. Infrared absorption in single crystal stannic oxide. *J. Phys. Chem. Solids* **26,** 921 (1965).

4. D. G. Thomas. Infrared absorption in zinc oxide crystals. *J. Phys. Chem. Solids* **10**, 47 (1959).

5. F. Bekisli, *et al.* Hydrogen impurities and shallow donors in SnO_2 studied by infrared spectroscopy. *Phys. Rev. B* **84,** 035213 (2011).

6. W. Yin, *et al.* Hydrogen centers and the conductivity of In_2O_3 single crystals. *Phys. Rev. B* **91,** 075208 (2015).

7. E. V. Lavrov. Hydrogen donor in anatase TiO_2. *Phys. Rev. B* **93,** 045204 (2016).

8. G. A. Shi, *et al.* Hydrogen local modes and shallow donors in ZnO. *Phys. Rev. B* **72**, 195211 (2005).

9. P. Y. Emelie, *et al.* Free carrier absorption and lattice vibrational modes in bulk ZnO. *J. Elec. Mater.* **35**, 525 (2006).

10. P. Saadatkia, *et al.* Fourier Transform Infrared Spectroscopy Measurements of Multi-phonon and Free-Carrier Absorption in ZnO. *J. Elec. Mater.* **45,** 6329 (2016).

11. S. G. Kaplan, *et al.* Testing the radiometric accuracy of Fourier transform infrared transmittance measurements. *Appl. Opt.* **36,** 8896 (1997).

12. D. B. Chase. Nonlinear detector response in FT-IR. *Appl. Spectrosc.* **38,** 491 (1984).

13. W. Spitzer & H. Y. Fan. Infrared Absorption in *n*-Type Silicon. *Phys. Rev.* **108,** 268 (1957).

Chapter 4

Uniaxial Stress Studies of O-H Centers in In_2O_3

Copyright Disclaimer: Portions of this chapter, including text and figures, are reprinted from P. Weiser, *et al.* Appl. Phys. Lett. **109**, 202105 (2016), with permission of AIP Publishing.

4.1: Introduction

Indium (III) oxide (In_2O_3) is a TCO with the cubic bixbyite structure shown in Fig. 4.1.1 that contains 80 atoms per cubic cell.[1] All of the O atoms are equivalent, but there are two types of In sites, In(1) and In(2), as shown in Figs. 4.1.2(a) and (b). In(1) and In(2) comprise 25% and 75% of the In sites, respectively.

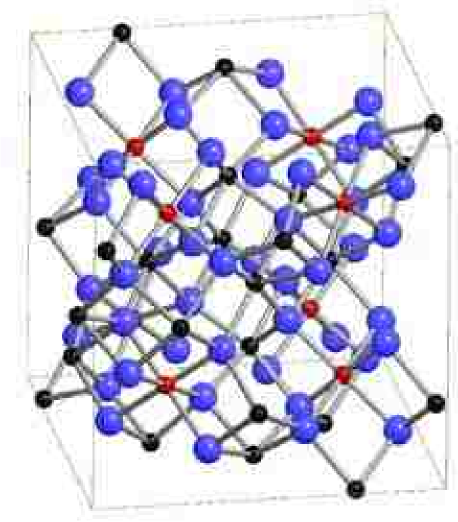

[redacted] blue red

The difference between these sites is the arrangement of the bonds with their neighboring O atoms. For In(1), all six In-O bond lengths are equal, and the adjacent O-In(1)-O bond angles are 80° or 100°. The structure of In(2) has a lower symmetry than In(1), and has three pairs of inequivalent O-In(2)-O bonds. Figure 4.1.2(c) shows the O site, which is coordinated with one In(1) atom and three In(2) atoms.[2]

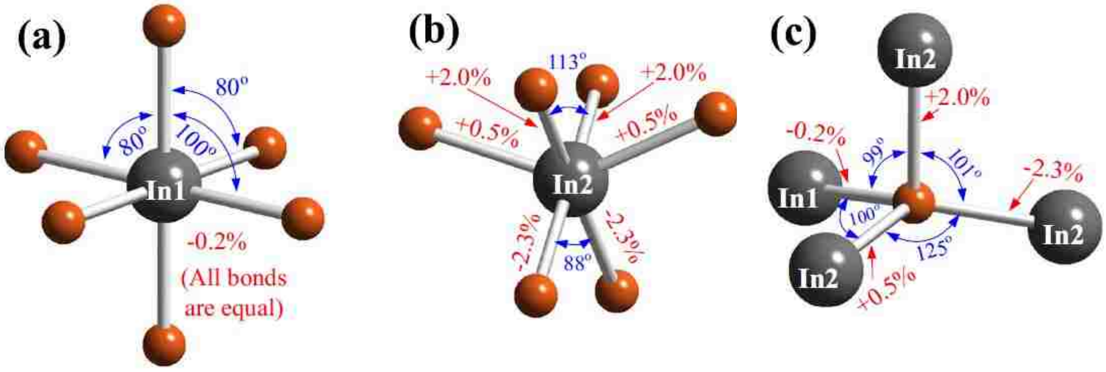

[redacted]

In_2O_3 doped with tin (Sn) is a highly conductive *n*-type alloy, commonly known as indium-tin oxide or ITO, and is the most widely used TCO. Thin films of ITO have found widespread applications as coatings for low-emissivity windows[3] and as transparent electrodes for light-emitting diodes, solar cells, and flat panel displays. Undoped In_2O_3 thin films and single crystals still show a strong *n*-type conductivity that has traditionally been attributed to oxygen vacancies and cation interstitials. The mechanisms to explain this unintentional conductivity have recently been challenged by both experiment and theory, which suggest that hydrogen centers are important shallow donors. Thin films of In_2O_3 doped with hydrogen exhibit *n*-type conductivity with a high carrier mobility.[4] Muon-spin-resonance experiments[5,6] show that implanted muons, whose properties can mimic those of hydrogen, form shallow donors in In_2O_3 powders. Density functional theory (DFT) calculations[2] predict that both interstitial hydrogen (H_i)

and hydrogen trapped at an oxygen vacancy (H_O) will act as shallow donors. More recently, Yin *et al.*[7] investigated hydrogen centers in In_2O_3 single crystals grown by the flux method at Oak Ridge National Lab. Many of the as-grown crystals show vibrational lines in the O-H stretching region. They found that treating In_2O_3 single crystals in a hydrogen (deuterium) ambient produced a complicated multiline spectrum in the O-H (O-D) stretching region.

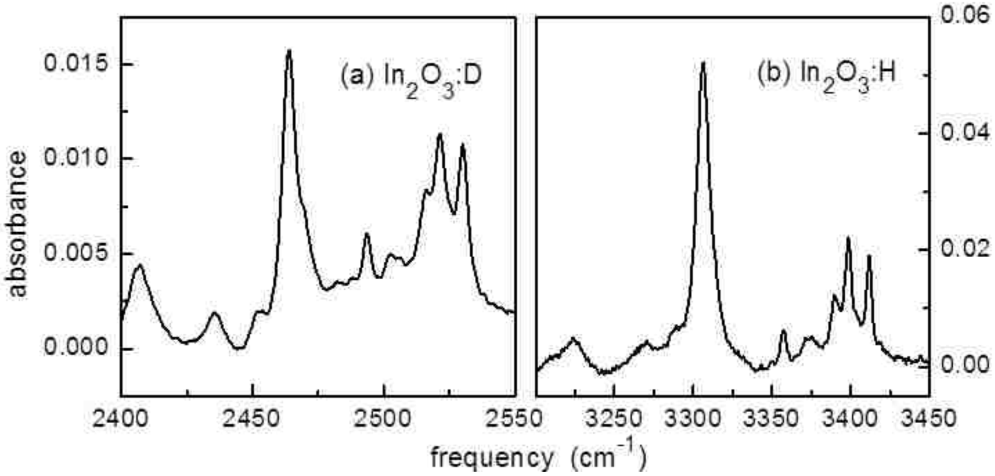

[redacted]

Figure 4.1.3 shows the IR-absorbance spectra measured at 4.2 K in these two regions. Samples annealed in a mixture of H_2 and D_2 did not display any additional LVMs, which suggests that these vibrational lines arise from O-H and O-D centers containing a single H or D atom. The H_2 and D_2 treatments also resulted in broad free-carrier absorption which becomes stronger at lower frequencies. To determine if any of the O-H centers were responsible for the free-carrier absorption, two sets of experiments were carried out whose results are shown in Fig. 4.1.4. In the first experiment (Fig. 4.1.4(a)), D-treated samples were subjected to isochronal anneals for 30 min. at successively higher temperatures which eliminated both the free-carrier absorption and the O-D vibrational lines. The decay of the free carrier absorption at each temperature is correlated with the decay of the 2464-cm^{-1} line. In the second experiment (Fig. 4.1.4(b)), H-treated samples

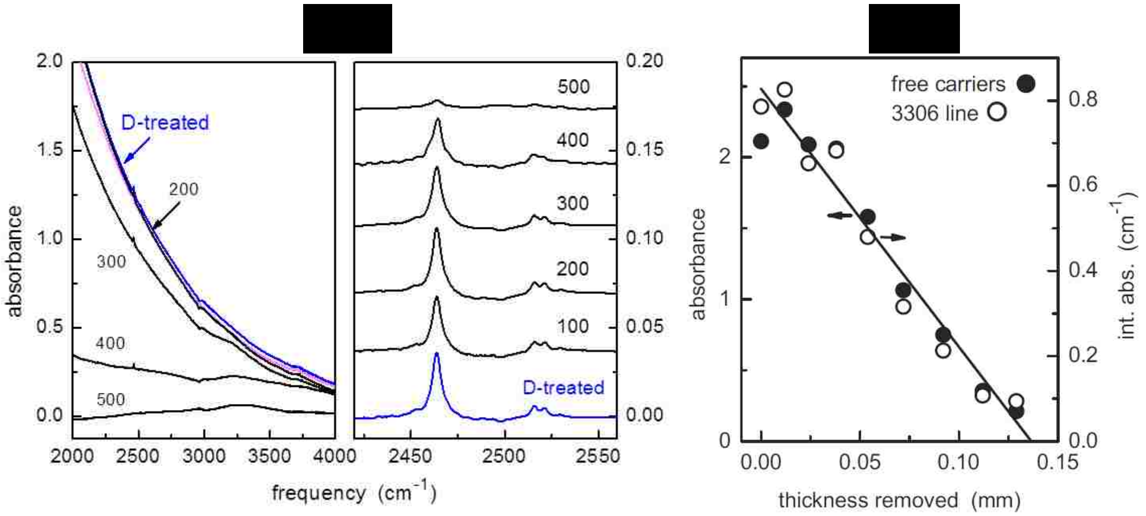

[redacted]

were thinned by lapping and polishing the sample. Both the free-carrier absorption and the O-H vibrational lines disappeared after ~0.15 mm of material was removed from the sample surfaces. The disappearance of the free-carrier absorption and the 3306 cm^{-1} O-H line show a similar dependence on the amount of sample removed, which suggests that the H center that gives rise to the 3306 cm^{-1} line is also responsible for the free-carrier absorption and therefore the conductivity of the sample.

Theoretical calculations have played a key role in identifying the microscopic structures of the O-H centers that give rise to the conductivity in In_2O_3. Limpijumnong and coworkers[2] investigated the formation energies of oxygen vacancies, substitutional hydrogen-, and interstitial hydrogen-defects in various charge states. The dependence of these formation energies on the Fermi energy is shown in Fig. 4.1.5(a).

[redacted] [redacted]

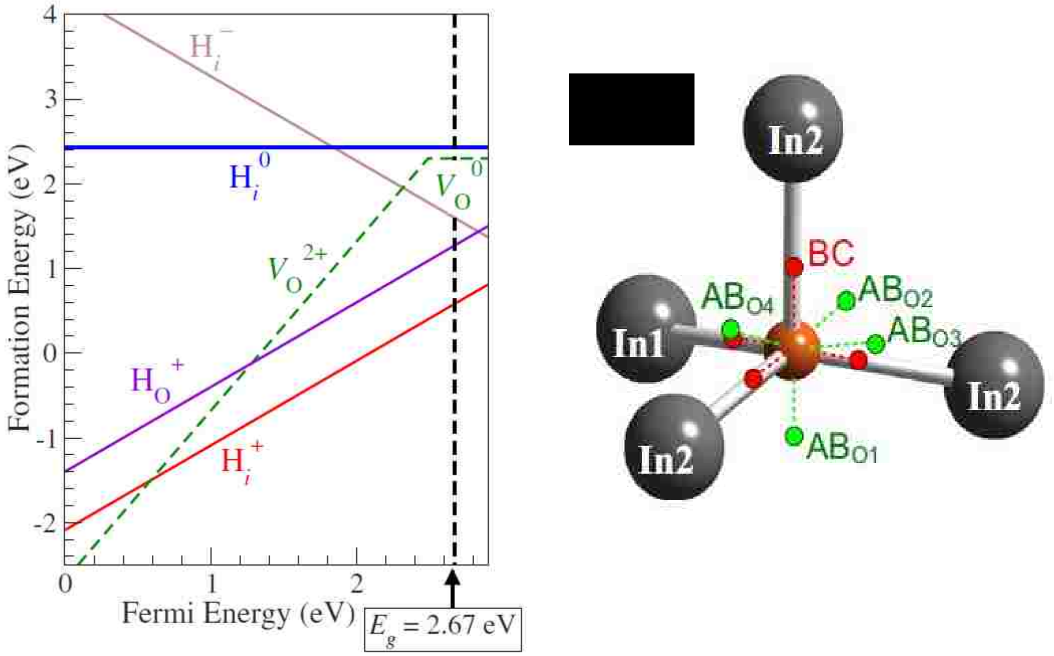

[redacted] (red) [redacted] (green) [redacted]

For all values of the Fermi energy, the positively charged interstitial-hydrogen defect (H_i^+) has the lowest formation energy and should therefore be the dominant shallow donor in this material. Figure 4.1.5(b) shows the different configurations that H_i^+ could occupy around an O atom. For the bond-centered (BC) configurations, which are shown in red, the hydrogen atoms lie along an In-O bond and are positioned between the In and O atoms. For the antibonding (AB) configurations, which are shown in green, the hydrogen atoms still lie along an In-O bond but are positioned on the side of the O atom opposite to the In atom. Although Limpijumnong *et al.*[2] found that the BC configurations of H_i^+ are unstable, there are several stable and metastable AB sites. The lowest energy configuration is labeled AB_{01}. The calculations reported by Yin *et al.*[7] confirmed these results, and they assigned the minimum energy H_i^+ site, shown in Fig. 4.1.6(a), to the 3306 cm^{-1} vibrational line.

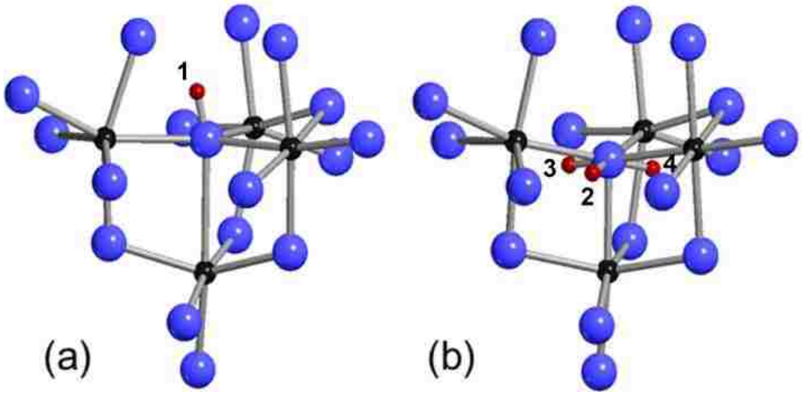

[redacted]

Infrared spectroscopy alone does not provide a definitive assignment of the 3306 cm^{-1} line to the ground-state H_i^+ structure. However, IR spectroscopy performed in conjunction with uniaxial stress yields information about the local symmetry of a defect based on the behavior of its vibrational lines under stress. This chapter presents the results of uniaxial stress experiments that determine the local structure and reorientation kinetics of O-H centers found in In_2O_3 single crystals.

4.2: Experimental Procedure

The In_2O_3 samples used in our experiments were bulk single crystals grown by the flux method at the Oak Ridge National Laboratory (ORNL) and whose properties have been reported recently.[8] Large single crystals, typically bigger than 5 x 5 x 2 mm^3, were used to fabricate samples for the application of uniaxial stress.

[redacted] [redacted]

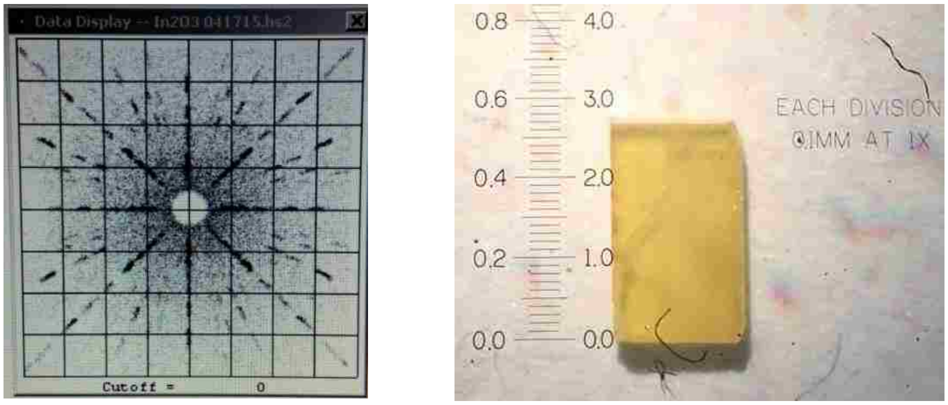

[redacted]

The Laue *x*-ray backscattering pattern for as-grown crystals (Fig. 4.2.1(a)) showed that these crystals had {100} faces, making it possible for us to prepare samples with either a [001] or [110] long axis for stress experiments. A typical [001]-oriented sample is shown in Fig. 4.2.1(b). The viewing axes for [001] and [110]-oriented stress samples were along the [100] and [001] directions, respectively.

The as-grown crystals already contained hydrogen and showed the 3306 cm^{-1} line assigned to H_i^+. This line could be made more intense by a 1 h anneal at 400°C in an inert ambient, presumably by the conversion of other hydrogen centers present in the as-grown sample. The OH centers present in the as-grown crystals were used in these experiments, i.e., the samples were not treated in a hydrogen atmosphere because centers distributed uniformly throughout the bulk of the In_2O_3 samples were preferred for our stress experiments.

Infrared absorption spectra were measured with a Bomem DA3.16 FTIR spectrometer equipped with a KBr beamsplitter and an InSb detector. Uniaxial stress was applied to a sample with a push-rod apparatus that was cooled in a variable-temperature Oxford CF 1204 cryostat using a He (4.2 K) or N_2 (77 K) cryogen. The probing light was polarized with a wire grid polarizer placed in the IR beam path between the sample and the detector. The empty sample holder with light polarized parallel or perpendicular to the stress axis was used to obtain reference spectra for all measurements.

Two different types of stress experiments were performed in these studies. In the first set of experiments, stress was applied to samples at 4.2 K or 77 K and the O-H centers were found to be static and unable to reorient among their possible configurations on the timescale of the IR measurements. In this case, the symmetries of the defects and their transition-moment directions could be determined.

In the second set of experiments, samples were cooled to low temperature (both 4.2 K and 77 K are sufficient) prior to the application of [001] or [110] stresses near 260 MPa and then annealed at successively higher temperatures to probe whether the O-H centers are able to reorient among their stress-split configurations. For the isochronal anneals, each sample received a series of anneals (15 minutes each) at successively higher temperatures with the stress maintained. For the isothermal anneals, each sample received a series of anneals at a constant temperature for successively longer lengths of time with the stress maintained. After each anneal, the sample was cooled under stress to low temperature for the measurement of polarized IR spectra. These experiments revealed information about the reorientation kinetics of the O-H centers.

4.3: Experimental Results: Symmetries

The experiments by Yin *et al.*[7] identified several O-H vibrational modes in H-treated In_2O_3 single crystals with frequencies of 3225, 3271, 3290, 3306, 3316, 3357, 3371, 3390, 3398, and 3411 cm^{-1}. The relative intensities of these lines vary from sample to sample. The crystals used for these uniaxial stress studies were treated to maximize the intensity of the 3306 cm^{-1} H_i^+ line. The lines at 3225, 3271, and 3290 cm^{-1} were not observed in the stressed samples. The intensity of the 3316 cm^{-1} line was correlated with the intensity of the 3398 cm^{-1} line, as seen in Fig 4.1.3; a strong 3398 cm^{-1} line resulted in a shoulder at 3316 cm^{-1}. As the 3398 cm^{-1} line is weak or absent in the absorbance spectra for our stress samples, the 3316 cm^{-1} line is assumed to be too weak to be observed. Our peak fitting showed that the 3306 cm^{-1} line seen in the unstressed sample could be fit with a symmetric, Gaussian (or Lorentzian) line shape. This point is important because a stress-induced shift of the 3316 cm^{-1} line will not interfere with our determination of the shift of the 3306 cm^{-1} line.

Two new, unresolved vibrational lines with frequencies at 4.2 K of approximately 3381 and 3404 cm^{-1} were detected in our absorbance spectra that have not been reported previously.

4.3.1: The 3306 cm^{-1} resonance due to the H_i^+ shallow donor

Figure 4.3.1 shows absorbance spectra for the 3306 cm^{-1} line of the H_i^+ shallow donor center with increasing magnitudes of stress applied along the [001] direction at 4.2 K and 77 K. The magnitude of the stress on the sample (in MPa) is shown at the baseline of each peak, and the dotted line indicates the peak position at zero stress. For small stress values (< 200 MPa), both polarizations showed a common red-shifted component and increasing asymmetry in the line shape for **E**||[010]. At larger stress values (250 – 270 MPa), this asymmetry had two unresolved components, one red-shifted and one blue-shifted, which are labeled as *b* and *a*, respectively. The *b* component was more intense than the *a* component. For **E**||[001], there appears to be a single broad line, but our analysis shows that component *a* is also present in this polarization with an intensity that is weaker compared to the **E**||[010] polarization. Samples which received stresses greater than 270 MPa consistently fractured and were no longer usable for stress experiments.

The shifts of the 3306 cm^{-1} line for increasing stresses along the [110] direction at 4.2 K and 77 K are shown in Fig. 4.3.2. For small stress values, both polarizations showed no apparent shift although for **E**||[110], the line becomes slightly asymmetric. For larger stress values, this asymmetry had two components, one red-shifted (*f*) and one blue-shifted (e_2), though they are less resolved than the spectra with **E**||[010] for [001] stress. The **E**||[1$\bar{1}$0] polarization still showed a single, unshifted component that broadens upon the application of stress.

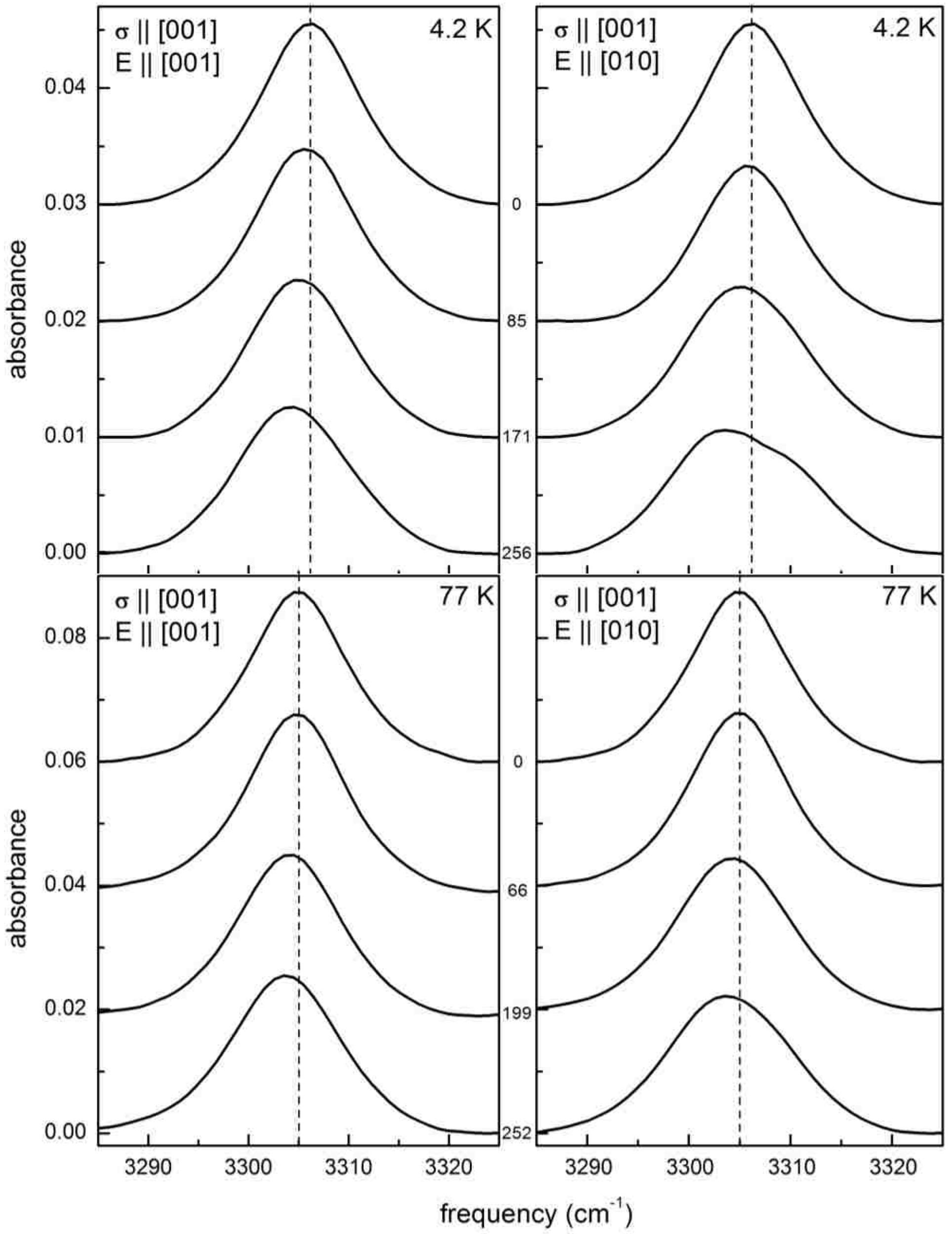
σ || [001]
E || [001]
4.2 K
σ || [001]
E || [010]
4.2 K
σ || [001]
E || [001]
77 K
σ || [001]
E || [010]
77 K
absorbance
0.04
0.03
0.02
0.01
0.00
0
85
171
256
absorbance
0.08
0.06
0.04
0.02
0.00
0
66
199
252
3290
3300
3310
3320
3290
3300
3310
3320
frequency (cm^{-1})

[redacted]

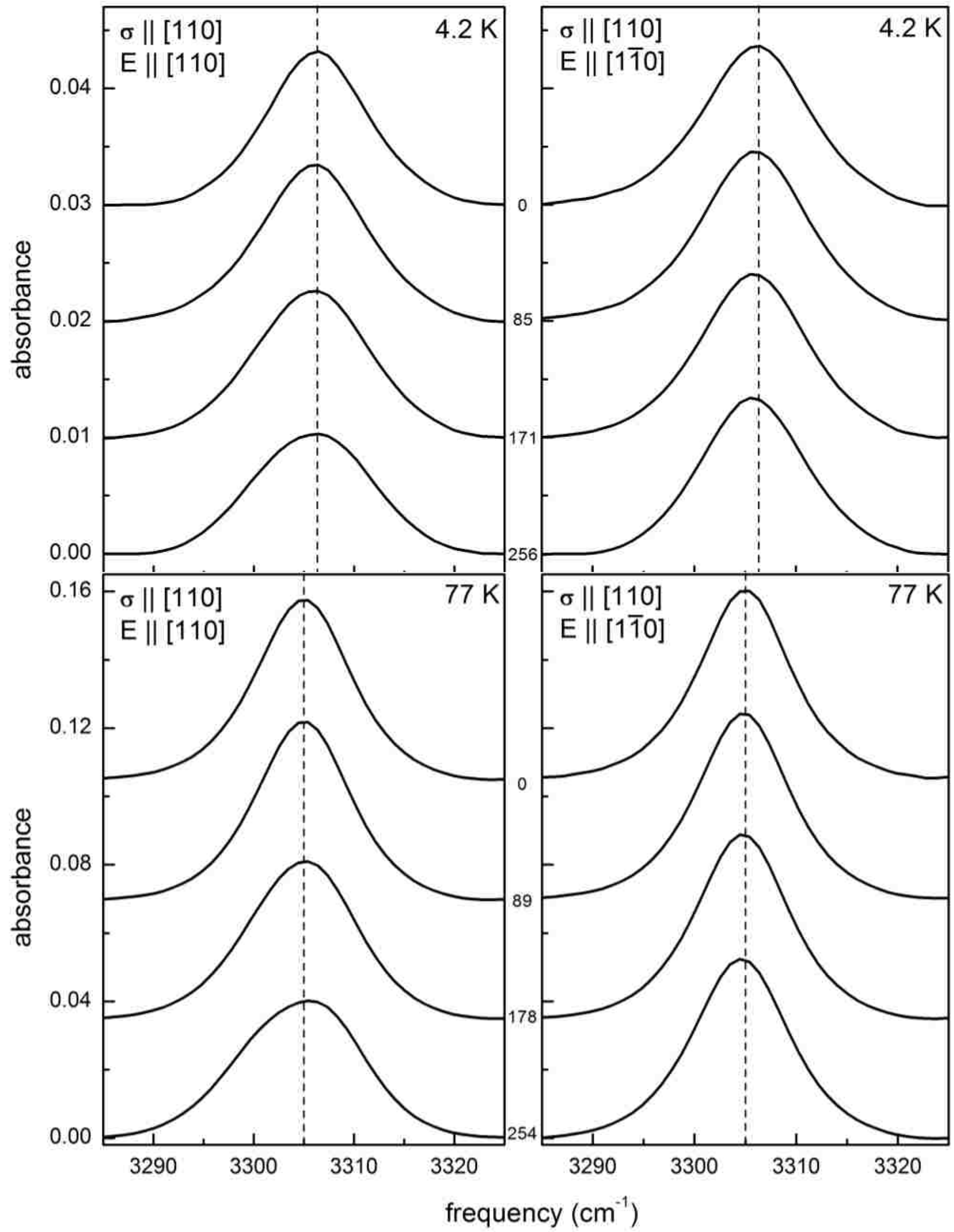
σ || [110]
E || [110]
4.2 K
σ || [110]
E || [1$\bar{1}$0]
4.2 K
0.04
0.03
0.02
0.01
0.00
absorbance
0
85
171
256
σ || [110]
E || [110]
77 K
σ || [110]
E || [1$\bar{1}$0]
77 K
0.16
0.12
0.08
0.04
0.00
absorbance
0
89
178
254
3290
3300
3310
3320
3290
3300
3310
3320
frequency (cm^{-1})

[redacted]

In the absence of stress, the 3306 cm^{-1} line had a FWHM of ~10 cm^{-1}, and the additional broadening introduced by stress makes it difficult to determine the split positions, widths, and relative intensities of the stress-split components in the absorption spectra accurately. One method to better identify and characterize line splittings is to examine the second derivative of the absorbance spectrum. A feature of the second-derivative spectrum is the narrowing of absorption lines, which allows unresolved peaks in the absorption spectrum to be separated in the second-derivative spectrum. Our second-derivative spectra were smoothed using the Savitsky-Golay routine in GRAMS/AI, which smooths the second-derivative calculated from point-to-point differences by convoluting it with a second-order polynomial. The number of points used in the smoothing routine was kept as small as possible to enhance the S/N ratio of the second-derivative spectrum without introducing additional line-width broadening. For all of our second-derivative spectra, the number of smoothing points was kept between 7 and 11. Figures 4.3.3 and 4.3.4 show the second derivatives of the polarized IR absorbance spectra for the In_2O_3 crystals under [001] and [110] stress, respectively, that were shown in Figs. 4.3.1 and 4.3.2. These second-derivative spectra determine the number of stress-split components and their relative intensities in each polarization.

For the O-H centers in In_2O_3, the second derivatives of the measured absorbance spectra have sufficiently high S/N ratios that fits can be made with the second derivatives of spectral line shapes. In our first stressed samples measured in the absence of stress, the 3306 cm^{-1} line is best fit with a Gaussian line shape given by Eq. (4.3.1).

$$G(\omega) = \frac{a_0}{a_{2\mathrm{G}}\sqrt{2\pi}} \exp\left[-\frac{1}{2}\left(\frac{\omega - a_1}{a_{2\mathrm{G}}}\right)^2\right] \qquad \textbf{Eq. (4.3.1)}$$

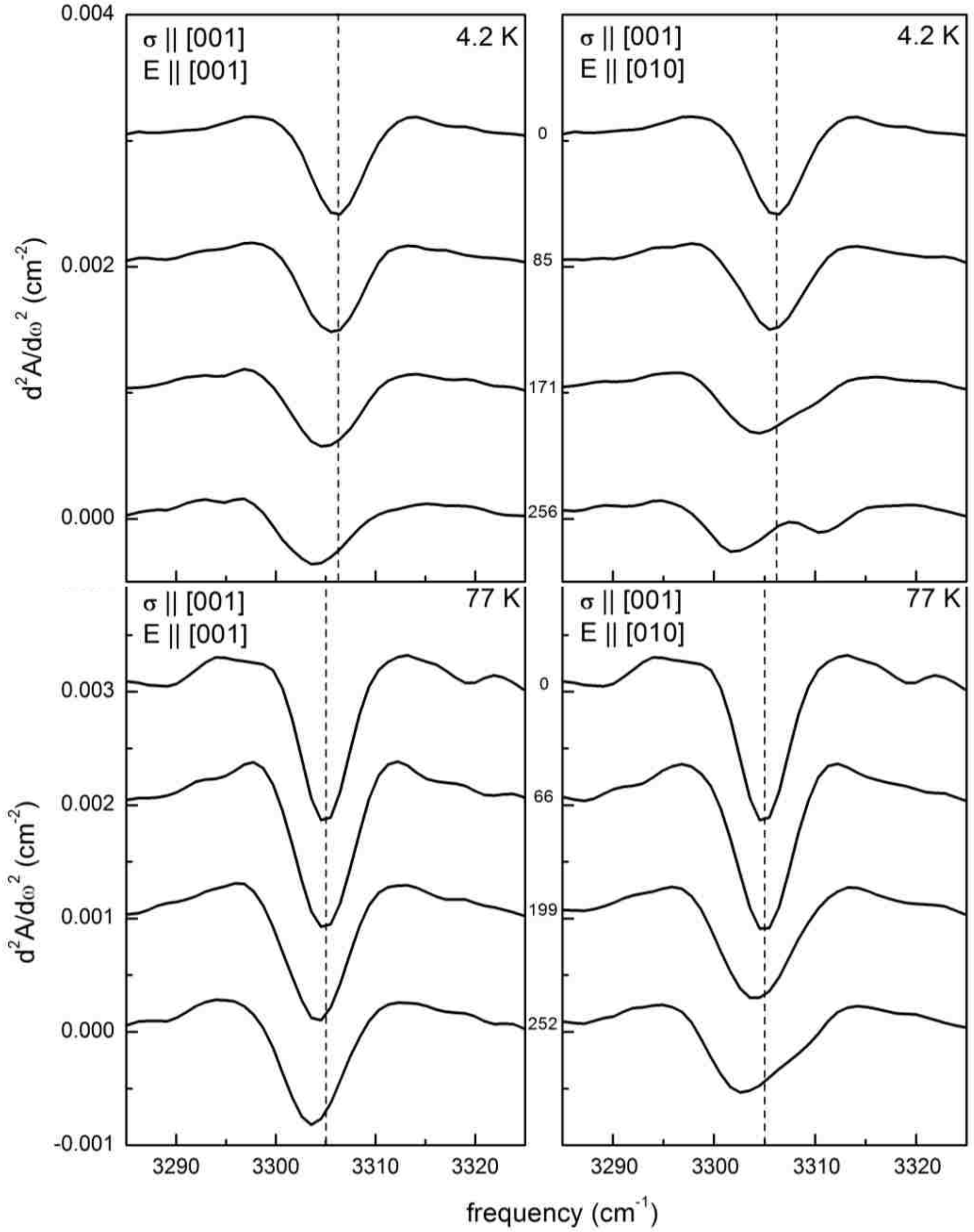
σ || [001]
E || [001]
4.2 K
σ || [001]
E || [010]
4.2 K
σ || [001]
E || [001]
77 K
σ || [001]
E || [010]
77 K
0
85
171
256
0
66
199
252
0.004
0.002
0.000
0.003
0.002
0.001
0.000
-0.001
$d^2A/d\omega^2$ (cm^{-2})
$d^2A/d\omega^2$ (cm^{-2})
3290
3300
3310
3320
3290
3300
3310
3320
frequency (cm^{-1})

[redacted]

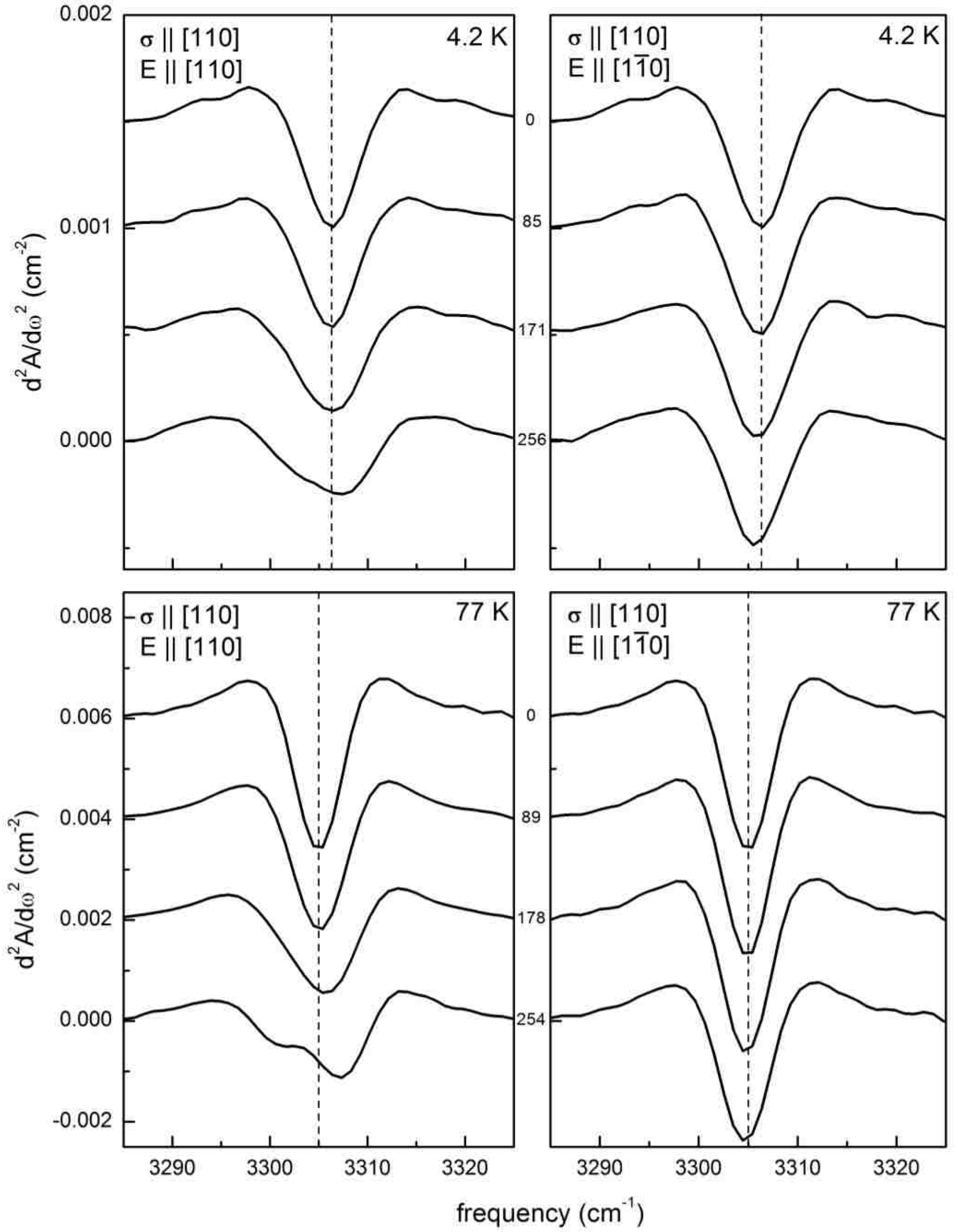
σ || [110]
E || [110]
4.2 K
σ || [110]
E || [1$\bar{1}$0]
4.2 K
0
85
171
256
0.002
0.001
0.000
d^{2}A/dω^2 (cm^{-2})
σ || [110]
E || [110]
77 K
σ || [110]
E || [1$\bar{1}$0]
77 K
0
89
178
254
0.008
0.006
0.004
0.002
0.000
-0.002
d^{2}A/dω^2 (cm^{-2})
3290
3300
3310
3320
3290
3300
3310
3320
frequency (cm^{-1})

[redacted]

In this expression, a_0 is the area or integrated absorbance, a_1 is the center frequency, and $a_{2\mathrm{G}}$ is the standard width of the peak. The second derivative of this line shape is given by Eq. (4.3.2),

$$\frac{d^2G}{d\omega^2} = \frac{1}{{a_{2\mathrm{G}}}^2}\left[\left(\frac{(\omega - a_1)}{a_{2\mathrm{G}}}\right)^2 - 1\right]G(\omega). \qquad \textbf{Eq. (4.3.2)}$$

The symmetry of the H_i^+ shallow donor and the direction of its transition moment can be determined from the number of stress-split components and their relative intensities. Kaplyanski[9] has tabulated the splittings and relative intensities for non-cubic defect centers in cubic crystals. The splittings of the 3306 cm^{-1} line, two components for [001] stress and at least three components for [110] stress, limit the defect symmetry to either rhombic I or monoclinic I; the type I centers having their primary axes along a [110] direction. A defect with rhombic symmetry must have its transition moment for an electric dipole transition oriented along the primary axis of the defect (Kaplyanski's π-oscillator), which fixes the relative intensities of the components seen for different polarizations. These tabulated intensities do not match the experimental data for stress along either the [001] or [110] directions. The two components seen in **E**||[010] would have the same intensity for rhombic I symmetry, but the data show that component *b* is stronger than component *a*. In addition, component e_2 seen for the **E**||[110] polarization should be present with the same intensity for the **E**||$[1\bar{1}0]$ polarization, which it is not. These discrepancies between the tabulated pattern and the experimental data eliminate the rhombic I symmetry, which means the defect must have monoclinic I symmetry and belongs to the C_{1h} point group.

A comparison of the experimental intensity ratios with those predicted for the π-oscillator with monoclinic I symmetry shows that they are still in disagreement. However, a monoclinic center can have its transition moment for an electric dipole transition at any angle θ in the reflection plane that is normal to the primary axis of the defect without any restriction imposed by symmetry on θ in this plane.[10] The angle θ is measured with respect to the <001> direction that is perpendicular to the <110> primary axis of the defect and is determined from the polarization-dependent intensities of the individual components. Davies and coworkers[10] have calculated the relative intensities of these stress-split components. The method for calculating the polarization-dependent intensity of a component is to sum the squares of the transition moments for a family of crystallographically equivalent defects projected onto the polarization directions of the measuring light (oriented parallel or perpendicular to the stress direction).

$$I_\alpha = \sum_i |\hat{\boldsymbol{\varepsilon}}_\alpha \cdot \hat{\boldsymbol{u}}_i|^2 \qquad \textbf{Eq. (4.3.3)}$$

Here $\hat{\boldsymbol{\varepsilon}}_\alpha$ is a unit vector in the polarization direction α that is either parallel or perpendicular to the stress axis and $\hat{\boldsymbol{u}}_i$ is a unit vector in the transition-moment direction. The twelve different orientations of a [110] monoclinic defect in a cubic crystal are shown in Fig. 4.3.5, and the transition moment-unit vectors are listed in Table 4.3.1. These orientations are equivalent under zero stress. Under [001] stress, component *a* has four equivalent orientations (*i*=1, 2, 3, 4) and component *b* has eight equivalent orientations (*i*=5, 6, …, 12).

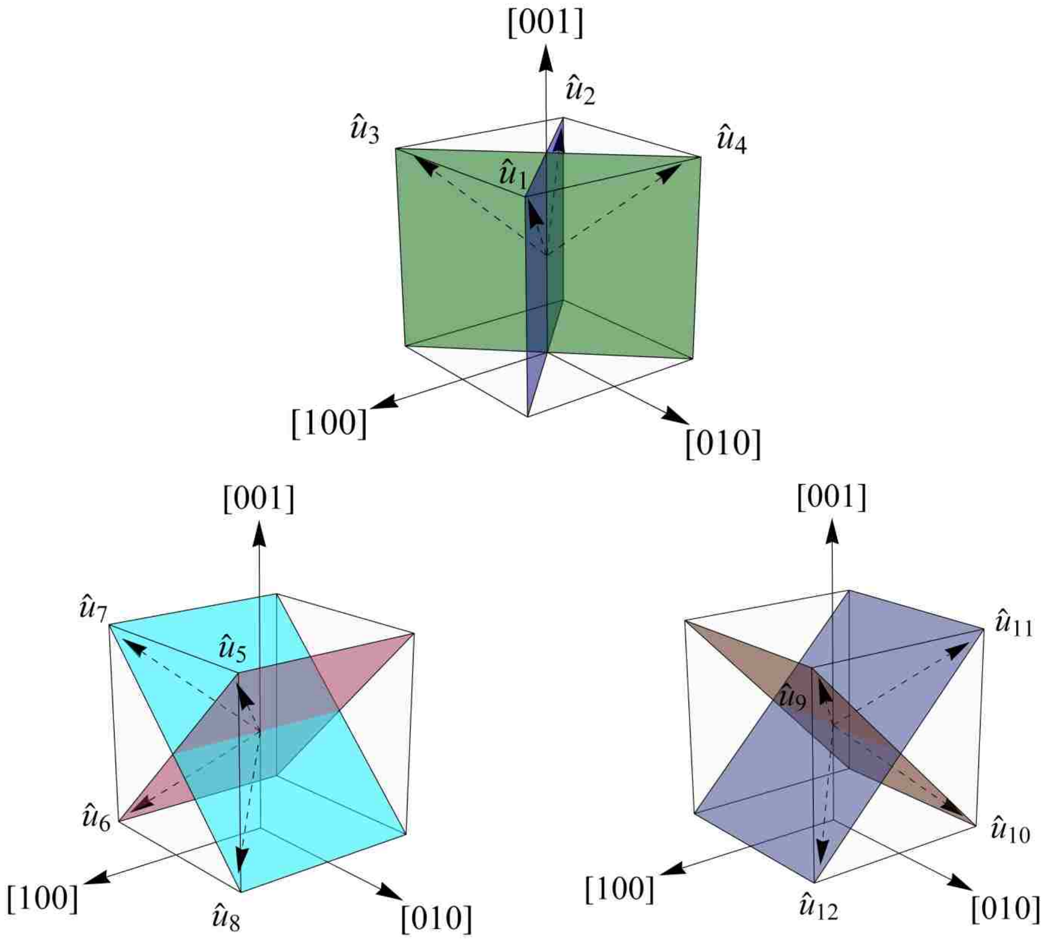

[redacted]

Under [110] stress, there are four components: components *f* and *g* each have two equivalent orientations, *i* = 1, 2 and i = 3,4, respectively. Component e_1 has four equivalent orientations (*i* = 6, 8, 10, and 12) and component e_2 also has four equivalent orientations (*i* = 5, 7, 9, and 11). The relative intensities of all components as a function of θ are given in Table 4.3.2 and are plotted in Fig. 4.3.6. The relative intensities of the *a* and e_2 components are derived here as examples. For component *a*, $\hat{\boldsymbol{\varepsilon}}_{001,||} = [001]$ and

$\hat{\boldsymbol{\varepsilon}}_{001,\perp} = [010]$. The relative intensities of *a* for light polarized parallel and perpendicular to the [001] axis are,

$$I_{a||} = \sum_{i=1}^{4} \left|\hat{\boldsymbol{\varepsilon}}_{001,\parallel} \cdot \hat{\boldsymbol{u}}_i\right|^2$$

$$= ([001] \cdot \hat{\boldsymbol{u}}_1)^2 + ([001] \cdot \hat{\boldsymbol{u}}_2)^2 + ([001] \cdot \hat{\boldsymbol{u}}_3)^2 + ([001] \cdot \hat{\boldsymbol{u}}_4)^2$$

$$= \cos^2\theta + \cos^2\theta + \cos^2\theta + \cos^2\theta = 4\cos^2\theta$$

and

$$I_{a\perp} = \sum_{i=1}^{4} \left|\hat{\boldsymbol{\varepsilon}}_{001,\perp} \cdot \hat{\boldsymbol{u}}_i\right|^2$$

$$= ([010] \cdot \hat{\boldsymbol{u}}_1)^2 + ([010] \cdot \hat{\boldsymbol{u}}_2)^2 + ([010] \cdot \hat{\boldsymbol{u}}_3)^2 + ([010] \cdot \hat{\boldsymbol{u}}_4)^2$$

$$= \frac{1}{2}\sin^2\theta + \frac{1}{2}\sin^2\theta + \frac{1}{2}\sin^2\theta + \frac{1}{2}\sin^2\theta = 2\sin^2\theta.$$

Table 4.3.1: Unit transition moment vector, $\hat{\boldsymbol{u}}_i$, of the *i*th position of a [110] monoclinic defect in a cubic crystal. There are twelve possible moments for the defect. The index *i* matches the labeling used by Nowick and Berry[11] in their discussion of the anelastic relaxation of [110] monoclinic defects under uniaxial stress in a cubic crystal.

$\hat{\boldsymbol{u}}_1 = \cos\theta\,(001) + \sin\theta\frac{1}{\sqrt{2}}(110)$	$\hat{\boldsymbol{u}}_2 = \cos\theta\,(001) - \sin\theta\frac{1}{\sqrt{2}}(110)$
$\hat{\boldsymbol{u}}_3 = \cos\theta\,(001) + \sin\theta\frac{1}{\sqrt{2}}(1\bar{1}0)$	$\hat{\boldsymbol{u}}_4 = \cos\theta\,(001) - \sin\theta\frac{1}{\sqrt{2}}(1\bar{1}0)$
$\hat{\boldsymbol{u}}_5 = \cos\theta\,(100) + \sin\theta\frac{1}{\sqrt{2}}(011)$	$\hat{\boldsymbol{u}}_6 = \cos\theta\,(100) - \sin\theta\frac{1}{\sqrt{2}}(011)$
$\hat{\boldsymbol{u}}_7 = \cos\theta\,(100) + \sin\theta\frac{1}{\sqrt{2}}(01\bar{1})$	$\hat{\boldsymbol{u}}_8 = \cos\theta\,(100) - \sin\theta\frac{1}{\sqrt{2}}(01\bar{1})$
$\hat{\boldsymbol{u}}_9 = \cos\theta\,(010) + \sin\theta\frac{1}{\sqrt{2}}(101)$	$\hat{\boldsymbol{u}}_{10} = \cos\theta\,(010) - \sin\theta\frac{1}{\sqrt{2}}(101)$
$\hat{\boldsymbol{u}}_{11} = \cos\theta\,(010) - \sin\theta\frac{1}{\sqrt{2}}(\bar{1}01)$	$\hat{\boldsymbol{u}}_{12} = \cos\theta\,(010) + \sin\theta\frac{1}{\sqrt{2}}(\bar{1}01)$

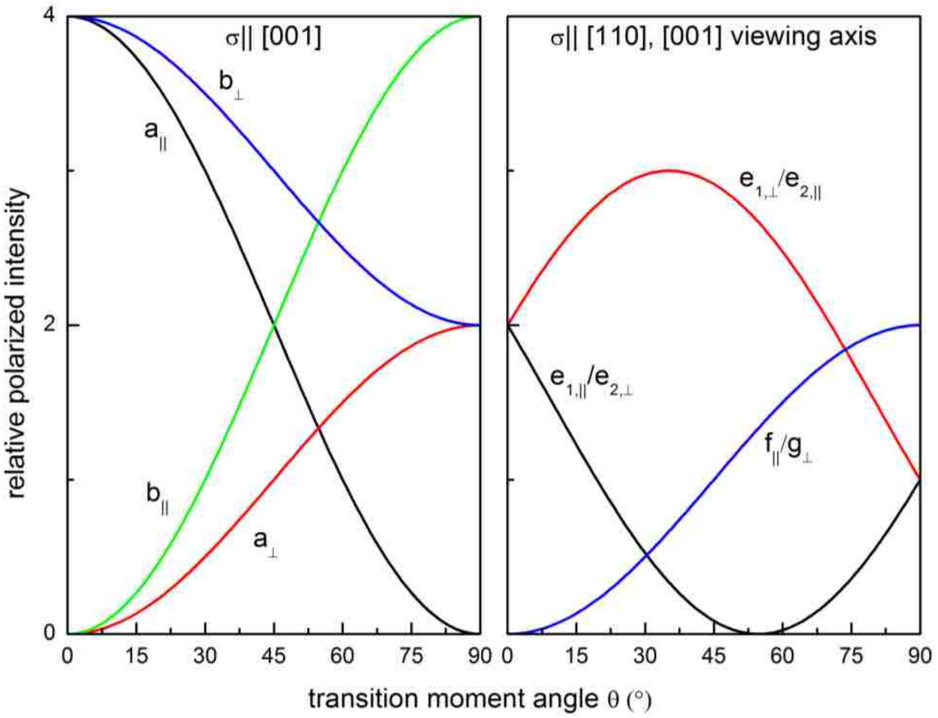

[redacted]

For component e_1, $\hat{\boldsymbol{\varepsilon}}_{110,||} = \frac{1}{\sqrt{2}}[110]$ and $\hat{\boldsymbol{\varepsilon}}_{110,\perp} = \frac{1}{\sqrt{2}}[1\bar{1}0]$, and the relative intensities for light polarized parallel and perpendicular to the [110] stress axis are,

$$I_{e_2,||} = \sum_{i=5,7,9,11} \left|\hat{\boldsymbol{\varepsilon}}_{110,\|} \cdot \hat{\boldsymbol{u}}_i\right|^2$$

$$= \frac{1}{\sqrt{2}}\{([110] \cdot \hat{\boldsymbol{u}}_5)^2 + ([110] \cdot \hat{\boldsymbol{u}}_7)^2 + ([110] \cdot \hat{\boldsymbol{u}}_9)^2 + ([110] \cdot \hat{\boldsymbol{u}}_{11})^2\}$$

$$= 4\left\{\frac{\cos\theta}{\sqrt{2}} + \frac{1}{2}\sin\theta\right\}^2 = \left(\sqrt{2}\cos\theta + \sin\theta\right)^2$$

and

$$I_{e_2,\perp} = \sum_{i=5,7,9,11} \left|\hat{\boldsymbol{\varepsilon}}_{110,\perp} \cdot \hat{\boldsymbol{u}}_i\right|^2$$

$$= \frac{1}{\sqrt{2}}\{([1\bar{1}0] \cdot \hat{\boldsymbol{u}}_5)^2 + ([1\bar{1}0] \cdot \hat{\boldsymbol{u}}_7)^2 + ([1\bar{1}0] \cdot \hat{\boldsymbol{u}}_9)^2 + ([1\bar{1}0] \cdot \hat{\boldsymbol{u}}_{11})^2\}$$

$$= 4\left(\frac{\cos\theta}{\sqrt{2}} - \frac{\sin\theta}{2}\right)^2 = \left(\sqrt{2}\cos\theta - \sin\theta\right)^2.$$

Table 4.3.2: Uniaxial stress perturbations for a [110] monoclinic defect in a cubic crystal for the [001] and [110] stress directions, with viewing directions along [100] and [001], respectively. The column on the right hand side gives the theoretical results for the relative intensities of the stress-split components for a specific angle of the transition moment, θ. Reprinted from P. Weiser, *et al.* Applied Physics Letters **109**, 202105 (2016), with permission of AIP Publishing. http://dx.doi.org/10.1063/1.4967943.

stress	**component**	**shift rate**	**E**//001	:	**E**//010
[001]	a	A_1	$4(\cos^2\theta)$	:	$2(\sin^2\theta)$
	b	A_2	$4(\sin^2\theta)$	:	$2(\cos^2\theta+1)$
			E//110	:	**E**//$1\bar{1}0$
[110]	e_1	$(A_1 + A_2)/2 - A_4$	$(2^{1/2}\cos\theta-\sin\theta)^2$	:	$(2^{1/2}\cos\theta+\sin\theta)^2$
	e_2	$(A_1 + A_2)/2 + A_4$	$(2^{1/2}\cos\theta+\sin\theta)^2$	:	$(2^{1/2}\cos\theta-\sin\theta)^2$
	f	$A_2 - A_3$	$2(\sin^2\theta)$	:	0
	g	$A_2 + A_3$	0	:	$2(\sin^2\theta)$

The angle of the transition moment, θ, can be determined from the relative intensities of the stress-split components. Data for cases in which the stress-split components are clearly resolved, i.e., *b* and *a* for [001]-oriented samples, and e_2 and *f* for [110]-oriented samples, were used in this analysis. Using Table 4.3.1, the expressions used to determine θ are

$$\frac{I(b_\perp)}{I(a_\perp)} = \frac{\cos^2\theta + 1}{\sin^2\theta} \quad \text{and} \quad \frac{I(e_2)}{I(f)} = \frac{\left(\sqrt{2}\cos\theta + \sin\theta\right)^2}{\sin^2\theta}.$$

Table 4.3.3 shows the experimental ratios for larger stress values and the calculated value of θ from the fits. The average O-H bond angle θ is 62±13°.

Table 4.3.3: Ratios of [001] and [110] stress-split components at large values of stress (> 250 MPa) determined from the fits to the second derivatives of the measured IR absorbance spectra. The transition moment angle, θ, was calculated using the ratios of the relative intensities given in Table 4.3.2.

Components	**Date/Temp (K)**	**Stress (MPa)**	**Ratio**	**θ (°)**
$(b/a)_\perp$	2016-02-29/77	260	1.632	60.7
	2016-05-12/77	265	1.833	57.2
	2016-05-19/77	265	2.107	53.3
	2016-05-24/77	265	2.191	52.3
	2016-06-09/6.0	256	1.895	56.2
	2016-06-10/6.0	270	1.504	63.3
e_2/f	2014-12-24/77	255	1.510	80.8
	2016-05-26/77	267	1.656	78.5
	2016-05-31/77	267	1.637	78.8
	2016-06-08/6.0	264	1.279	84.7

This average angle was used to generate global fits to the polarized IR absorbance spectra and their second derivatives, which are shown in Figs. 4.3.7 and 4.3.8 for 4.2 K and 77 K, respectively. The second derivative of the measured spectrum (unfilled circles) and its fit (solid red curve) are shown at the top of each panel. The solid spectrum in the middle is the experimentally measured absorbance. The individual peaks (black) are shown below the fit spectrum (red) at the bottom of the panel. The global fits are in reasonable agreement with the experimental data.

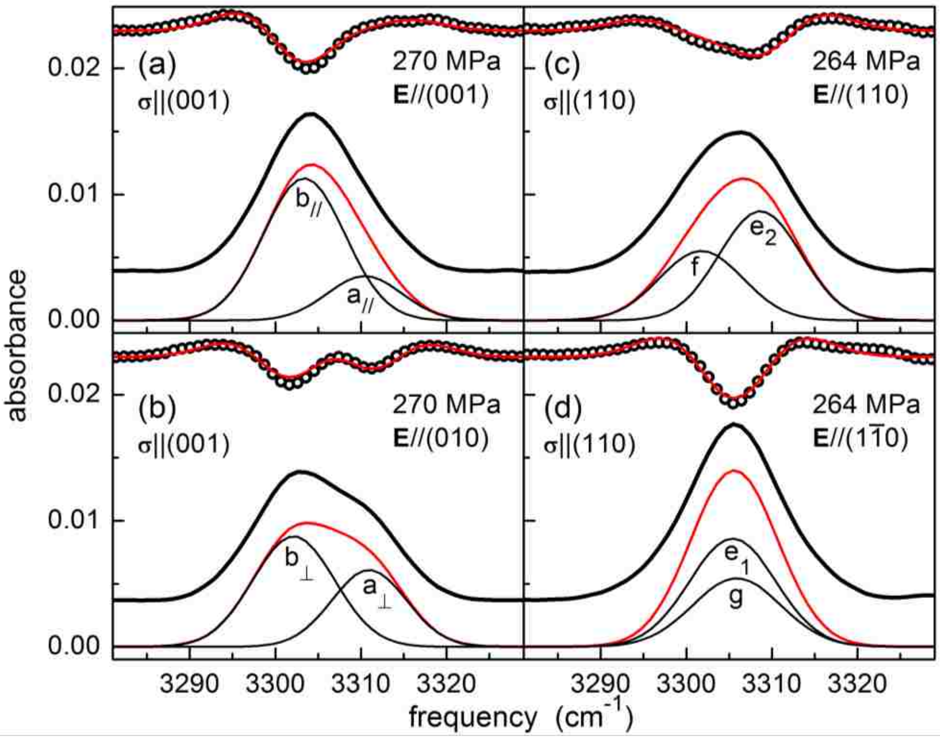
absorbance
0.00
0.01
0.02
(a)
σ||(001)
270 MPa
E//(001)
b//
a//
(c)
σ||(110)
264 MPa
E//(110)
f
e2
(b)
σ||(001)
270 MPa
E//(010)
b⊥
a⊥
(d)
σ||(110)
264 MPa
E//(1$\bar{1}$0)
e1
g
3290
3300
3310
3320
frequency (cm-1)

[redacted]

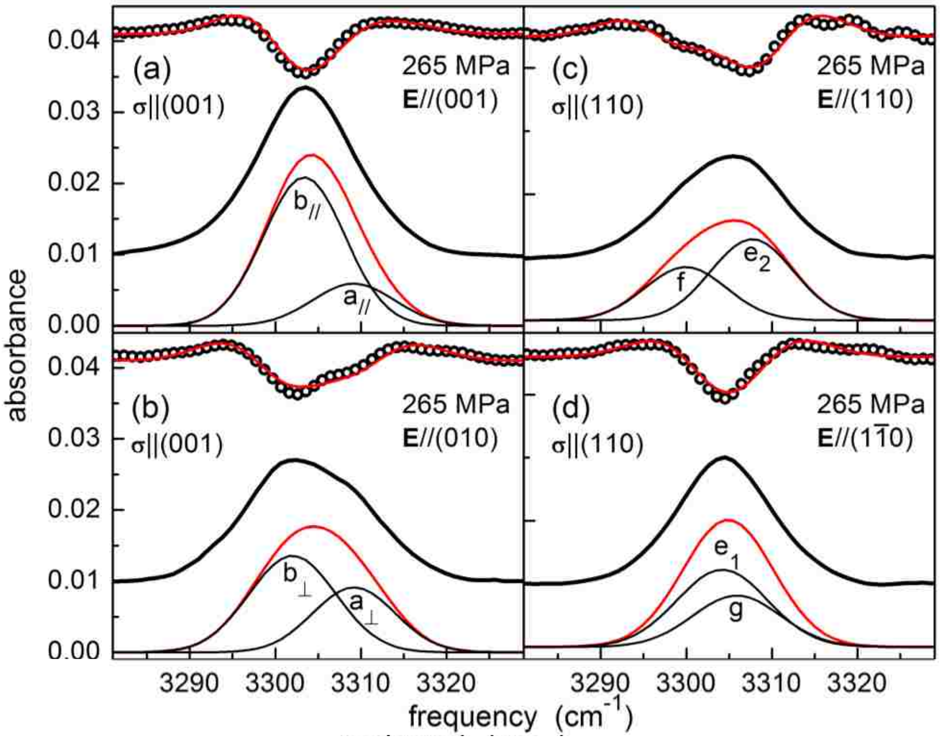

[redacted]

The LVM frequencies of the stress-split vibrational lines for a defect are typically a linear function of the applied stress. The slope of the plot of the LVM frequency shift for a defect, Δω, per unit applied stress is defined as the shift rate (cm^{-1}/GPa). For a [110] monoclinic defect, the shift rates for the stress-split components, which are listed in Table 4.3.2, are characterized by four independent shift rates: A_1, A_2, A_3, and A_4. A least-squares fit was performed using the Solver feature in Microsoft Excel to fit the shift rates to both the [001] and [110] stress data. Figure 4.3.9 shows the stress-induced shifts of each component and the corresponding fits at 4.2 K and 77 K. The calculated shift rates, which are listed in Table 4.3.4, confirm that the splitting of the e_1 and g components cannot be detected experimentally because these overlapping lines have similar shift rates.

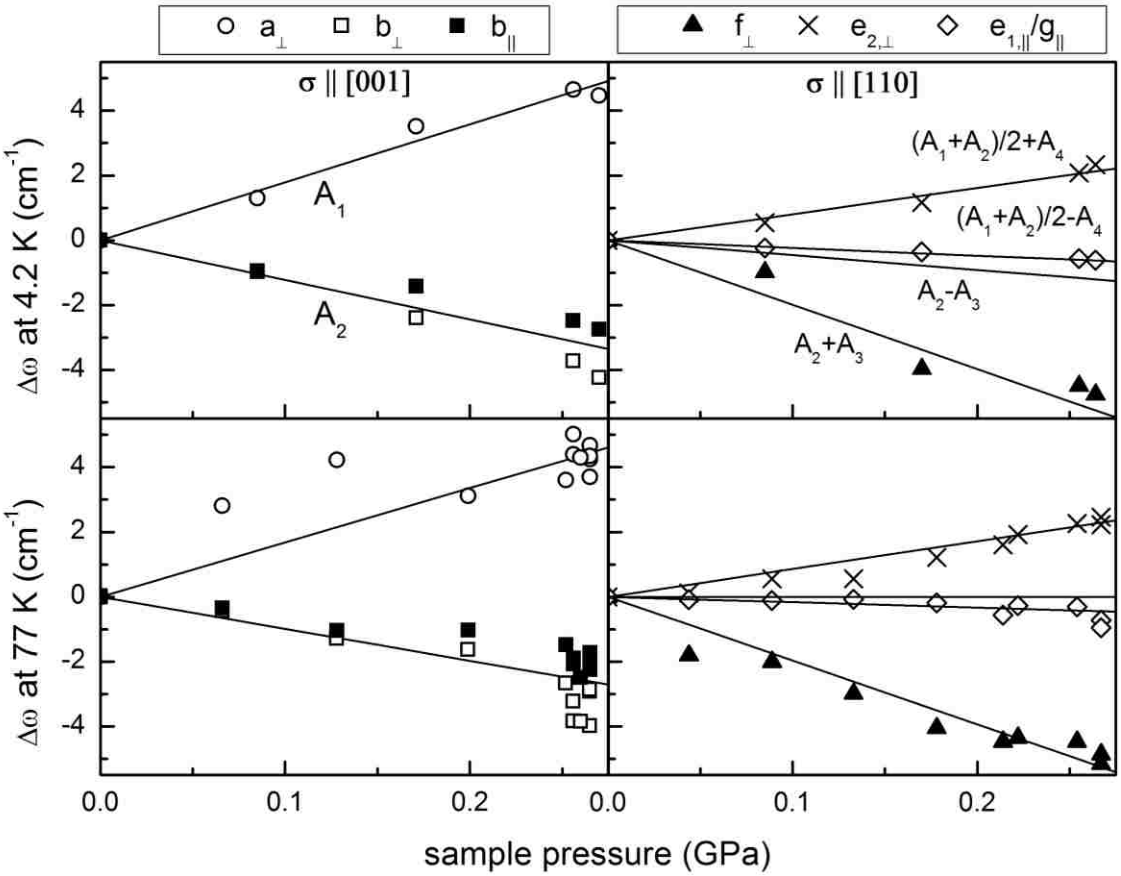

[redacted]

Table 4.3.4: Shift rates of the 3306 cm^{-1} H_i^+ center that are shown in Fig. 4.3.6. The shift rates A_1, A_2, A_3, and A_4 were determined at a fixed temperature (either 4.2 or 77 K) from a simultaneous fit to the [001] and [110] data using the Solver Add-In feature in Microsoft Office Excel.

Shift Rate (cm^{-1}/GPa)	**T = 77 K**	**T = 4.2 K**	**All data**
A_1	16.8	17.9	17.0 ± 1.0
A_2	-9.9	-12.2	-10.4 ± 1.0
A_3	9.8	7.7	9.3 ± 1.0
A_4	5.1	5.2	5.2 ± 1.0

In summary, the number of stress-split components, their relative intensities, and their shift rates show that the H_i^+ defect has C_{1h} symmetry and that its transition moment is at an angle of 62±13° with respect to the [001] axis. The [111] direction has an angle of 54.7° with respect to the [001] axis, so the O-H bonding direction for the 3306 cm^{-1} center is at an angle ~7° greater than the value for a <111> direction, which is in agreement with the “quasi-trigonal” symmetry predicted by theory.

4.3.2: Other OH centers

Figure 4.3.10 shows the O-H vibrational lines seen at higher frequencies in the IR-absorbance spectrum of an unstressed [001]-oriented sample. This spectrum could be fit by seven lines, five of which were identified previously by Yin *et al.*[7] as O-H vibrational modes. The two new lines, with frequencies of approximately 3381 and 3404 cm^{-1} (at 4.2 K), are unresolved from their neighboring lines, but their presence is suggested by the changes in curvature in the absorbance spectrum and further supported by their appearance in the second derivative spectrum. The stress-induced shifts of the vibrational lines are most easily seen in the second derivatives of the polarized IR absorbance spectra, which are shown in Fig. 4.3.11.

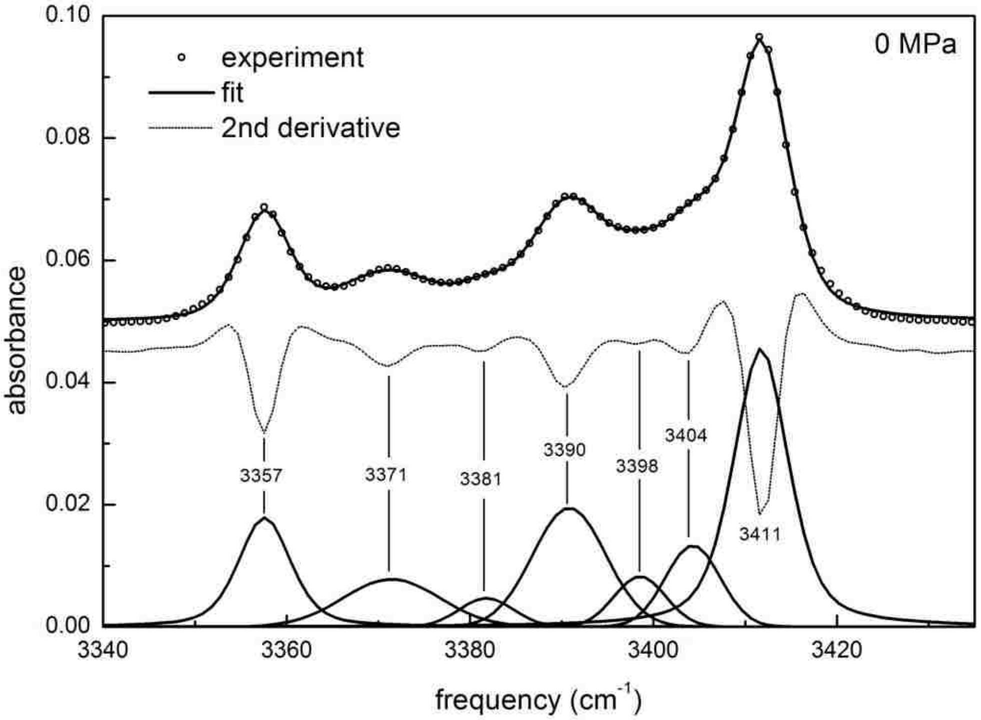

[redacted]

The identification of line splittings requires a shift in the LVM frequency that is not masked by the broad line-width. Only the 3357, 3371, and 3390 cm^{-1} O-H vibrational bands meet this condition. The shifts or splittings of the remaining lines cannot be reliably determined because of either the weak intensity of a line (3398 cm^{-1}) or because of a significant broadening of the line by stress (3411 cm^{-1}).

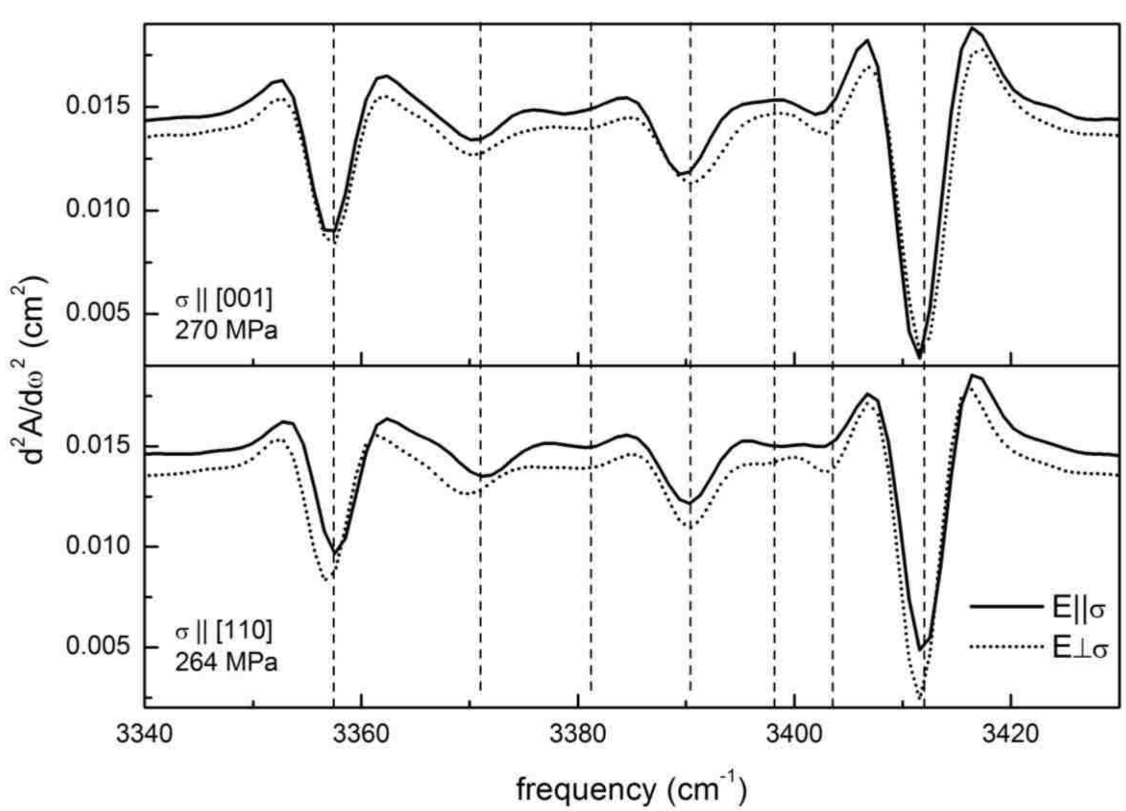

[redacted]

The stress-induced frequency shifts of the 3357, 3371, and 3390 cm^{-1} vibrational lines and the fits to the shift rates at 4.2 and 77 K are plotted in Figs. 4.3.12, 4.3.13, and 4.3.14. The shift rates are summarized in Table 4.3.5. The data at both temperatures showed the same trends. Under [001] stress, both the 3357 and 3371 cm^{-1} lines did not split and are slightly red-shifted for both polarizations. The lines split under [110] stress into two components, one with **E**∥[110] and the other with **E**∥$[1\bar{1}0]$. This splitting pattern suggests that these defects have trigonal symmetry and are π-dipole oscillators oriented parallel to a [110] direction.

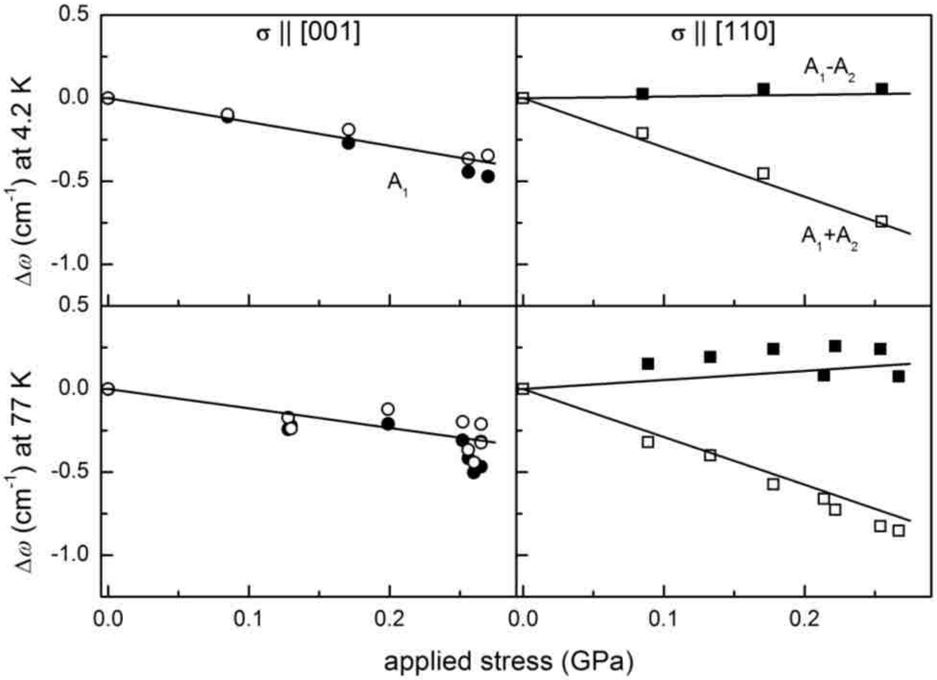

[redacted]

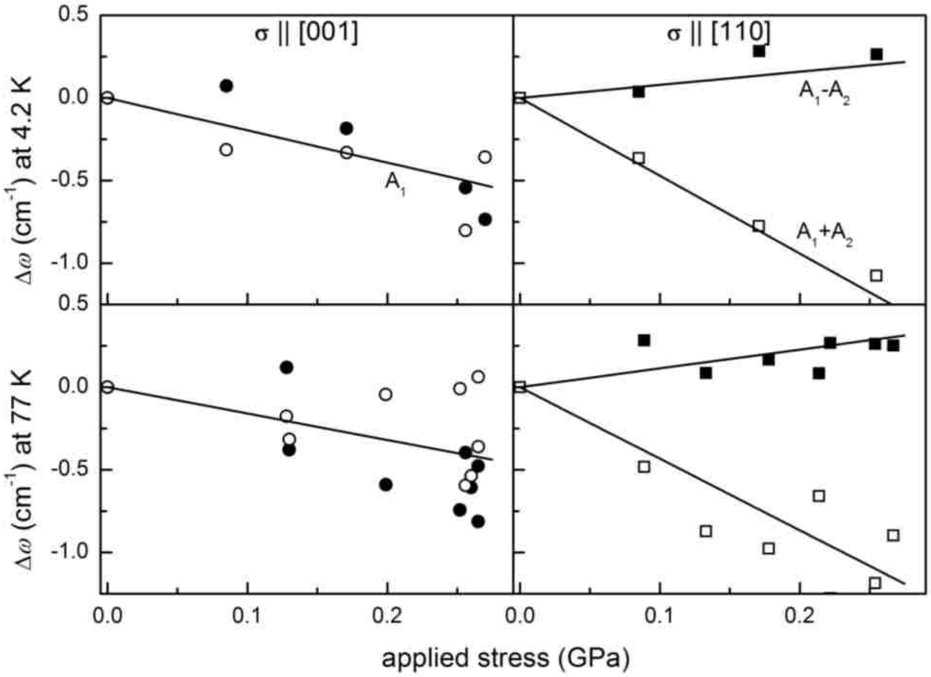
σ || [001]
σ || [110]
A$_1$
A$_1$-A$_2$
A$_1$+A$_2$
Δω (cm^{-1}) at 4.2 K
Δω (cm^{-1}) at 77 K
0.5
0.0
-0.5
-1.0
0.0
0.1
0.2
applied stress (GPa)

[redacted]

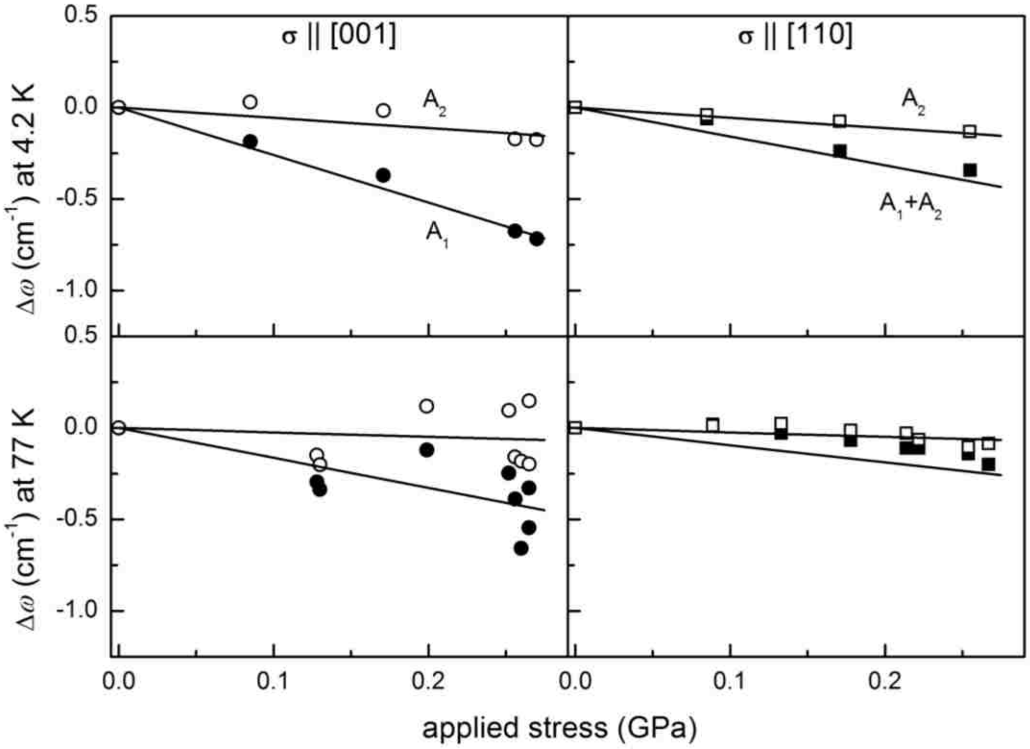

[redacted]

The 3390 cm^{-1} line splits into two components under [001] stress, which suggests a defect with tetragonal, rhombic I, or monoclinic I symmetry. However, the symmetry of this defect cannot be determined because the splitting under [110] stress is small. For any of the suggested symmetries, the $\mathbf{E}\|[1\bar{1}0]$ component should shift according to $(A_1+A_2)/2$, but seems to follow A_2 instead. Given that the experimental shift rates for the 3390 cm^{-1} line are small (~ 2 cm^{-1} or less), it is within experimental error that the $\mathbf{E}\|[1\bar{1}0]$

component shifts like $(A_1+A_2)/2$. The highest possible symmetry for this defect would be tetragonal, followed by rhombic I and monoclinic I symmetries.

Table 4.3.5: Shift rates of the 3357, 3371, and 3390 cm^{-1} OH lines which are shown in Fig. 4.3.9. The shift rates for a specific defect were determined at a fixed temperature (either 4.2 or 77 K) from a simultaneous fit to the [001] and [110] data using the Solver feature in Microsoft Office Excel.

LVM frequency (cm^{-1})	Shift Rate (cm^{-1}/GPa)	T = 77 K	T = 4.2 K
3357	A_1	-1.2	-1.4
3357	A_2	-1.7	-1.5
3371	A_1	-1.6	-2.0
3371	A_2	-2.7	-2.8
3390	A_1	-1.6	-2.6
3390	A_2	-0.2	-0.6

In summary, only the 3357, 3371 and 3390 cm^{-1} lines showed small splittings for [001] and [110] uniaxial stresses. The defects giving rise to the 3357 and 3371 cm^{-1} showed shifts consistent with trigonal symmetry. The 3390 cm^{-1} vibrational line showed shifts consistent with tetragonal, rhombic I, or monoclinic I symmetry.

4.4: Diffusion of H_i^+ in In_2O_3

4.4.1: Experimental Results: [001]-Stress-Induced-Alignment

When the stress was applied at elevated temperatures, the relative intensities of the stress-split components of the 3306 cm^{-1} line changed due to a stress-induced alignment of the inequivalent components of the C_{1h} center. The alignment indicates that the differently oriented configurations of the H_i^+ center have different ground-state energies under stress. These components would then be populated according to their Boltzmann factors if sufficient time elapses for equilibrium to be established. The greatest alignment is seen for stress along the [001] direction. This section focuses on those results; similar experiments performed for the [110] stress direction resulted in no appreciable stress-induced alignment from the component of stress along the [111] direction from 10 K to 300 K, consistent with it being the component of stress along the [001] directions that produced alignment. No stress-induced alignment was detected for any of the higher frequency OH vibrational lines for either the [001] or [110] stressed samples.

Our first experiments to produce a stress-induced alignment of the 3306 cm^{-1} H_i^+ center utilized isochronal anneals of 15 minutes. Figures 4.4.1 and 4.4.2 show the second derivatives of the measured absorbance spectra for **E**||[010] for two different [001]-oriented In_2O_3 samples measured at 6 and 77 K, respectively. The black curve is the spectrum taken after application of the [001] stress at 6 or 77 K. The red curves are from samples that were annealed under stress at the successively higher temperatures listed at the top of the panels and then cooled back down to 6 or 77 K for absorption measurements. Anneals at or below 150 K did not produce a substantial change in the intensity of either component. Anneals at 160 K consistently produced small changes in which the decrease in the intensity of *a* was accompanied by an increase in the intensity of *b*. The 175 K anneal enhanced these changes in intensity, and the effect saturated for anneals at temperatures greater than or equal to 180 K.

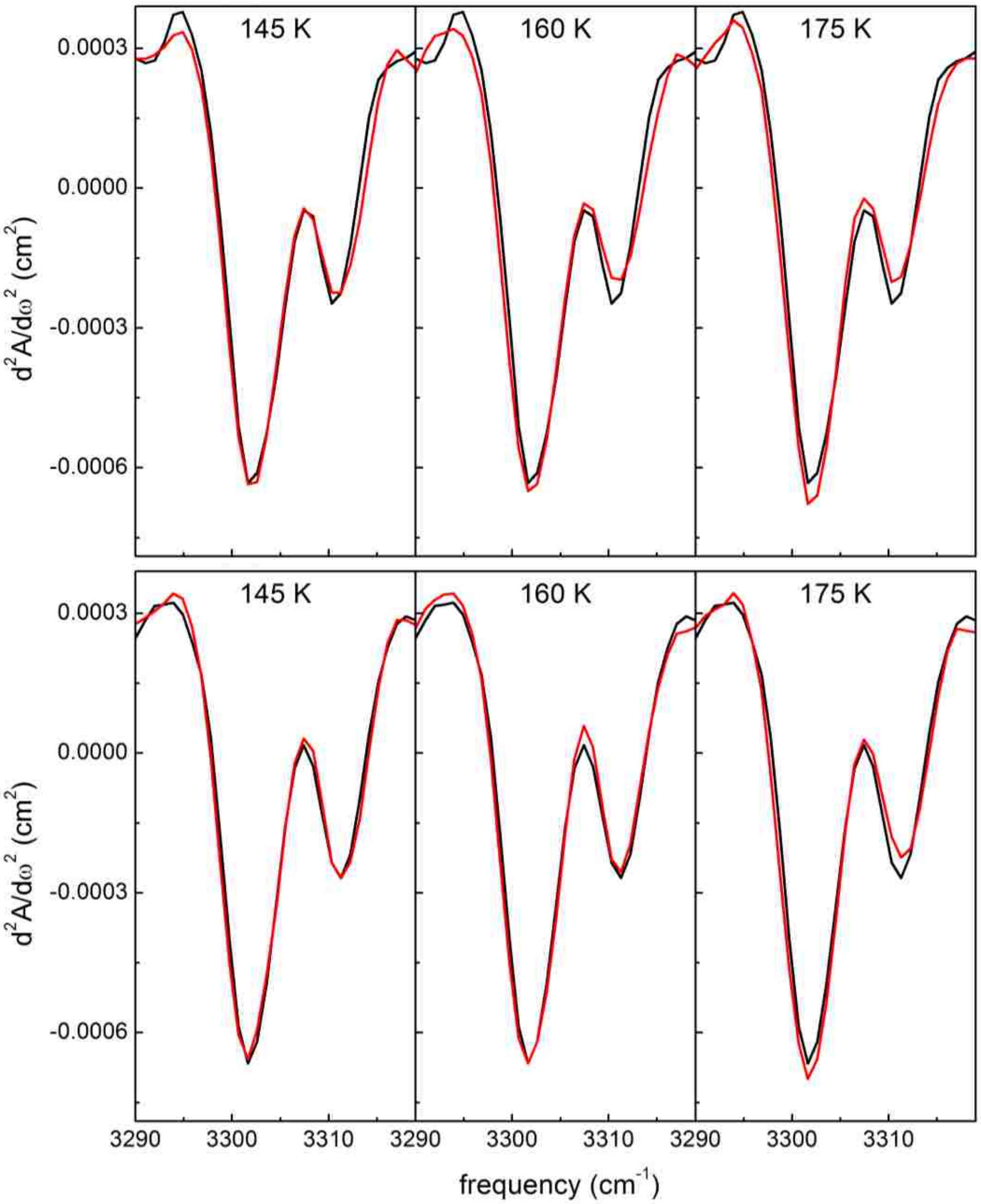
145 K
160 K
175 K
145 K
160 K
175 K
0.0003
0.0000
-0.0003
-0.0006
$d^2A/d\omega^2$ (cm^2)
3290
3300
3310
frequency (cm^{-1})

[redacted]

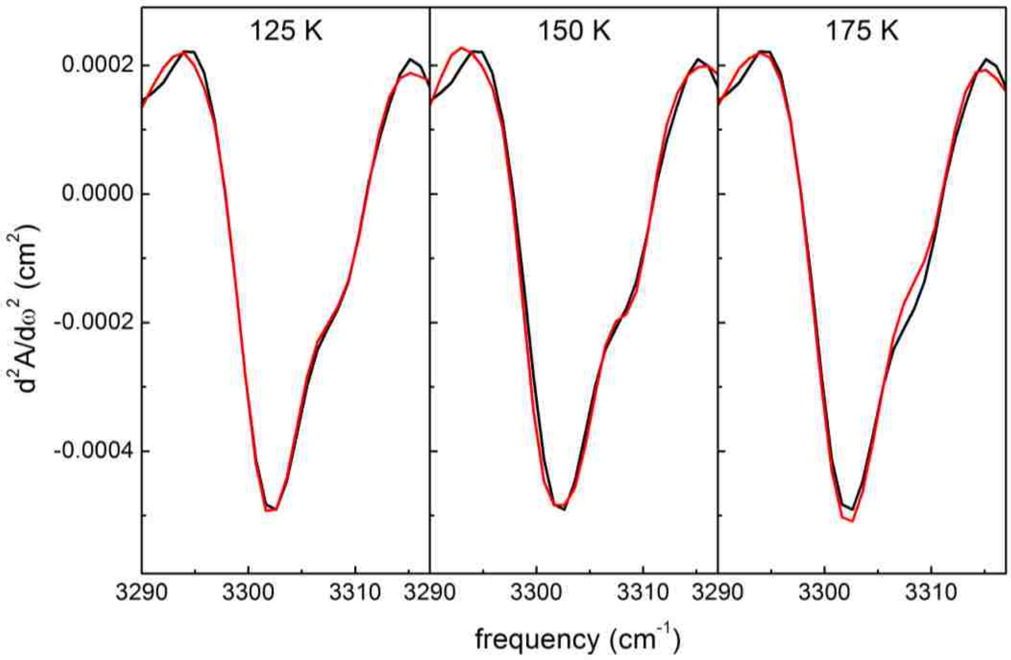

[redacted]

Isothermal-annealing experiments were also performed at temperatures between 153 and 160 K. Figure 4.4.3 shows the second derivatives of the absorbance spectra for the isothermal anneal at 160 K for 0 and 180 minutes. When the sample is annealed under stress for 20 or 40 minutes, the intensity of component *a* decreaseed slightly. Anneals for 60 minutes or longer increased the intensity of component *b* and decreased the intensity of component *a*, which is consistent with the trend seen for the isochronal anneals.

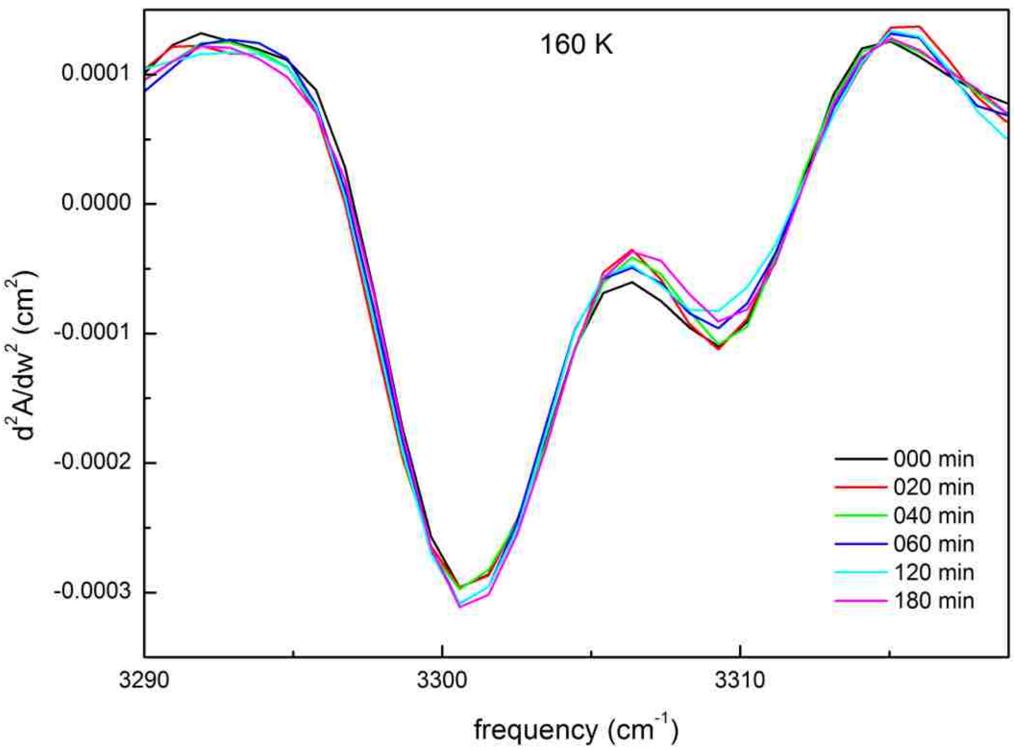

[redacted]

The stress-split lines for the isothermal annealing experiments were better resolved than the stress-split lines in the isochronal annealing experiments. Figures 4.4.4 and 4.4.5 show the second derivatives of the measured IR absorbance spectra at 155 and 160 K for 0 and 120 minutes. For these measurements, the sums of the second derivatives of two Gaussian lines, shown in red, underestimate the areas of the *b* and *a* components.

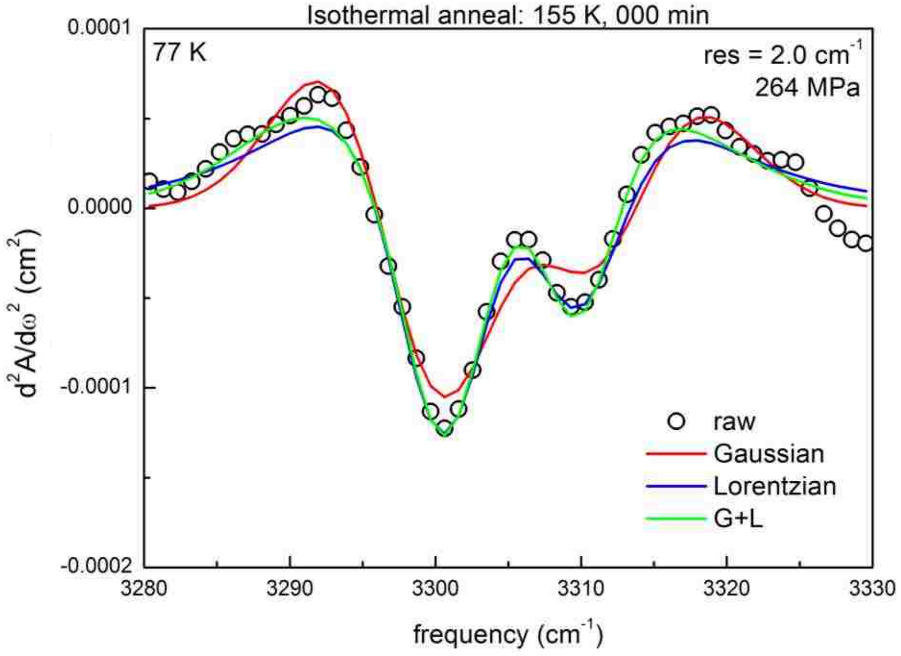
Isothermal anneal: 155 K, 000 min
77 K
res = 2.0 cm^{-1}
264 MPa
$d^2A/d\omega^2$ (cm^2)
0.0001
0.0000
-0.0001
-0.0002
3280
3290
3300
3310
3320
3330
frequency (cm^{-1})
raw
Gaussian
Lorentzian
G+L

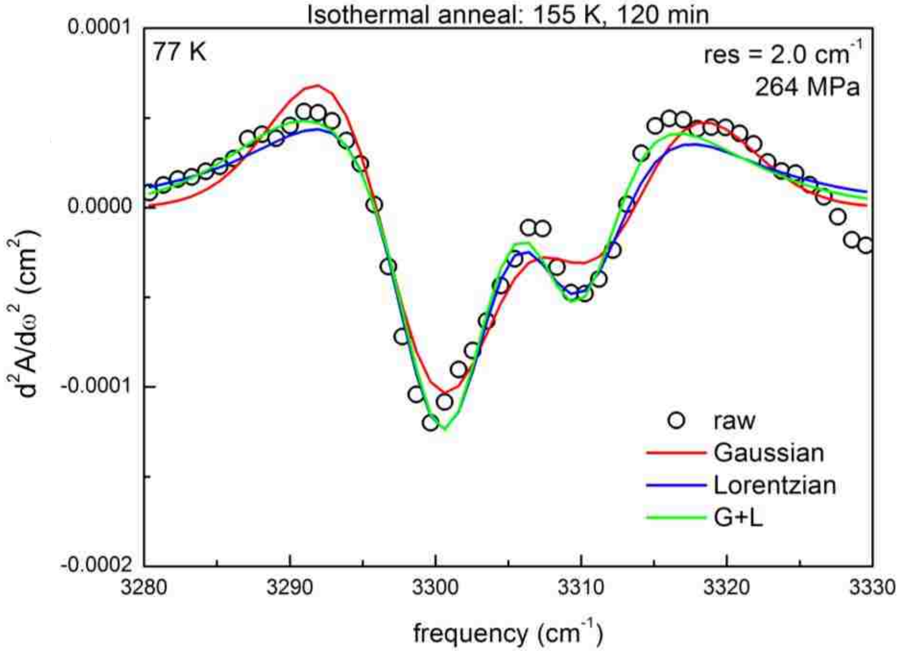
Isothermal anneal: 155 K, 120 min
77 K
res = 2.0 cm^{-1}
264 MPa
$d^2A/d\omega^2$ (cm^2)
0.0001
0.0000
-0.0001
-0.0002
3280
3290
3300
3310
3320
3330
frequency (cm^{-1})
raw
Gaussian
Lorentzian
G+L

[redacted]

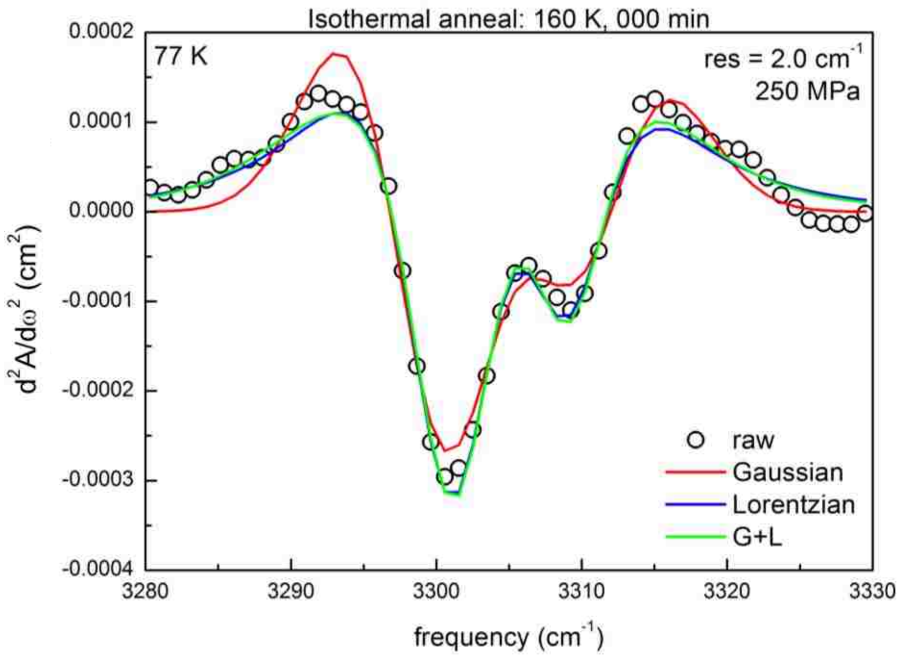
Isothermal anneal: 160 K, 000 min
77 K
res = 2.0 cm^{-1}
250 MPa
0.0002
0.0001
0.0000
-0.0001
-0.0002
-0.0003
-0.0004
d^{2}A/dω^2 (cm^2)
3280
3290
3300
3310
3320
3330
frequency (cm^{-1})
raw
Gaussian
Lorentzian
G+L

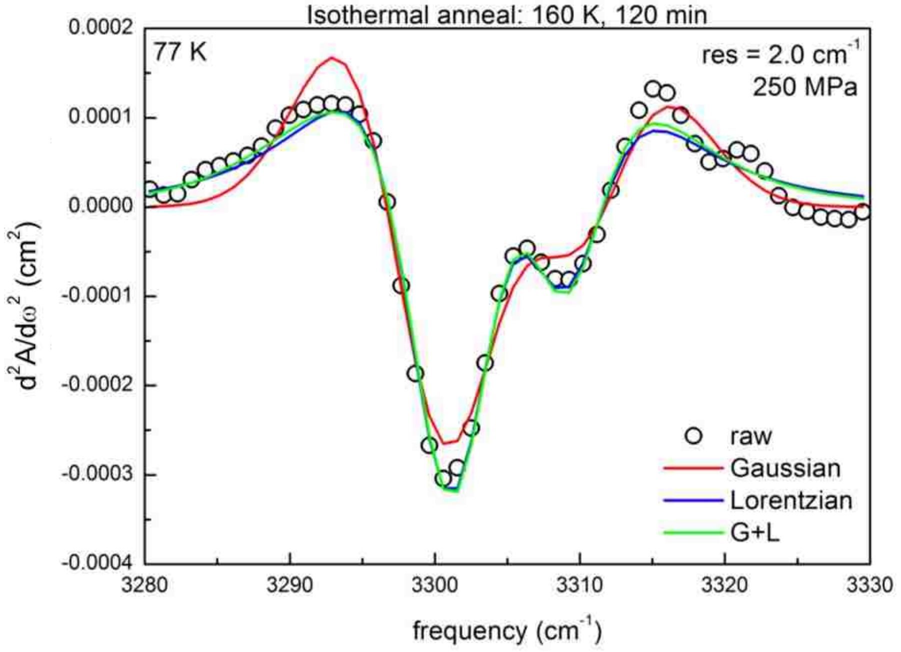
Isothermal anneal: 160 K, 120 min
77 K
res = 2.0 cm^{-1}
250 MPa
0.0002
0.0001
0.0000
-0.0001
-0.0002
-0.0003
-0.0004
d^{2}A/dω^2 (cm^2)
3280
3290
3300
3310
3320
3330
frequency (cm^{-1})
raw
Gaussian
Lorentzian
G+L

[redacted]

The sums of the second derivatives of two additional line shapes, a pure Lorentzian line and a mixed Gaussian-Lorentzian line, produced better fits to the data. The standard Lorentzian line shape with integrated absorbance a_0, center frequency a_1, and width $a_{2\mathrm{L}}$ is given by,

$$L(\omega) = \frac{a_0}{a_{2\mathrm{L}}\pi}\left[1 + \left(\frac{\omega - a_1}{a_{2\mathrm{L}}}\right)^2\right]^{-1} \qquad \textbf{Eq. (4.4.1)}$$

and the second derivative of this line shape is given by,

$$\frac{d^2L}{d\omega^2} = \frac{2}{{a_{2\mathrm{L}}}^2}\frac{1}{\left[1 + \left(\frac{\omega - a_1}{a_{2\mathrm{L}}}\right)^2\right]}\left[\frac{4(\omega - a_1)^2}{{a_{2\mathrm{L}}}^2\left[1 + \left(\frac{\omega - a_1}{a_{2\mathrm{L}}}\right)^2\right]} - 1\right]L(\omega). \qquad \textbf{Eq. (4.4.2)}$$

The mixed Gaussian-Lorentzian line has an expression of the form,

$$y(\omega) = a_3G(\omega) + (1 - a_3)L(\omega).$$

In addition to the area, center frequency, and widths of the Gaussian and Lorentzian lines, an additional parameter, a_3, is used to control the amount of Gaussian-Lorentzian character of the mixed line. For a pure Gaussian line, $a_3 = 1$, and for a pure Lorentzian line, $a_3 = 0$. As the intrinsic widths of the Gaussian and Lorentzian lines are different, the standard widths for each line shape were converted to a common FWHM parameter, Γ, by,

$$a_{2\mathrm{G}} = \Gamma/(2\sqrt{2\ln(2)})$$

and $$a_{2\mathrm{L}} = \Gamma/2.$$

By using a common FWHM, the number of fit parameters for each stress-split component is reduced to four: a_0, a_1, Γ, and a_3. The second derivative of the mixed Gaussian-Lorentzian function is given by,

$$\frac{d^2y}{d\omega^2} = a_3 \frac{d^2G}{d\omega^2} + (1 - a_3)\frac{d^2L}{d\omega^2}. \qquad \textbf{Eq. (4.4.3)}$$

The fits to the second derivatives of the absorbance spectra using the second derivatives of the different line shapes are shown in Figs. 4.4.4 and 4.4.5. For the mixed Gaussian-Lorentzian lines shapes, a_3 was varied for t=0 and then fixed at that value for all subsequent annealing times. For both temperatures and both sets of annealing times shown in the figures, the Lorentzian and mixed Gaussian-Lorentzian line shapes not only provided better fits to the data than the pure Gaussian line shape, these fits are also comparable to one another.

Table 4.4.1: Line shape parameters for the *b* and *a* components of the H_i^+ center in In_2O_3 under [001] stress prior to isothermal annealing at temperature T_{anneal}.

T_{anneal} (K)	b_1 (cm^{-1})	Γ_b (cm^{-1})	b_3	a_1 (cm^{-1})	Γ_a (cm^{-1})	a_3
153	3301.38	15.0	0.132	3308.92	14.2	0.000
155	3300.60	15.2	0.398	3309.75	14.9	0.192
157	3301.00	15.2	0.562	3310.32	15.0	0.060
160	3301.14	15.2	0.132	3308.98	14.2	0.072

Table 4.4.1 lists the center frequency, FWHM, and Gaussian/Lorentzian character parameters for the *b* and *a* components for the mixed Gaussian-Lorentzian fits to the second derivatives of the absorbance spectra of [001-oriented In_2O_3 samples under stress but prior to annealing. Except for a_3 of component *b* at 157 K, all of the mixed Gaussian-Lorentzian lines have values for a_3 closer to zero than to one. Due to this dominant Lorentzian character, we chose to use the second derivatives of Lorentzian line shapes to fit the isothermal annealing data at all temperatures.

Stress-induced alignments are usually quantified by the dichroic ratio, $\mathcal{D}$, which was defined in Chapter 2 by Eq. (2.2.16),

$$\mathcal{D} = \frac{\alpha_{\perp} - \alpha_{||}}{\alpha_{\perp} + \alpha_{||}}, \qquad \textbf{Eq. (4.4.4)}$$

in which $\alpha_{||}$ and $\alpha_{\perp}$ are the absorption coefficients for a single absorption peak for the parallel and perpendicular polarized light beams relative to the stress direction. The numerator of Eq. (4.4.4) reflects the changes in the populations of the different orientations of the defect, and the denominator of Eq. (4.4.4) is a normalization factor proportional to the total defect population.

Wen[12] modified this expression in an analysis of the stress-induced alignment of the D-N-D center formed in $GaAs_{1-x}N_x$ alloys. Coincidently, the D-N-D center possesses the same symmetry as the H_i^+ defect being studied in this chapter: [110] monoclinic with the transition moment of the defect lying in the plane perpendicular to the [110] primary axis of the defect. Wen observed a [110] stress-induced alignment due to a local reorientation (canting distortion) of the D-N-D center, which was observed in the IR-absorbance spectra as an increase in the intensity of component e_1 and decrease in the intensity of component e_2. The following quantity was used to analyze these data,

$$\frac{\left[I\left(e_{2,\parallel}\right) + I\left(e_{2,\perp}\right)\right] - \left[I\left(e_{1,\parallel}\right) + I\left(e_{1,\perp}\right)\right]}{\left[I\left(e_{2,\parallel}\right) + I\left(e_{2,\perp}\right)\right] + \left[I\left(e_{1,\parallel}\right) + I\left(e_{1,\perp}\right)\right]}. \qquad \textbf{Eq. (4.4.5)}$$

For the H_i^+ defect, anneals near 160 K cause an increase in the intensity of component *b* and decrease in the intensity of component *a*. For our experiments, changes in the intensities of the *b* and *a* families of defects are most easily determined from the spectra measured for [001] stress with **E** perpendicular to the stress for which the components are clearly separated. Therefore, changes in the **E**||[010] absorbance spectra were used to quantify the [001] stress-induced alignment. The quantity P is defined such that,

$$P_\gamma(T) = I_\gamma(T)/I_{\gamma 0}, \qquad \textbf{Eq. (4.4.6)}$$

in which $I_\gamma(T)$ is the area of a stress-split component, γ, for the **E**||[010] polarization after an anneal at temperature T, and $I_{\gamma 0}$ is the area of this component immediately after the application of stress at 6 or 77 K where reorientation cannot occur. The [001] stress-induced alignment can be characterized by the quantity,

$$\frac{P_b - P_a}{P_b + P_a} = \frac{I_b(T)/I_{b0} - I_a(T)/I_{a0}}{I_b(T)/I_{b0} + I_a(T)/I_{a0}}. \qquad \textbf{Eq. (4.4.7)}$$

According to Eq. (4.4.7), values of $(P_b - P_a)/(P_b + P_a)$ differing from zero are due to a stress-induced alignment of the H_i^+ center. If the reorientation kinetics of the alignment is a first order process, then $(P_b - P_a)/(P_b + P_a)$will obey the expression,

$$\frac{P_b - P_a}{P_b + P_a} = B_{\text{max}}\left[1 - \exp\left(-\frac{t}{\tau^*}\right)\right]. \qquad \textbf{Eq. (4.4.8)}$$

In this expression, B_{max} is the maximum value of $(P_b - P_a)/(P_b + P_a)$ due to the saturation of the stress-induced alignment and $\tau^*(T)$ is the time constant for the alignment of the H_i^+ center under [001] stress at temperature T. Tables 4.4.2 and 4.4.3 show the values of $(P_b - P_a)/(P_b + P_a)$ calculated from I_b and I_a for the isochronal and the isothermal anneals, respectively. The uncertainties in the values of I_b and I_a were propagated using standard techniques[13] to determine the uncertainty in $(P_b - P_a)/(P_b + P_a)$.

Table 4.4.2: Integrated absorbance of the [001] stress-split components and $(P_b - P_a)/(P_b + P_a)$ for isochronal anneals for 15 minutes at successively increasing temperatures.

Date	T_{anneal} (K)	I_b (x10^{-2}cm^{-1})	I_a (x10^{-2}cm^{-1})	$(P_b - P_a)/(P_b + P_a)$
06/09/16 256 MPa	10	9.7 ± 0.1	5.15 ± 0.05	0.000
	145	9.7 ± 0.1	5.07 ± 0.05	0.004 ± 0.010
	160	9.8 ± 0.1	4.90 ± 0.05	0.026 ± 0.010
	175	9.9 ± 0.1	4.88 ± 0.05	0.035 ± 0.010
06/10/16 270 MPa	10	9.7 ± 0.1	5.76 ± 0.05	0.000
	145	9.9 ± 0.1	5.91 ± 0.05	0.000 ± 0.010
	160	9.8 ± 0.1	5.46 ± 0.05	0.031 ± 0.010
	175	10.0 ± 0.1	5.49 ± 0.05	0.042 ± 0.010
05/12/16 265 MPa	77	17.9 ± 0.2	9.8 ± 0.1	0.000
	165	17.5 ± 0.1	9.1 ± 0.1	0.022 ± 0.011
05/19/16 265 MPa	77	16.0 ± 0.2	6.9 ± 0.1	0.000
	165	15.8 ± 0.2	6.5 ± 0.1	0.022 ± 0.014
	180	16.0 ± 0.2	6.4 ± 0.1	0.038 ± 0.014
05/24/16 265 MPa	77	18.3 ± 0.2	8.4 ± 0.1	0.000
	145	18.2 ± 0.2	8.2 ± 0.1	0.006 ± 0.012
	160	17.8 ± 0.2	7.9 ± 0.1	0.011 ± 0.011
	175	18.6 ± 0.2	7.7 ± 0.1	0.048 ± 0.012
07/08/16 265 MPa	77	5.5 ± 0.1	3.10 ± 0.05	0.000
	110	5.6 ± 0.1	3.13 ± 0.05	0.002 ± 0.019
	162	5.5 ± 0.1	3.02 ± 0.05	0.005 ± 0.018
	215	5.0 ± 0.1	2.59 ± 0.05	0.037 ± 0.017
	240	4.4 ± 0.1	2.29 ± 0.05	0.029 ± 0.017

Table 4.4.3: Integrated absorbance of the [001] stress-split components and $(P_b - P_a)/(P_b + P_a)$ for isothermal anneals at 153, 155, 157, and 160 K.

Date	t (min)	I_b (x10^{-2}cm^{-1})	I_a (x10^{-2}cm^{-1})	$(P_b - P_a)/(P_b + P_a)$
153 K 01/20/17 250 MPa	0	36.6 ± 0.4	20.6 ± 0.2	0.000
	30	29.9 ± 0.4	16.4 ± 0.2	0.011 ± 0.011
	60	33.0 ± 0.4	17.4 ± 0.2	0.033 ± 0.011
	90	33.5 ± 0.4	17.4 ± 0.2	0.041 ± 0.011
	120	31.0 ± 0.4	16.2 ± 0.2	0.034 ± 0.011
	180	34.6 ± 0.4	17.4 ± 0.2	0.056 ± 0.011
155 K 01/05/17 264 MPa	0	17.8 ± 0.2	10.7 ± 0.1	0.000
	20	17.6 ± 0.2	10.5 ± 0.1	0.006 ± 0.011
	40	17.7 ± 0.2	10.3 ± 0.1	0.019 ± 0.011
	60	17.6 ± 0.2	10.1 ± 0.1	0.025 ± 0.011
	90	17.9 ± 0.2	9.9 ± 0.1	0.047 ± 0.011
	120	17.5 ± 0.2	9.8 ± 0.1	0.036 ± 0.011
	150	16.9 ± 0.2	9.1 ± 0.1	0.053 ± 0.010
157 K 01/02/17 264 MPa	0	17.3 ± 0.2	8.6 ± 0.1	0.000
	30	17.6 ± 0.1	8.4 ± 0.1	0.029 ± 0.013
	60	15.1 ± 0.2	6.7 ± 0.1	0.057 ± 0.012
	90	16.8 ± 0.2	7.4 ± 0.1	0.067 ± 0.013
	120	16.7 ± 0.2	7.4 ± 0.1	0.059 ± 0.013
	150	15.1 ± 0.2	6.6 ± 0.1	0.060 ± 0.012
	180	15.0 ± 0.2	6.7 ± 0.1	0.049 ± 0.012
157 K 01/04/17 264 MPa	0	15.2 ± 0.2	9.0 ± 0.1	0.000
	15	15.6 ± 0.2	9.1 ± 0.1	0.010 ± 0.012
	45	15.6 ± 0.2	8.6 ± 0.1	0.037 ± 0.012
	75	16.8 ± 0.2	9.0 ± 0.1	0.058 ± 0.013
	105	15.5 ± 0.2	8.4 ± 0.1	0.045 ± 0.012
160 K 01/20/17 250 MPa	0	29.4 ± 0.4	14.7 ± 0.2	0.000
	20	29.0 ± 0.4	13.7 ± 0.2	0.029 ± 0.013
	40	31.7 ± 0.4	14.9 ± 0.2	0.034 ± 0.013
	60	32.5 ± 0.4	15.0 ± 0.2	0.042 ± 0.014
	120	29.0 ± 0.4	12.8 ± 0.2	0.058 ± 0.013
	180	38.3 ± 0.4	16.9 ± 0.2	0.077 ± 0.015

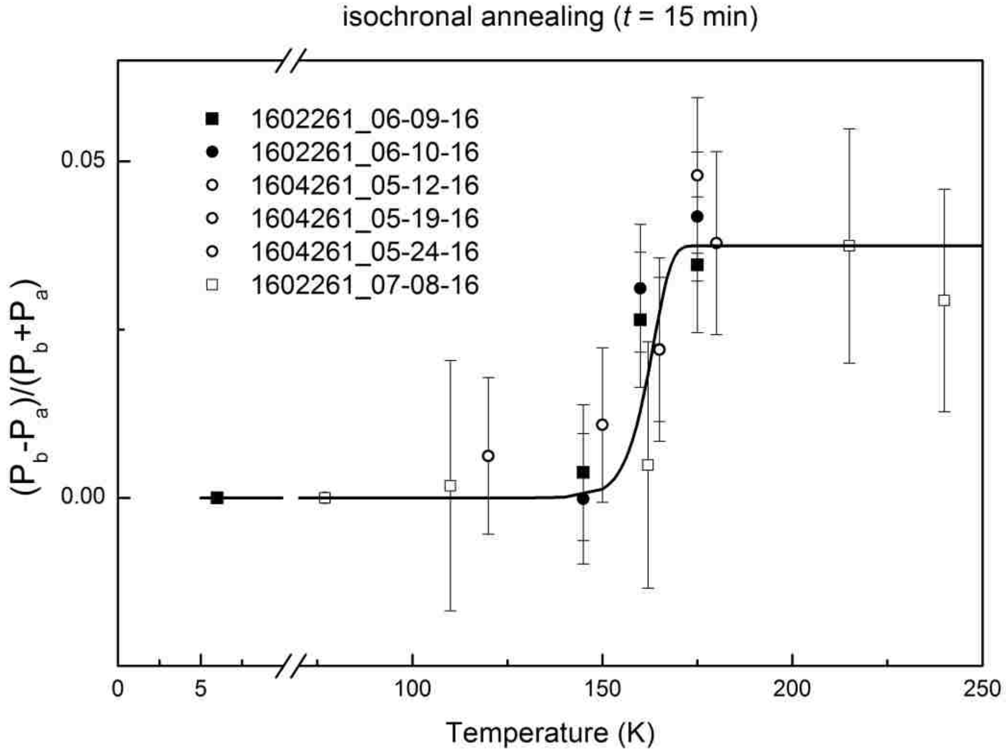

[redacted]

Figure 4.4.6 shows a plot of $(P_b - P_a)/(P_b + P_a)$ versus the annealing temperature for the isochronal annealing data shown in Table 4.4.2. The 15-minute anneal at 165 K produced a stress-induced alignment that is approximately half of the value produced by a 15-minute anneal at a higher temperature, for which the equilibrium value can be achieved. Equation (4.4.8) can be rewritten to solve for $\tau^*(165\ \mathrm{K})$,

$$0.5 = \left[1 - \exp\left(-\frac{t}{\tau^*(165\ \mathrm{K})}\right)\right]$$

$$\frac{1}{\tau^*(165\ \mathrm{K})} = -\frac{1}{t}\ln[0.5] = -\frac{\ln[0.5]}{(900 \pm 90\ \mathrm{s})}.$$

These calculations yield a time constant for the alignment of the H_i^+ defect by stress of $\tau^*(165\ K) = (1.3\pm0.3)$ x 10^3 s.

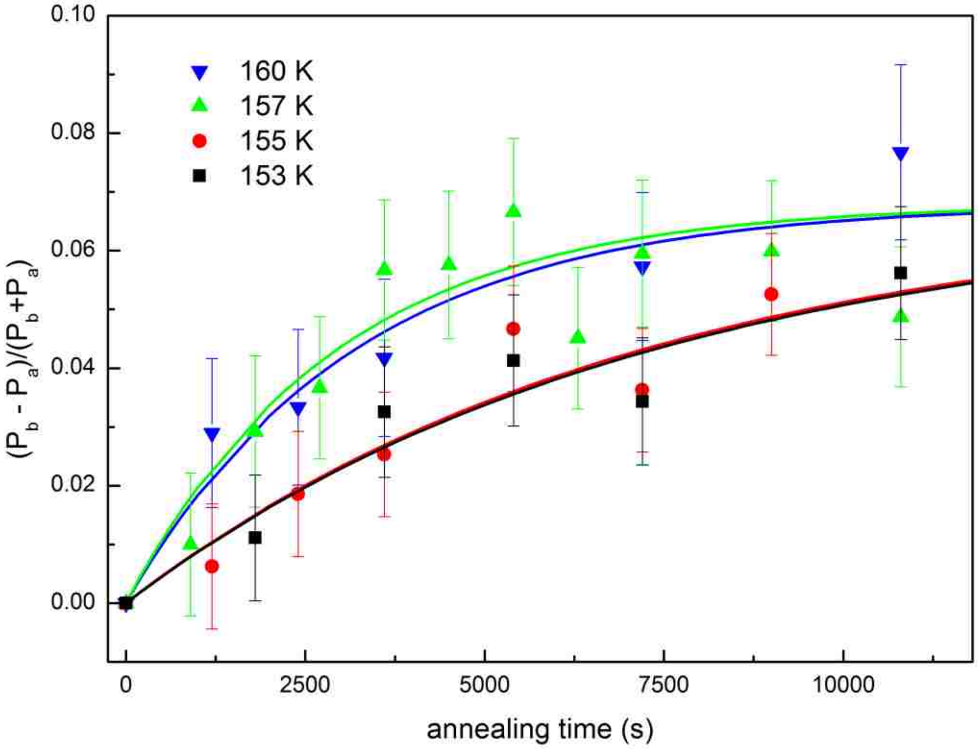

[redacted]

Figure 4.4.7 shows $(P_b - P_a)/(P_b + P_a)$ versus annealing temperature for the isothermal annealing data listed in Table 4.4.3. The data for all four temperatures, 153, 155, 157, and 160 K, were fit simultaneously to Eq. (4.4.8) with five parameters: a common $B_{\max}$ and the time constants for the H_i^+ stress-induced alignment for each of the annealing temperatures. The fit parameters are listed in Table 4.4.4. The time constants for the H_i^+ stress-induced alignment for the high temperature (157 and 160 K) anneals are shorter than the time constants for the low temperature (153 and 155 K) anneals, as expected. The progression, however, is not monotonic due to the scatter of the data, which could be reduced for the 160 K anneal by measuring additional annealing times, e.g., around 5000 and 9000 seconds, and for the 153 and 155 K anneals by measuring longer annealing times.

4.4.2: Computational Results: Motion of H_i^+ in In_2O_3

In Chapter 2, the H-B acceptor complex in Si was discussed as an example for which the stress-induced alignment of this defect results from a preferential alignment of the defect between its different bond-centered configurations. Professor W. Beall Fowler has performed theoretical calculations using CRYSTAL06 to study the possible types of motion of H_i^+ in In_2O_3.[14] The results of these calculations give insights into the mechanism of the [001] stress-induced alignment for H_i^+ in In_2O_3. Figure 4.4.8(a) shows the In_2O_3 lattice containing the lowest (red) and next higher (green) energy sites for H_i^+. There are two equivalent minimum-energy H_i^+ sites on adjacent O atoms; directly above them on the neighboring O atoms are the two higher-energy sites. The most energetically favorable motion of H_i^+ is “back and forth” hopping between the minimum-energy sites. This type of motion does not lead to diffusion.

In order for diffusion to occur, an H_i^+ must leave the initial cluster and reach the low energy site on an adjacent O, such as the one shown in Fig. 4.4.8(b). There are two types of motions that could lead to H_i^+ diffusion. The first motion involves H_i^+ moving from a low-energy site to the higher-energy site on the same O atom, jumping to the higher-energy site on an adjacent O, and then relaxing to a low-energy site on this same O.

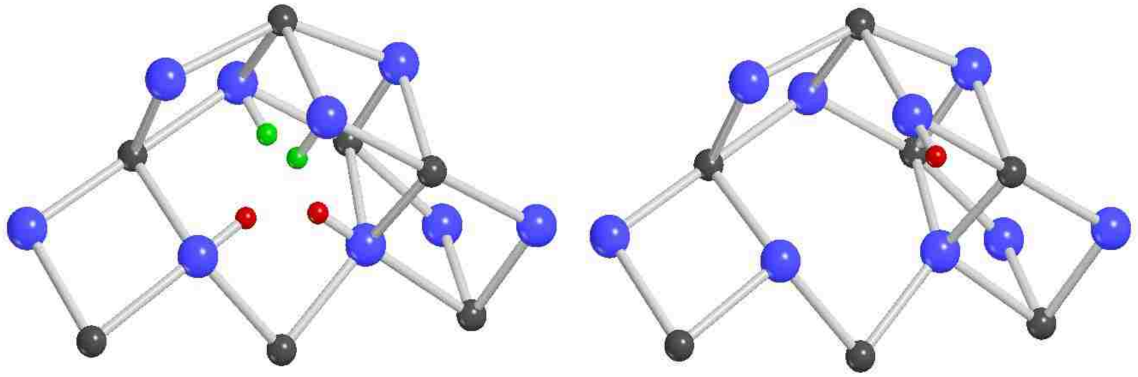

[redacted] [redacted]

[redacted]

In the second motion, H_i^+ jumps from its low-energy site to the high-energy site on an adjacent O within the same cluster, and then relaxes to the low-energy site on this O. Although the experimental data does not distinguish between the two types of motions, the second motion (jump to adjacent O followed by a rotation) has a lower activation barrier compared to the first motion, and will be considered as the most likely path for a diffusion jump. Notice that this diffusion jump requires that H_i^+ overcomes an energy barrier of at least 0.51 eV, which is the energy difference between the metastable and low energy configurations.

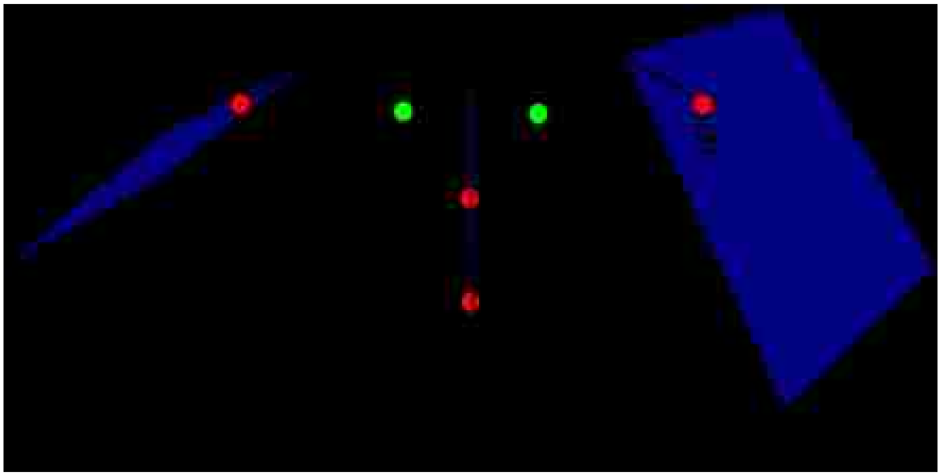

A diffusion jump along the pathway shown in Fig. 4.4.9 is also the process by which a defect alignment can be produced by stress (or annealed away in the absence of stress). A H_i^+ center with its primary axis in either a (110) or $(1\bar{1}0)$ plane, that contributes to component *a* in the IR spectrum under [001] stress, is converted to a H_i^+ center with a primary axis in either a (011), $(01\bar{1})$, (101), or $(10\bar{1})$ plane that contributes to component *b*. Thus, the combination of experimental and computational results suggests that the changes in the IR absorbance spectra under [001] stress at elevated temperatures are due to the diffusion of the H_i^+ center.

4.4.3: Point-Defect Relaxations and H Diffusion Constant

Nowick and Berry[11] have worked out the general cases that relate the diffusivity of a defect to the time constant τ^* of a stress-induced alignment of that defect. Assuming that there are no reactions among the different species of defects and that the concentration of defects is dilute so there are no interactions between defects of the same species, then Eq. (4.4.9) can be used to model the diffusion.

$$D_H = \frac{1}{6}\Gamma d^2 \qquad \textbf{Eq. (4.4.9)}$$

In this equation, d is the jump distance between the initial and final sites, and Γ is the mean jump rate, given by $\Gamma = \omega/z$, where ω is the fundamental frequency for a single diffusion jump (i.e., the reciprocal of the relaxation time $1/\tau$) and z is the number of equivalent directions in which the jump can occur. These conditions are satisfied in these experiments as the total intensity of the stress-split 3306 cm^{-1} line remains constant (i.e., no conversion into other OH species) and the concentration of H defects in similar samples has been estimated to be on the order of 10^{18} cm^{-3}. The diffusion-jump process suggested in Section 4.4.2 has $z = 2$ since there are two equivalent jumps that can occur, so Eq (4.4.9) becomes,

$$D_H = \omega\frac{d^2}{3} = \frac{d^2}{3\tau}.$$

It remains to relate the time constant for the alignment under [001] stress, τ^*, to the time constant for a single diffusion jump, τ. Nowick and Berry[11] have determined the general expressions for τ^* in terms of the specific reorientation (or jump) frequencies ν_{pq} between defect sites p and q, which depend only on the symmetry of the defect, the symmetry of the host crystal, and the direction of the applied stress. For a [110] monoclinic defect in a cubic crystal, there are twelve possible orientations of the defect, whose unit vector transition dipole moments are given in Table 4.3.1. The expression for the relaxation of a [110] monoclinic defect under [001] uniaxial stress is given by Eq. (4.4.10),

$$\frac{1}{\tau^*} = 3\left(2\nu_{1,11} + \nu_{1,9} + \nu_{1,10}\right). \qquad \textbf{Eq. (4.4.10)}$$

The defect labeling corresponds to the different transition moment directions listed in Table 4.3.1. In Eq. (4.4.10), 1 refers to one of the initial H_i^+ sites and 9 and 11 refer to the minimum energy sites located on an adjacent O atom which is outside the cluster (Fig. 4.4.7(b)). Figure 4.4.9 shows a model for the diffusion pathway with the sites labeled. The p = 9 and 11 sites are predicted to have the largest jump rates ($\therefore \nu_{1,10} = 0$) and to have similar jump pathways. If their reorientation frequencies are assumed to be equal, then $\nu_{1,9} = \nu_{1,11} = \tau^{-1}$. These considerations simplify Eq. (4.4.10) to give,

$$\frac{1}{\tau^*} = 3\left(2\frac{1}{\tau} + \frac{1}{\tau}\right) = \frac{9}{\tau},$$

and the diffusivity of H_i^+ at temperature T is,

$$D_{\mathrm{H}}(\mathrm{T}) = \frac{d^2}{27\tau^*}. \qquad \textbf{Eq. (4.4.11)}$$

The jump distance d between the closest minimum energy H_i^+ sites determined from the CRYSTAL06 calculations is 3.003 Å. Using the time constants listed in Table 4.4.4, the diffusivity of H_i^+ at each annealing temperature was calculated. For example, with τ^*(165 K) = $(1.3\pm0.3)\times10^3$ s, the diffusivity for H_i^+ at 165 K is,

$$D_{\mathrm{H}}(165\ \mathrm{K}) = \frac{(3.003 \times 10^{-8}\ \mathrm{cm})^2}{27(1.3 \pm 0.3) \times 10^3\ \mathrm{s}} = (2.6 \pm 0.2) \times 10^{-20}\ \mathrm{cm}^2/\mathrm{s}.$$

The diffusivities for H_i^+ due to the stress-induced alignment at temperatures between 153 and 165 K are listed in Table 4.4.4.

Table 4.4.4: Time constants for the stress-induced alignment and diffusivities of the H_i^+ defect at different annealing temperatures. The parameter $B_{\max}$ is 0.068 ± 0.005. The uncertainties in the time constants are determined from the scatter of the data about the fit curve. The diffusivities are calculated from the time constant using Eq. (4.4.11).

Sample	**T_{anneal} (K)**	**$\tau^*(T)$ x10^3 (s)**	**$D_H(T)$ x10^{-21} (cm^2/s)**
1612293	153	7.2 ± 1.3	4.6 ± 0.9
1602261	155	7.2 ± 1.2	4.7 ± 0.8
1602261	157	2.9 ± 0.6	11.4 ± 0.2
1612293	160	3.2 ± 0.7	10.5 ± 0.2
1604261	165	1.3 ± 0.3	26 ± 2

Qin[15] has measured the H_i^+ in-diffusion depth profiles resulting from annealing treatments of In_2O_3 samples in an H_2 ambient and has analyzed the out-diffusion of H_i^+ from hydrogenated In_2O_3 samples. These experiments yielded values for the diffusivity of H_i^+ at 300, 325, 350, 375, 400, 425, and 450°C, which are given in Table 4.4.5.

Table 4.4.5: Diffusivities of the H_i^+ defect determined from bulk diffusion experiments of hydrogen into In_2O_3 single crystals from Qin.[15]

T_{anneal} (°C)	**T_{anneal} (K)**	**$D_H(T)$ x10^{-10} (cm^2/s)**
300	573	1.4 ± 0.2
325	598	7.4 ± 0.2
350	623	2.9 ± 0.2
375	648	5.9 ± 0.3
400	673	9.5 ± 0.2
425	698	10.9 ± 0.2
450	723	10.4 ± 0.2

The diffusivities determined from the bulk in- and out- diffusion experiments and the uniaxial stress measurements extend across 10 decades. These results are shown in a semi-log plot D_H vs. $1000/T^{-1}$ in Fig 4.4.10.

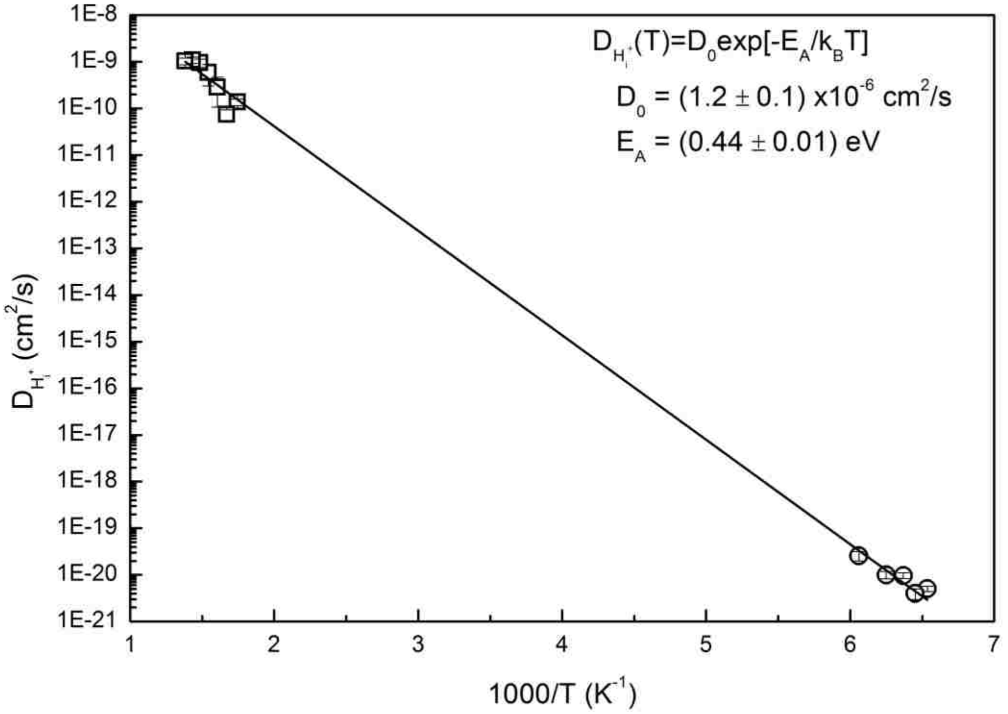

[redacted]

A linear regression to these combined data yields an expression for the diffusivity of H_i^+ in In_2O_3 of,

$$D_{\mathrm{H}} = (1.2 \pm 0.1) \times 10^{-6}\mathrm{cm}^2/\mathrm{s}\ \exp[-(0.44 \pm 0.01)\ \mathrm{eV}/\mathrm{k_b T}].$$

The experimental activation energy for diffusion of 0.44 eV is remarkably close to the energy difference of 0.51 eV between the H_i^+ minimum energy configuration and the next higher metastable state and implies that this metastable state is crucial in the diffusion pathway of H_i^+. Recent experiments[5] which investigated the motion of muons in In_2O_3 found a similar activation energy (0.46 eV) and suggest that the diffusion-jump process proposed for H_i^+ also applies to the muon.

4.5: Summary

Fourier Transform Infrared spectroscopy in conjunction with uniaxial stress has been used to study the symmetry of the H_i^+ shallow donor and of additional OH defects in single crystal In_2O_3. The H_i^+ center has C_{1h} symmetry and a transition moment oriented 7° from a <111> direction, which is in good agreement with the structure predicted by Fowler with first-principles theory. The OH centers at 3357 and 3373 cm^{-1} have trigonal symmetry. A stress-induced alignment of the 3306 cm^{-1} center occurs in [001]-oriented samples annealed under stress at temperatures between 153 and 165 K. Theory predicts that the process by which the H_i^+ defect reorients between inequivalent orientations under [001] stress is also a diffusion jump. Thus, the reorientation kinetics of the 3306 cm^{-1} H_i^+ center reveal the microscopic process by which H_i^+ diffuses in In_2O_3 and provides an elegant spectroscopic strategy for determining the diffusion constant from the time constant for a single hydrogen jump.

4.6: References

1. M. Marezio. Refinement of the crystal structure of In_2O_3 at two wavelengths. *Acta Crystallogr.* **20**, 723 (1966).

2. S. Limpijumnong, *et al.* Hydrogen doping in indium oxide: An ab initio study. *Phys. Rev. B* **80**, 193202 (2009). https://doi.org/10.1103/PhysRevB.80.193202

3. I. Hamberg & C. G. Granqvist. Evaporated Sn-doped In_2O_3 films: Basic optical properties and applications to energy-efficient windows. *J. Appl. Phys.* **60,** R123 (1986).

4. T. Koida, H. Fujiwara, & M. Kondo. Hydrogen-doped In_2O_3 as high-mobility transparent conductive oxide. *Jap. J. Appl. Phys.* **46**, L685-687 (2007).

5. B. B. Baker, *et al.* Motional characteristics of positively charged muonium defects in In_2O_3. *AIP Conf. Proc.* **1583**, 323 (2014).

6. B. Baker. Charged Muonium Diffusion in Indium Oxide and Other Transparent Conducting Oxides. (Texas Tech University, 2015).

7. W. Yin, *et al.* Hydrogen centers and the conductivity of In_2O_3 single crystals. *Phys. Rev. B* **91**, 075208 (2015).

8. D. R. Hagleitner, *et al.* Bulk and surface characterization of In_2O_3 (001) single crystals. *Phys. Rev. B* **85**, 115441 (2012).

9. A. A. Kaplyanskii. Noncubic centers in cubic crystals and their piezospectroscopic investigation. *Opt. Spectrosc.* **16**, 329 (1964).

10. G. Davies, *et al.* The 3942-cm^{-1} optical band in irradiated silicon. *Phys. Rev. B* **35**, 2755 (1987).

11. A. S. Nowick & B. S. Berry. Anelastic Relaxation in Crystalline Solids. (Academic Press, 1972).

12. L. Wen. Experimental Study of H-N-H Centers in Dilute III-N-V Alloys by Low-Temperature Vibrational Spectroscopy and Uniaxial-Stress Methods. (Lehigh University, 2010).

13. J. R. Taylor. An Introduction to Error Analysis: The Study of Uncertainties in Physical Measurements. (University Science Books, 1997).

14. R. Dovesi, *et al.* Crystal06 User's Manual. (2006).

15. Y. Qin. Private communication. (2017).

Chapter 5

Hydrogen Centers in β–Ga_2O_3

5.1: Introduction

Over the past decade, gallium oxide (Ga_2O_3) has become one of the most widely studied TCOs. Its large band gap of 4.9 eV makes it transparent for ultraviolet (UV) wavelengths, making it one of the few TCOs that can be used for UV-transparent applications.[1] There is also considerable interest in its use for high-power electronics.[2] The Baliga figure-of-merit (FOM)[3], which is given by Eq. (5.1.1),

$$\text{Baliga FOM} = \frac{\mu \varepsilon_r {E_c}^3}{\text{FOM(Si)}}, \qquad \textbf{Eq. (5.1.1)}$$

is a unitless parameter that estimates a material's potential for high power device applications based on minimizing the conduction losses, and is calculated from the electron mobility μ, the relative dielectric constant ε_r, and the critical electric field where device breakdown occurs, E_c. The Baliga FOM is defined relative to the performance of Si, i.e., the FOM for other materials is normalized with respect to the value for Si. The theoretical Baliga FOM for β–Ga_2O_3 is 3444, which is 10 times larger than the FOM of SiC and nearly 4 times larger than the FOM of GaN. The Baliga FOM for β–Ga_2O_3 is based on the theoretical E_C of 8 MV/cm. An experimental value of E_c=3.8 MV/cm has already been demonstrated[4] for a Sn-doped β–Ga_2O_3 metal-oxide semiconductor field effect transistor (MOSFET).

Of the five structural polymorphs (α, β, γ, δ, ε), the monoclinic (β) structure is most commonly studied because it is stable up to its melting point of 1,795 °C, whereas the other four phases are metastable and convert into the β structure at temperatures between 750 and 900 °C.[5] The lattice parameters for the $\beta\text{–}Ga_2O_3$ structure were first reported by Geller[6] in 1960. Recent measurements by Ahman and coworkers[7] found lattice parameters similar to those of Geller, but with a factor of 10 improvement in the precision of these values. The experimental lattice parameters for $\beta\text{–}Ga_2O_3$ are a = 12.214±0.003 Å, b = 3.0371±0.0009 Å, c = 5.7981±0.0009 Å, and β = 103.83±0.02°.[7] Figure 5.1.1 shows the conventional unit cell of $\beta\text{–}Ga_2O_3$. The crystal contains two inequivalent Ga sites and three inequivalent O sites. Gallium (1) is tetrahedrally coordinated, and Ga(2) is octahedrally coordinated. Of the three O sites, O(1) and O(2) are trigonally coordinated and O(3) is tetrahedrally coordinated.[8] Over the past decade, the improvements in various growth techniques, e.g. Czochralski,[9,10] floating zone (FZ),[11] and edge-defined film-fed growth (EFFG),[12,13] have produced high quality $\beta\text{–}Ga_2O_3$ single crystals with (0 1 0) or (-2 0 1) surface orientations (see S. I. Stepanov *et al.*[14] and references within). The availability of these crystals has created opportunities for research that aim to understand more about the fundamental optical, electrical, and thermal properties of $\beta\text{–}Ga_2O_3$.

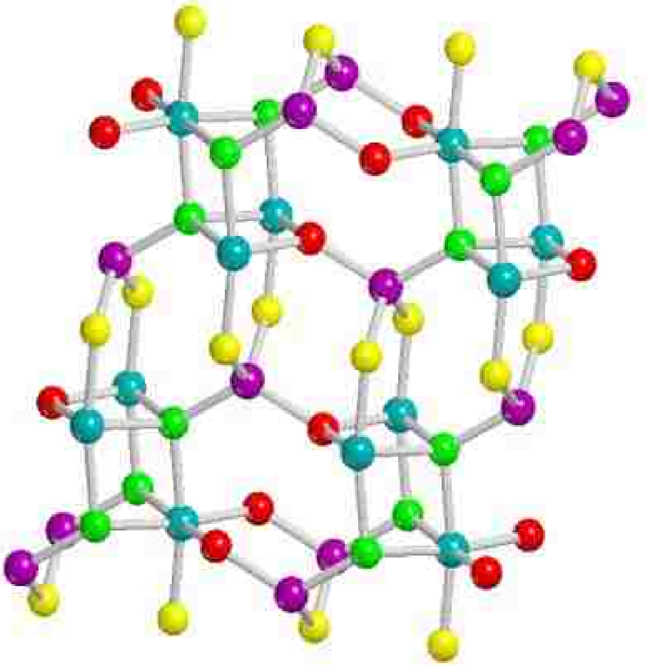

[redacted]

As with several other TCOs, early studies of the electrical conductivity in $\beta-Ga_2O_3$ single crystals concluded that oxygen vacancies were responsible for the unintentional *n*-type conductivity of undoped crystals.[15] However, theoretical calculations by Varley *et al.*[16] show that oxygen vacancies have high formation energies under both O-rich and O-poor growth conditions, and that they act as deep donors. Consequently, oxygen vacancies are unlikely to occur in large concentrations or be responsible for the unintentional *n*-type conductivity observed in as-grown $\beta-Ga_2O_3$ single crystals. Theoretical studies[8,17] have identified several impurities that could act as shallow donors in this material, including: Si, Sn, C, W, and Ge on a Ga site; F, Cl, and H on an O site;

and interstitial hydrogen (H_i). Of these impurities, there is experimental evidence for the shallow donor behavior of Si and Sn. Ueda *et al.*[11] produced highly conductive $\beta-Ga_2O_3$ single crystals via the floating zone (FZ) method by doping the crystal feed rods with Sn. M. Orita and coworkers[1] observed a similar effect in Sn-doped $\beta-Ga_2O_3$ thin films produced by pulsed-laser deposition. Villora *et al.*[18] demonstrated control of the electrical conductivity over three orders of magnitude by varying the concentration of Si incorporated during the growth process. Low-temperature scanning-tunneling microscopy/spectroscopy studies performed by Iwaya *et al.*[19] on Si-doped $\beta-Ga_2O_3$ single crystals confirmed the donor nature of Si impurities. Silicon is the most common impurity present in Ga_2O_3 powders used for bulk crystal growth. Therefore, it is suspected to be the origin of the *n*-type conductivity in the unintentionally doped crystals. A recent EPR study[20] of the electronic properties of the residual donor in unintentionally doped $\beta-Ga_2O_3$ single crystals suggests that Si is the dominant shallow donor. This donor could only be activated after high temperature annealing (N_2 1100 °C, 20 min), which suggests that substitutional Si impurities may be passivated by other defects.

There are only a few reported experiments that have explored the role of hydrogen on the conductivity of $\beta-Ga_2O_3$. Ahn *et al.*[21] observed an increase in the electrical conductivity of $\beta-Ga_2O_3$ crystals exposed to a deuterium plasma, but they noted that the increased conductivity could also result from plasma-induced surface effects. King *et al.*[22] found that the behavior of muonium injected into $\beta-Ga_2O_3$ powder is consistent with it being a shallow donor. Since muonium mimics the properties of hydrogen, this result suggests that hydrogen could also act as a shallow donor. There is reason to suspect, however, that hydrogen may influence the conductivity of $\beta-Ga_2O_3$ differently than its behavior in In_2O_3 and SnO_2. Varley *et al.*[23] calculated the formation energies of interstitial hydrogen, isolated cation vacancies, and cation vacancy-hydrogen complexes under O-rich and Ga-rich conditions. In both materials, the hydrogenated-cation vacancies (V_{In}-H and V_{Ga}-H) are more stable than the respective isolated vacancies, but the stabilities of the hydrogenated cation-vacancies relative to interstitial hydrogen are quite different. In *n*-type In_2O_3 grown under O-rich conditions, H_i is more stable than the V_{In}-H complexes. However, in *n*-type $\beta-Ga_2O_3$ under similar conditions, the V_{Ga}-H complexes are predicted to have lower formation energies than H_i by nearly 2 eV. The stability of V_{Ga}-H complexes adds an intriguing twist to the picture of hydrogen in $\beta-Ga_2O_3$. Cation vacancies are readily formed in *n*-type materials and can reduce the conductivity by giving rise to carrier recombination and scattering.[23] Positron-annihilation spectroscopy experiments performed by Korhonen and coworkers[24] on Si-doped $\beta-Ga_2O_3$ thin films showed that high concentrations of gallium vacancies (V_{Ga}) can be created during the growth process. The presence of these vacancies almost completely compensated the enhancement of the electrical conductivity due to the Si doping. The formation of hydrogenated cation-vacancies should passivate these acceptors and contribute to the *n*-type conductivity.

As with other TCOs, understanding the behavior of hydrogen in $\beta-Ga_2O_3$ single crystals is crucial for controlling the electrical and optical properties of this material. To my knowledge, there are no FTIR studies of hydrogen related defects in $\beta-Ga_2O_3$ reported in the literature. This chapter reports IR-spectroscopy studies of the chemical nature, thermal stability, and polarization properties of hydrogen centers formed in hydrogenated β–Ga_2O_3 single crystals.

5.2: Experimental Methods

Bulk, *n*-type β–Ga_2O_3 single crystals grown by the floating zone (FZ) method were purchased from MTI Corporation. These crystals have a (-2 0 1) surface orientation, with [0 1 0] and [1 0 2] edges. (Due to the monoclinic structure, the vectors that are normal to the (-2 0 1) surface are along the [-1 0 2] and [1 0 -2] directions. These samples have a thickness of 0.7 mm and a carrier density between $(1.1–1.7)x10^{18}$ cm^{-3}, presumably from Sn dopants that were intentionally introduced into the sample during its growth.

To introduce hydrogen or deuterium, the samples were sealed in quartz ampoules filled with H_2 or D_2 gas (2/3 atm at room temperature) and annealed at elevated temperatures in a tube furnace. These anneals were terminated by quenching the sample (contained in the ampoule) to room temperature in water.

Infrared absorption spectra were measured with a Bomem DA.3.16 Fourier transform spectrometer equipped with a globar source, a KBr beamsplitter, and an InSb detector. A wire-grid polarizer was placed in the IR beam between the cryostat and the detector to polarize the light. (The sample was mounted such that the electric field vector **E** was parallel to either the [0 1 0] axis or the [1 0 2] axis of the crystal.) Samples were cooled to either 10 or 77 K in an Air Products Helitran continuous-flow cryostat. To investigate the temperature dependences of the line shapes of the O-H and O-D vibrational lines introduced by the H_2 and D_2 treatments, the samples were cooled in a variable temperature Oxford CF1204 cryostat using either liquid He or N_2 as the cryogen.

A 3.0 μm (3333 cm^{-1}) low-pass filter was used to limit the spectral range of the O-D measurements to increase their signal-to-noise (S/N) ratio.

Heat treatments to determine the thermal stability and reactions of the hydrogen-containing centers were performed at successively increasing temperatures. The anneals lasted 30 minutes and were performed in either flowing N_2 (≤ 1000 °C) or in air (> 1000 °C); the samples were quenched to room temperature in water to terminate the anneals or were allowed to cool on a metal plate outside the furnace.

5.3: Experimental Results

5.3.1: Hydrogenation Treatments

Figure 5.3.1 shows the IR-absorbance spectra (at 77 K) of β–Ga_2O_3 single crystals in their as-grown state and after hydrogenation at 800 or 900 °C for 1 hour. The left panel shows the broad absorption due to free carriers. Individual spectra were corrected by subtracting a polynomial function from the absorbance to produce a flat baseline between 3400 and 3650 cm^{-1}; these regions are shown in the right panel. The as-grown crystal showed free carrier absorption, but no O-H vibrational lines. Samples that were hydrogenated at 800 or 900 °C for 1 hour showed a strong vibrational line with a frequency (at 77 K) of 3437.02 cm^{-1}. The integrated absorbance of this line for a sample prepared at 900 °C was ~1.5 times stronger than the integrated absorbance of this line for a sample prepared at 800 °C. In both hydrogenation treatments, the free-carrier absorption remained unchanged (within error) relative to the as-grown sample, which indicates that the defect responsible for the 3437 cm^{-1} line does not produce a substantial concentration of free electrons. A more quantitative set of free-carrier measurements will be presented in Section 5.3.5, which confirms this result. The free-carrier absorption in these crystals could arise from the Sn dopants that were intentionally introduced during crystal growth or from another defect (perhaps Si) that is not detected in our absorbance spectra. With our limited number of samples, however, it was not possible to determine the origin of this free-carrier absorption in more detail.

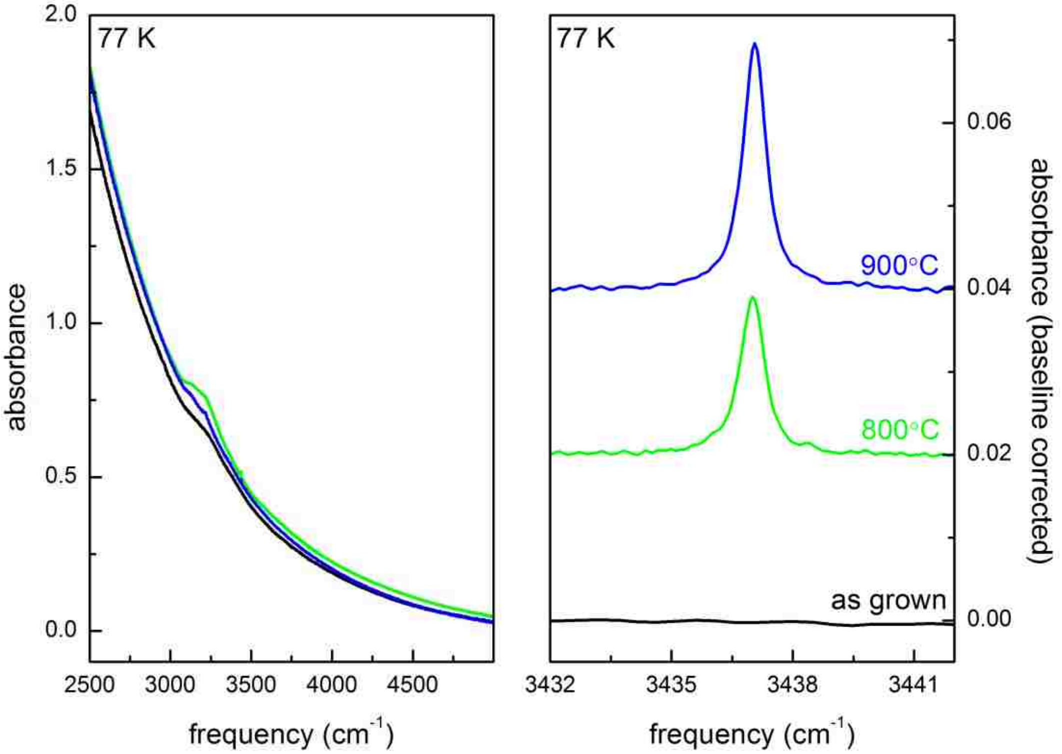

[redacted]

5.3.2: Isotope Shifts

Figure 5.3.2 shows the polarized IR absorbance spectra for two β–Ga_2O_3 samples: one sample was deuterated at 800 °C for 1 hour, and the other was hydrogenated at 900 °C for 1 hour. The treatments were terminated by quenching the samples to room temperature in water. The D_2 treatment resulted in the appearance of a vibrational line with a frequency of 2546.43 cm^{-1}, and the H_2 treatment produced the 3437.02 cm^{-1} line that was discussed in Section 5.3.1.

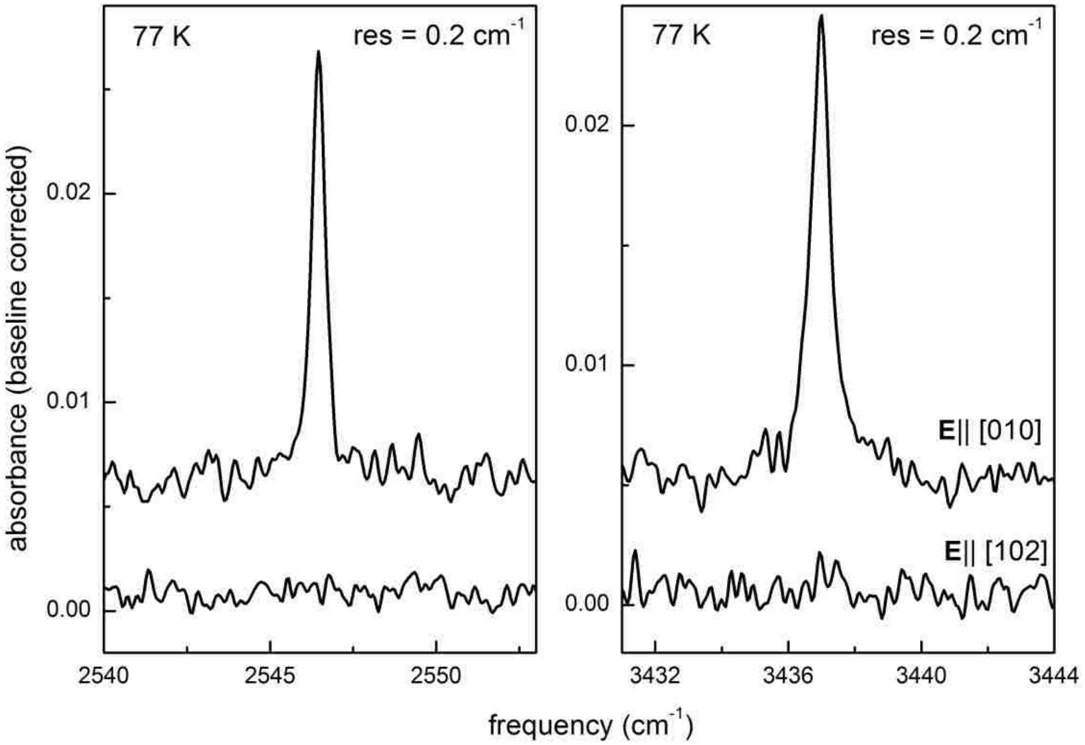

[redacted]

The ratio of the frequency of the vibrational line in the hydrogenated sample to the frequency of the vibrational line in the deuterated sample, $r = \omega_H/\omega_D$, is 1.350, which is close to the value of 1.37 determined in Chapter 2 for a harmonic oscillator consisting of oxygen and hydrogen. Therefore, the LVMs shown in Fig. 5.3.2 are likely to be the stretching modes of an O-H defect.

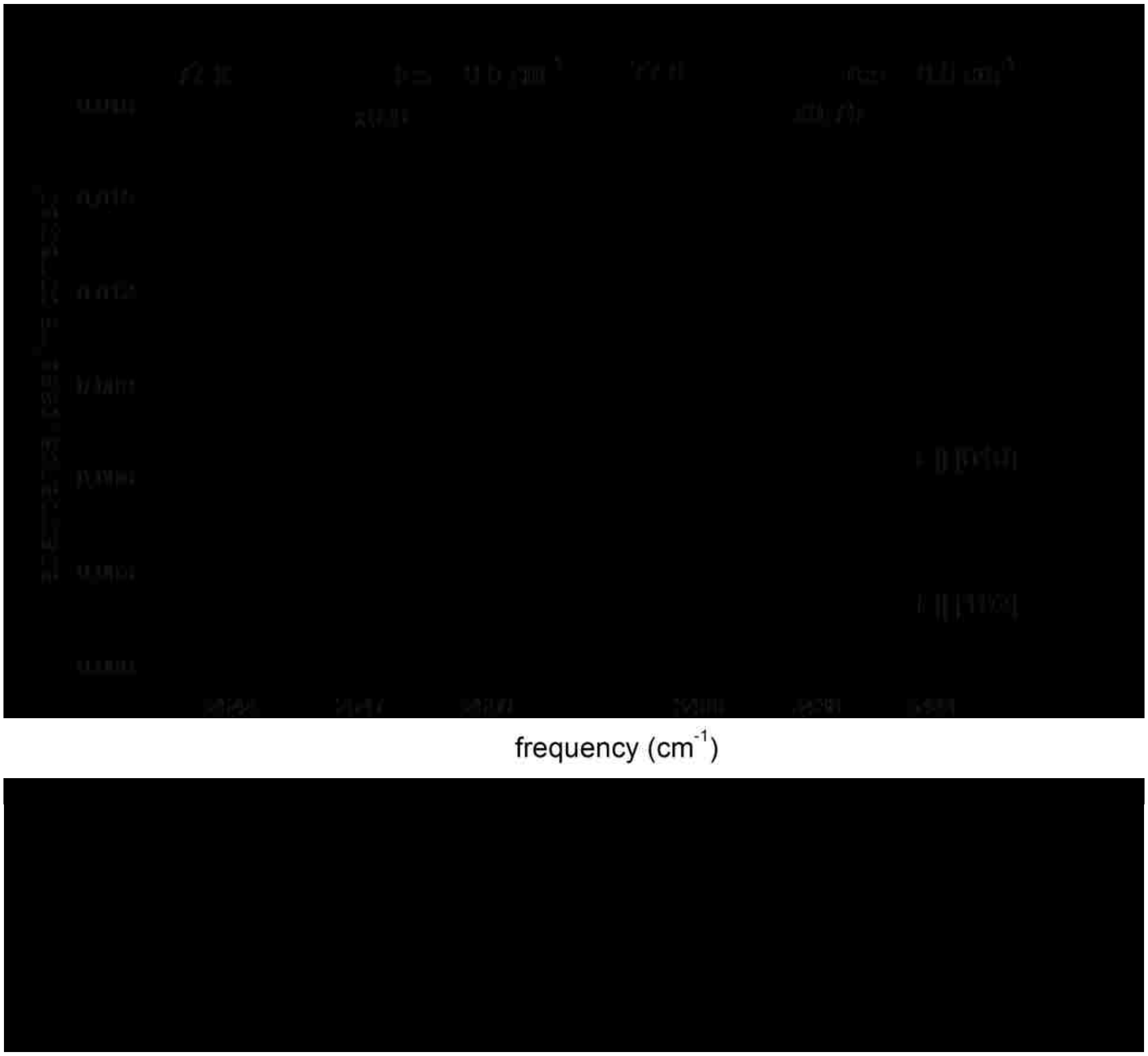

Information about the number of hydrogen atoms contained in a defect can be obtained by co-doping a sample with hydrogen and deuterium. Figure 5.3.3 shows the polarized IR absorbance spectra at 77 K for a $\beta{-}Ga_2O_3$ single crystal that was treated in a 1:1 H_2:D_2 gas mixture. The absorbance spectra for **E**||[0 1 0] for the H- and D-treated samples from Fig. 5.3.2 are shown as dashed lines in the same panel as the spectra for the

H_2+D_2 co-doped sample. In addition to the 3437.02 cm^{-1} and 2546.43 cm^{-1} lines, the H_2+D_2 treatment produced two new lines with frequencies of 3438.16 cm^{-1} and 2547.11 cm^{-1}. These new H and D lines also have a frequency ratio *r* = 1.350, which confirms that they are due to an O-H-containing defect. To confirm that the new lines arise from co-doping hydrogen and deuterium into the same sample, a second β−Ga_2O_3 sample was treated in a ~1:3 H_2:D_2 gas mixture.

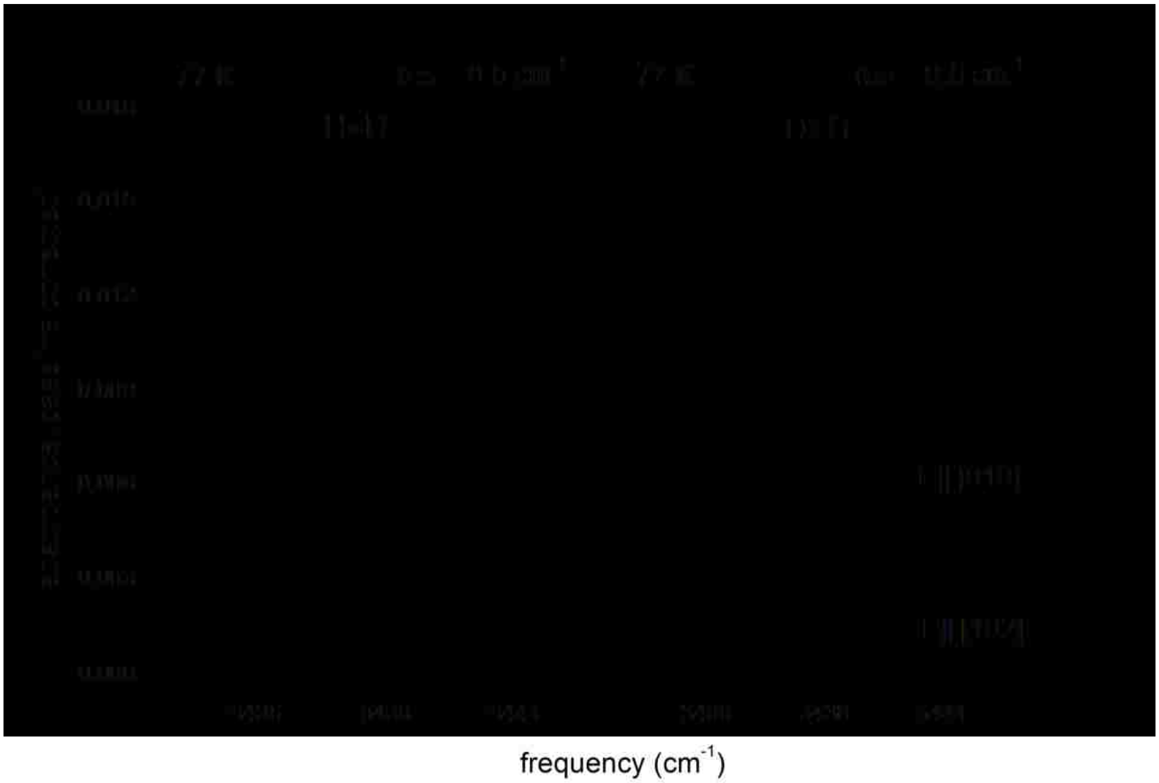

[redacted]

Polarized absorbance spectra for the O-H stretching region of these samples are shown in Fig. 5.3.4. (Spectral information in the O-D stretching region for the β−Ga_2O_3 sample that was treated in the ~1:3 H_2:D_2 mixture is unavailable because it was obscured by stronger free-carrier absorption than the sample treated in the 1:1 H_2:D_2 mixture). The intensity of the 3438 cm^{-1} line relative to the 3437 cm^{-1} line is depended on the H_2:D_2 ratio of the gas mixture. As the amount of D_2 gas in the mixture was increased relative to the amount of H_2 gas, the intensity of the 3438 cm^{-1} line increased relative to the intensity of the 3437 cm^{-1} line. The presence of two additional LVMs in the H+D treated samples and the dependence of the relative intensity of these LVMs on the H_2:D_2 concentration in the gas mixture show that these LVMs arise from a defect containing two hydrogen atoms.

If the two hydrogen atoms were inequivalent, as was observed in ZnO,[25] one would expect to observe *two* O-H LVMs in a sample treated in pure H_2, *two* O-D LVMs in a sample treated in pure D_2, and *four* additional LVMs in a sample treated in the H_2+D_2 mixture. Since one O-H and one O-D LVM are observed in the samples treated in pure H_2 and D_2, respectively, and only two additional LVMs are observed in the samples treated in a H_2+D_2 mixture, these LVMs must arise from a defect containing *two equivalent* hydrogens.

5.3.3: Polarization Dependence

The bulk $\beta-Ga_2O_3$ crystals from MTI Corporation have a (-2 0 1) surface with edge orientations along the [0 1 0] and [1 0 2] directions. Figures 5.3.2 – 5.3.4 reveal another interesting feature of the 3437.0/2546.4 cm^{-1} and the 3438.2/2547.1 cm^{-1} lines. At normal incidence of the IR beam on the (-2 0 1) sample surface, the vibrational lines were completely polarized along the [0 1 0] axis of the crystal. Thus, the transition dipole moment of the defect lies in the plane containing the [0 1 0] axis and the direction that is normal to the (-2 0 1) plane.

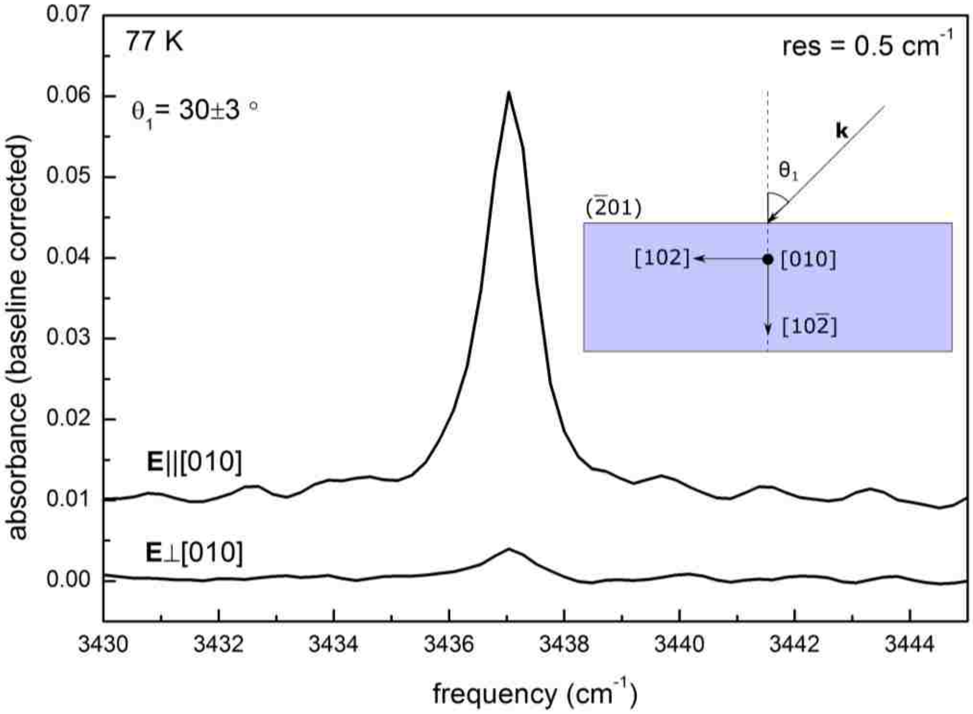

[redacted]

Figure 5.3.5 shows the absorbance spectra of the 3437 cm^{-1} line for **E**∥[0 1 0] and **E**⊥[0 1 0] with the sample rotated about the [0 1 0] axis by 30±3° clockwise from normal incidence on the (-2 0 1) surface. If the transition moment of the defect was aligned parallel to the [0 1 0] axis, the 3437 cm^{-1} line would show no component in the absorbance spectrum for **E**⊥[0 1 0]. As is evident in the figure, there is a small component present in the spectrum for **E**⊥[0 1 0]. Consequently, the transition moment of the defect must be angled between the [0 1 0] direction and the direction perpendicular to the (-2 0 1) plane. The integrated absorbances of the 3437 cm^{-1} line for the projections along **E**∥[0 1 0] and **E**⊥[0 1 0] are (78±2)x10^{-3} and (6.2±0.3)x10^{-3} cm^{-1}, respectively.

Determining the transition-moment angle of the 3437 cm^{-1} O-H line is complicated by the monoclinic symmetry of $\beta-Ga_2O_3$. The complex dielectric tensor of this crystal has the form,

$$\bar{\bar{\varepsilon}} = \begin{pmatrix} \tilde{\varepsilon}_{xx} & 0 & \tilde{\varepsilon}_{xz} \\ 0 & \tilde{\varepsilon}_{yy} & 0 \\ \tilde{\varepsilon}_{xz} & 0 & \tilde{\varepsilon}_{zz} \end{pmatrix}, \qquad \textbf{Eq. 5.3.1}$$

where x is parallel to the ***a*** axis, y is parallel to the ***b*** axis (the symmetry axis of the crystal), and z is parallel to the $\boldsymbol{c}^*$ axis, where $\hat{e}_z = \hat{e}_x \times \hat{e}_y$. One would need to determine the tensor representations for the 3437 cm^{-1} O-H line and the refracted, polarized light with respect to the main dielectric axes of the crystal. The angle of the transition moment with respect to the [0 1 0] axis, θ_d, can be determined by matching the absorption coefficients for the refracted light on the O-H dipole with the absorption coefficients of the 3437 cm^{-1} line determined from experiment.

Several studies[26–28] have found that in the IR spectral region, the imaginary components of the dielectric tensor are negligible and the off-diagonal elements of the real components of the dieletric tensor have values such that ε_{xz}~0.02 << ε_{xx}, ε_{yy}, and ε_{zz}~3.5-3.6. Thus, for a first approximation, the ***a***, ***b***, and $\boldsymbol{c}^*$ axes are the dielectric axes of the crystal. In the transparent spectral region and for $\lambda = 4.0$ μm, $\varepsilon_{xx} \sim 3.48$ and $\varepsilon_{zz} \sim 3.58$, which gives a difference in the refractive indices along the ***a*** and $\boldsymbol{c}^*$ axes of ~0.02 refractive index units. Consequently, the difference in the projection angle of the refracted light inside the crystal is ~0.2°. This difference is small enough to model $\beta-Ga_2O_3$ as an isotropic medium for the polarization analysis.

The angle of the transition moment with respect to the [0 1 0] axis, θ_d, can be determined from the projections of the O-H transition moment onto the directions that are parallel and perpendicular to the [0 1 0] axis and from Snell's law. The ratio of the intensity of light polarized perpendicular to the [0 1 0] axis to the intensity of light polarized parallel to the [0 1 0] axis is given by,

$$\frac{I_{\perp[010]}}{I_{\parallel[010]}} = \frac{\sin^2\theta_d \sin^2\varphi_2}{\cos^2\theta_d} = \tan^2\theta_d \sin^2\varphi_2\,; \quad \varphi_2 = \sin^{-1}\left(\frac{n_1 \sin\varphi_1}{n_2}\right), \qquad \textbf{Eq. (5.3.1)}$$

where n_2 is the refractive index of the isotropic medium and φ_2 is the angle of refraction. The transmission moment angle, θ_d, can be determined using $n_1 = 1.0$ (vacuum), $n_2 = 1.88$ (average "isotropic" refractive index for $\beta\text{–}Ga_2O_3$), $\varphi_1 = 30\pm3°$, and the integrated absorbances of the 3437 cm^{-1} line polarized parallel and perpendicular to the [0 1 0] axis.

$$\frac{I_{\perp[010]}}{I_{\parallel[010]}} = \frac{(6.2 \pm 0.3)\times10^{-3}\text{cm}^{-1}}{(78.0 \pm 2.0)\times10^{-3}\text{cm}^{-1}} = \tan^2\theta_d \sin^2(15 \pm 6°) \qquad \textbf{Eq. (5.3.2)}$$

This analysis yields a transition moment angle with respect to the [0 1 0] axis of 47±11° for the 3437 cm^{-1} O-H defect.

5.3.4: Temperature Dependence

The temperature-dependent frequency shift and line-width broadening of several O-H LVMs in ZnO[29–32] have been analyzed using the theory developed by Persson and Ryberg.[33] In their model, a LVM is coupled anharmonically with an exchange mode of energy E_0 through a parameter $\delta\omega$. The exchange mode then interacts with the phonon modes of the crystal through a "friction" parameter η. In the weak-coupling limit, the frequency of the LVM as a function of temperature is given by,

$$\omega = \omega_0 + \frac{\delta\omega}{\exp(E_0/k_B T) - 1}. \qquad \textbf{Eq. (5.3.3)}$$

Its full-width-at-half-maximum (FWHM), Γ, as a function of temperature is given by,

$$\Gamma = \frac{2(\delta\omega)^2}{\eta}\left(\frac{1}{2} + \frac{1}{\exp(E_0/k_B T) - 1}\right)^2. \qquad \textbf{Eq. (5.3.4)}$$

Figure 5.3.6 shows absorbance spectra for the 3437 and 2546 cm^{-1} lines at temperatures of 10, 100, 175, and 250 K. As the temperature of the sample increases, the lines broaden and shift to lower frequencies.

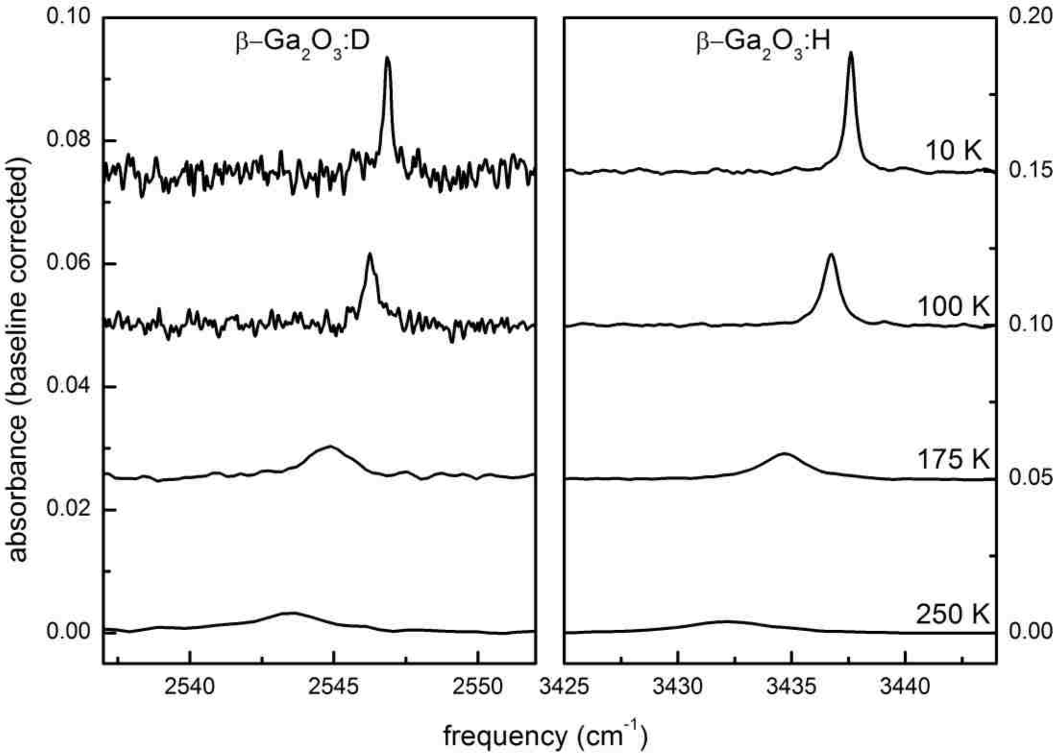

[redacted]

The shapes of the 3437 and 2546 cm^{-1} lines were fit using the curve-fitting software Thermo Grams Scientific PeakFit. Both of the lines are fit well with Lorentzian line shapes at all temperatures. Figure 5.3.7 shows the temperature dependences of ω and Γ between 10 and 293 K for the 3437 and 2546 cm^{-1} lines. The data for each isotope were fit with Eqs. (5.3.3) and (5.3.4) by adjusting three fit parameters: E_0, $\delta\omega$, and η. These fit parameters for the 3437 and 2546 cm^{-1} lines and their uncertainties, determined from the scatter of the data, are listed in Table 5.3.1.

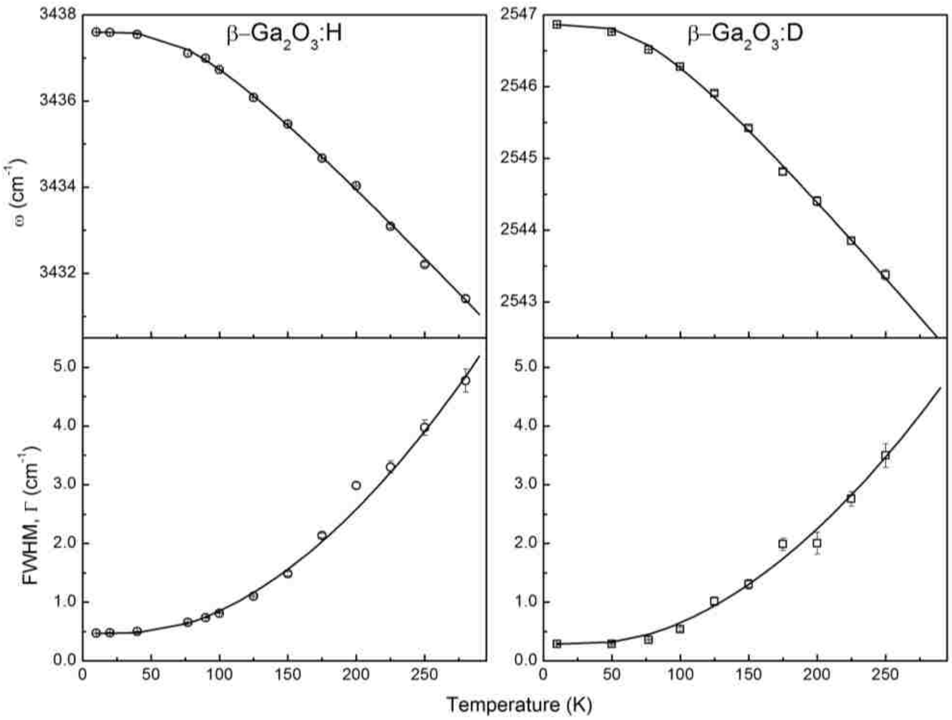

[redacted]

The energy of the exchange mode is small (< 200 cm^{-1}) and independent of the hydrogen isotope, which suggests that the same exchange mode, involving the motion of the host atoms, is coupled with the defects. The values of E_0 and $\delta\omega$, ~160 cm^{-1} and ~ 7 cm^{-1}, respectively, are similar for both the O-H and O-D defects.

Schubert *et al.*[28] have determined the energies of various phonon modes in $\beta-Ga_2O_3$. Phonons for both transverse and longitudinal optic modes have frequencies of 155 cm^{-1}, which are similar to the values of E_0 determined from the fits. The magnitude of $\delta\omega$ determined for several O-H LVMs in ZnO[29–32] to which the Persson-Ryberg model has been successfully applied is ~10 cm^{-1}. The values of $\delta\omega$ (~7 cm^{-1}) from the fits to our $\beta-Ga_2O_3$ data are of the same order.

Table 5.3.1: Fit parameters for the Persson fits to the LVM temperature dependence of the 3437.1 and 2546.5 cm^{-1} O-H and O-D LVMs measured at 77 K.

Fit Parameter	2546.1 cm^{-1}(O-D)	3437.1 cm^{-1}(O-H)
E_0 [cm^{-1}]	157 ± 13	162 ± 5
$\delta\nu$ [cm^{-1}]	–5.2 ± 0.4	–8.1 ± 0.4
η [cm^{-1}]	9.7 ± 0.4	20.1 ± 0.4

Although the fits to the temperature dependences of ω and Γ are in good agreement with the data, $\delta\omega$ and η for both the 3437 and 2546 cm^{-1} lines do not satisfy the weak-coupling condition, $\delta\omega << \eta$. The disagreement is worse for the 2546 cm^{-1} line (5.2 < 9.7 cm^{-1}) than for the 3437 cm^{-1} line (8.1 < 20.1 cm^{-1}). Thus, the anharmonic interaction between a LVM and a single-exchange mode may not be a good model for the temperature dependence of the data. A similar observation was reported recently by Herklotz and coworkers[34] for the temperature dependence of the O-H and O-D LVMs of a complex involving three equivalent hydrogen atoms in hydrothermal ZnO. Because the temperature dependence of the LVM line shape does not affect the interpretation of the data from other experiments, e.g., isotope exchange, polarization, and thermal stability, other models for the temperature dependences of the line frequencies and widths are not considered here.

5.3.5: Thermal Stability

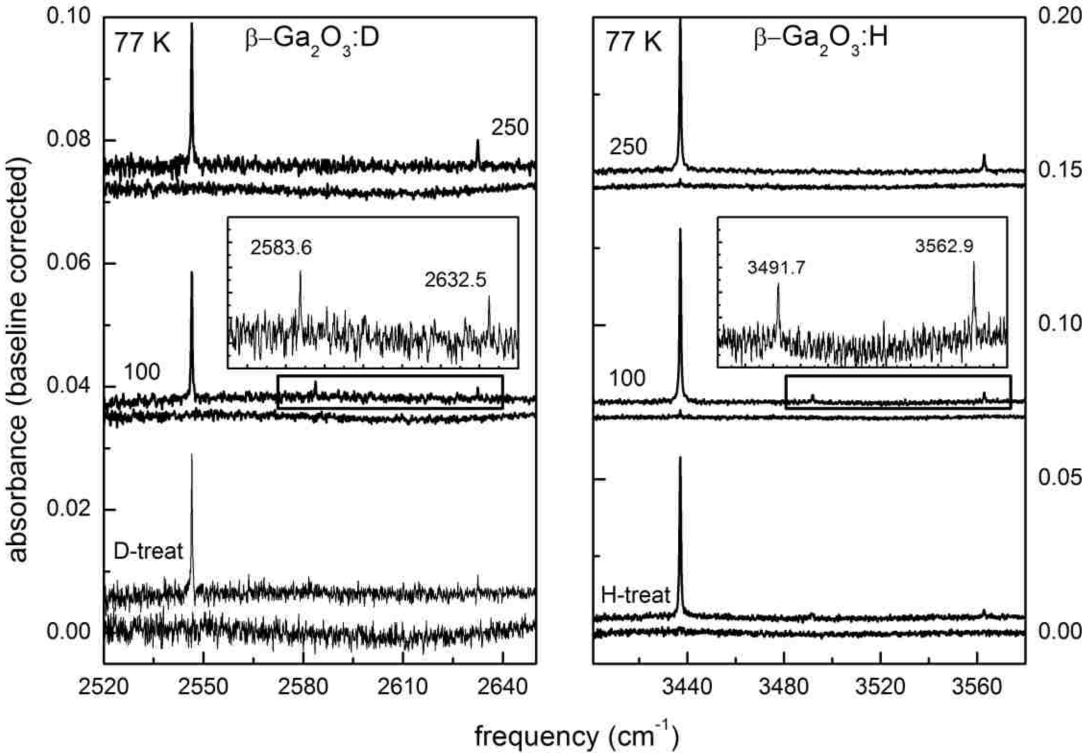

[redacted]

A series of annealing experiments was performed to investigate the stabilities of the defects responsible for the 3437 and 2546 cm^{-1} vibrational lines. Figure 5.3.8 shows a selection of polarized IR-absorbance spectra for $\beta-Ga_2O_3$ samples that were deuterated or hydrogenated at 900 °C and subsequently annealed in N_2 gas for 30 minutes at temperatures of 100 and 250 °C. The $H_2(D_2)$-treated samples also show two weak lines with frequencies at 77 K of 3491.7(2583.6) cm^{-1} and 3562.9(2632.5) cm^{-1}; samples that were hydrogenated or deuterated at 800 °C did not show these lines. The *r* values for these two pairs of lines are 3491.7/2583.6 = 1.351 and 3562.9/2632.5 = 1.353, respectively, which confirms that they are vibrational modes of O-H containing defects. The weaker line at 3491.7(2583.6) cm^{-1} annealed away at 200 °C. On the other hand, the 3562.9(2632.5) cm^{-1} line increased in strength after the 200 °C anneal but annealed away at 500 °C. The different thermal stabilities of the 3491.7(2583.6) cm^{-1} and 3562.9(2632.5) cm^{-1} lines show that these vibrational lines arise from two different H-containing defects. These new vibrational lines have the same polarization properties as the 3437/2546 cm^{-1} lines, i.e., they are completely polarized for $\mathbf{E}\|[0\ 1\ 0]$ and have no component for $\mathbf{E}\|[1\ 0\ 2]$. Thus, the transition moments of these defects must also lie in the plane containing the [0 1 0] and the direction that is normal to the (-2 0 1) plane.

Figure 5.3.9 shows the IR absorbance spectra for hydrogenated $\beta-Ga_2O_3$ (H_2 900 °C, 1 hour) that was subsequently annealed in an inert N_2 ambient at successively higher temperatures between 100 and 1,000 °C. As is evident in the figure, the 3437 cm^{-1} line shows a high thermal stability and was still present after the 1,000 °C anneal. The integrated absorbance of the peak remained relatively constant except after anneals at 400 and 700 °C, where it increases by ~20 %. The strength of the 3437 cm^{-1} line decreases after the 900 °C anneal and remains at that strength following the 1,000 °C anneal. In addition, a weak line at 3467.8 cm^{-1} appeared after the 900 °C anneal and maintained the same intensity after the 1,000 °C anneal.

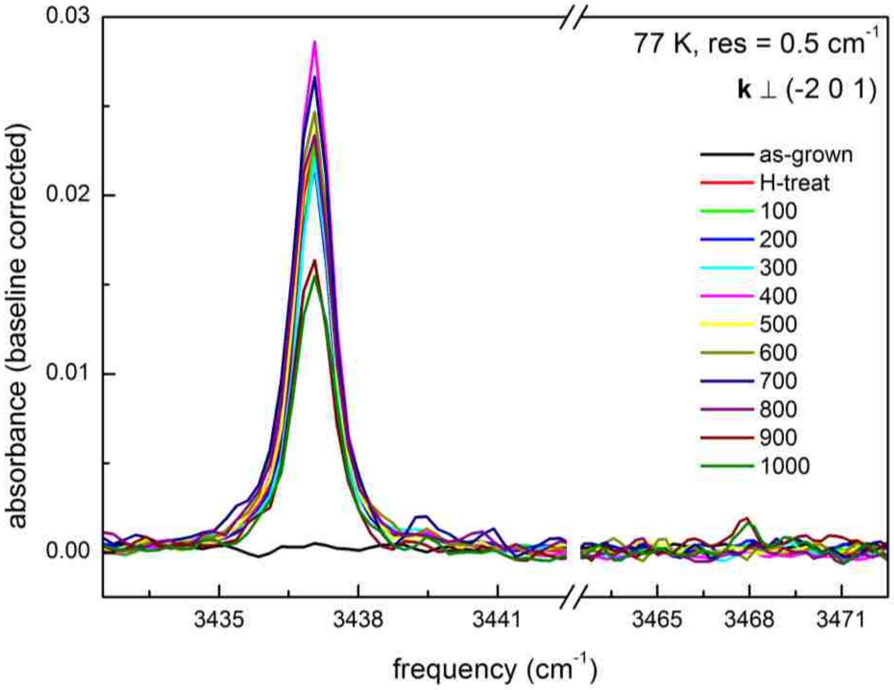

[redacted]

The furnace used to anneal samples in inert N_2 gas is limited to a maximum temperature of 1000 °C. A second furnace in our lab is capable of reaching temperatures up to 1500 °C, but the anneals are performed in open air. The hydrogenated $\beta-Ga_2O_3$ sample described above was also annealed at 1050 °C in air for 30 minutes and then quenched to room temperature in water. The polarized IR-absorbance spectra after this anneal are shown in Fig. 5.3.10.

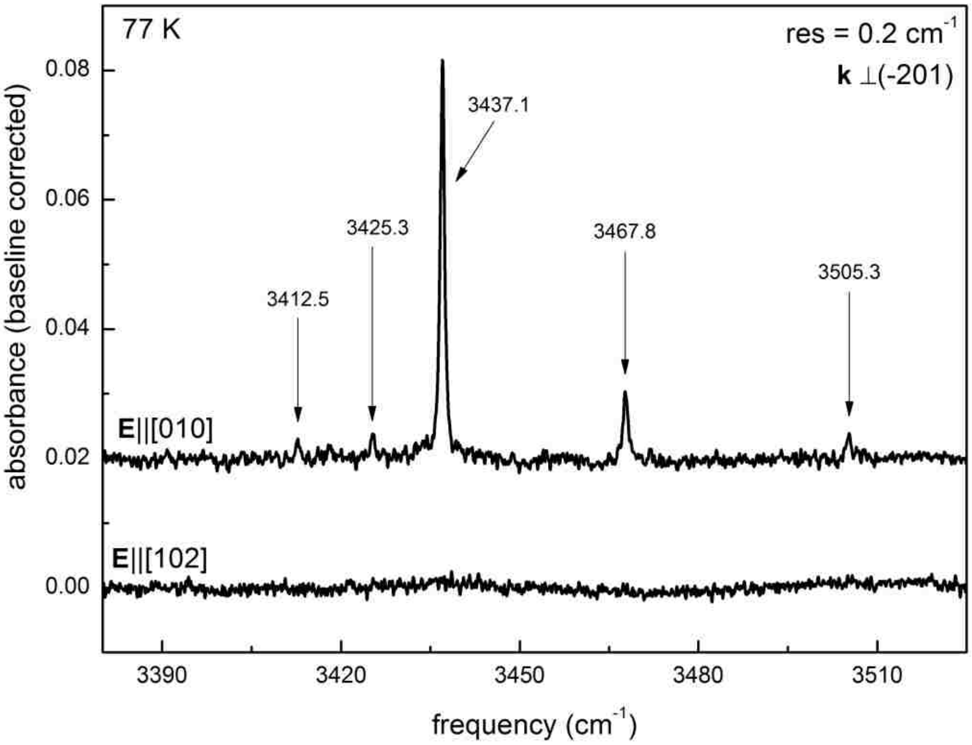

[redacted]

The 1050 °C anneal returned the 3437 cm^{-1} line back to its as-grown strength, increased the strength of the 3467.8 cm^{-1} line, and produced three additional weak vibrational lines with frequencies at 77 K of 3412.5, 3425.3, and 3505.3 cm^{-1}. These lines also showed the same polarization properties as the other O-H lines, i.e., they were completely polarized for **E**||[0 1 0]. The simultaneous increases in the strengths of the 3437.0 and the 3467.8 cm^{-1} lines suggests that there may be another source of hydrogen available to the sample. However, it is difficult to identify this source of the hydrogen based solely on these results.

Another $\beta-Ga_2O_3$ sample, cut from the same bulk piece as the sample used for the H-isochronal-annealing experiments, was deuterated (D_2 800 °C, 1 hour) and annealed in an inert N_2 ambient at successively higher temperatures to examine the thermal stability of the defect responsible for the 2546 cm^{-1} line. Prior to the deuteration, both sample surfaces were polished to optical quality using diamond paste, which permits quantitative measurements of free-carrier absorption. Figure 5.3.11 shows the IR absorbance spectra of this deuterated $\beta-Ga_2O_3$ sample after the D-treatment and after each anneal.

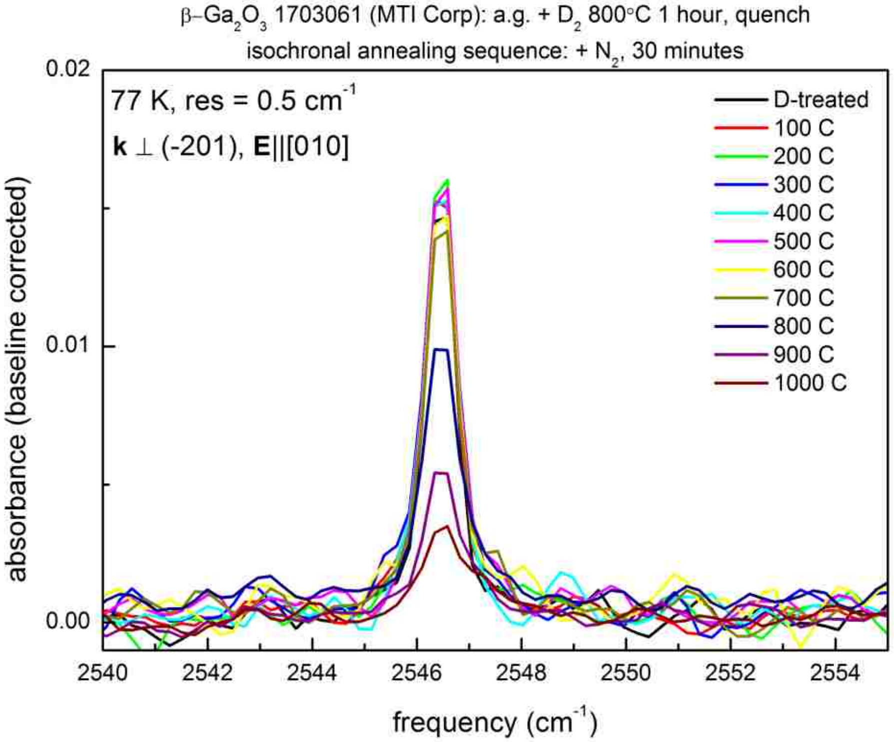

[redacted]

The intensity of the 2546 cm^{-1} line was unaffected by anneals up to 700 °C and, within error, remained constant. The 800, 900, and 1000 °C anneals significantly decrease the strength of the 2546 cm^{-1} line. Only 20% of the integrated absorbance remained after the 1000 °C anneal as compared to the value immediately after deuteration. The free-carrier absorbance spectra measured at 77 K, shown in Fig. 5.3.12, showed no significant changes during the annealing sequence.

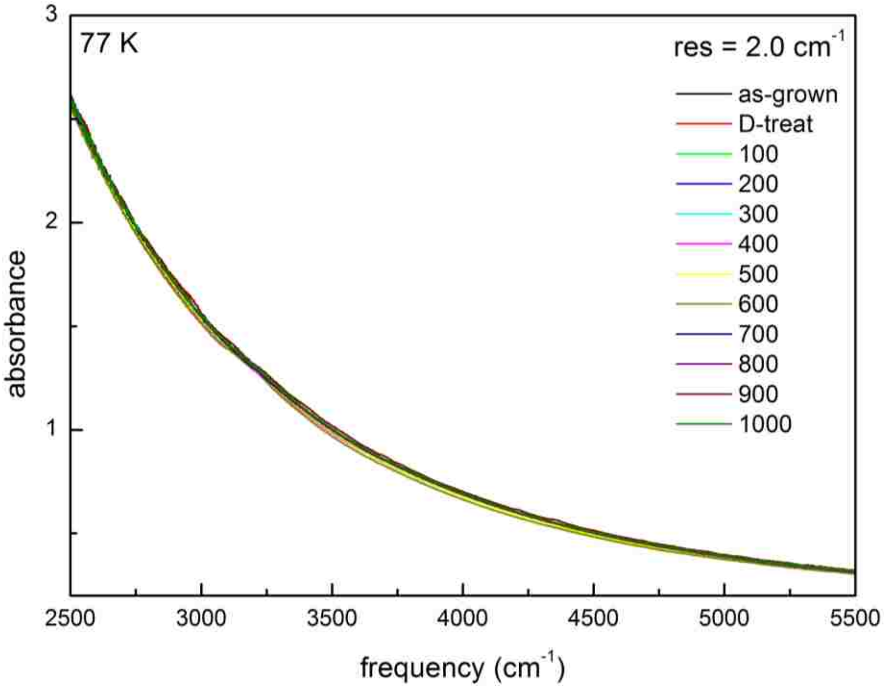

[redacted]

If the O-H and O-D defects that contribute to the 3437 and 2546 cm^{-1} lines, respectively, are uniformly distributed throughout the same region of the sample, then one might expect that the 3437 cm^{-1} O-H line should anneal away at a lower temperature than the 2546 cm^{-1} O-D line due to the heavier mass, and therefore smaller mobility, of D compared to H. The data presented in Figs. 5.3.9 and 5.3.11 show the opposite trend. The 2546 cm^{-1} O-D line begins to anneal away at 700-800 °C while the 3437 cm^{-1} O-H line appears to be stable for anneals up to 1050 °C. A careful inspection of the absorbance spectra in Fig. 5.3.11 for anneals at 800 °C and above reveals a weak signature of the 2547 cm^{-1} line seen in the H+D co-doped sample, which suggests the presence of hydrogen in the deuterated sample.

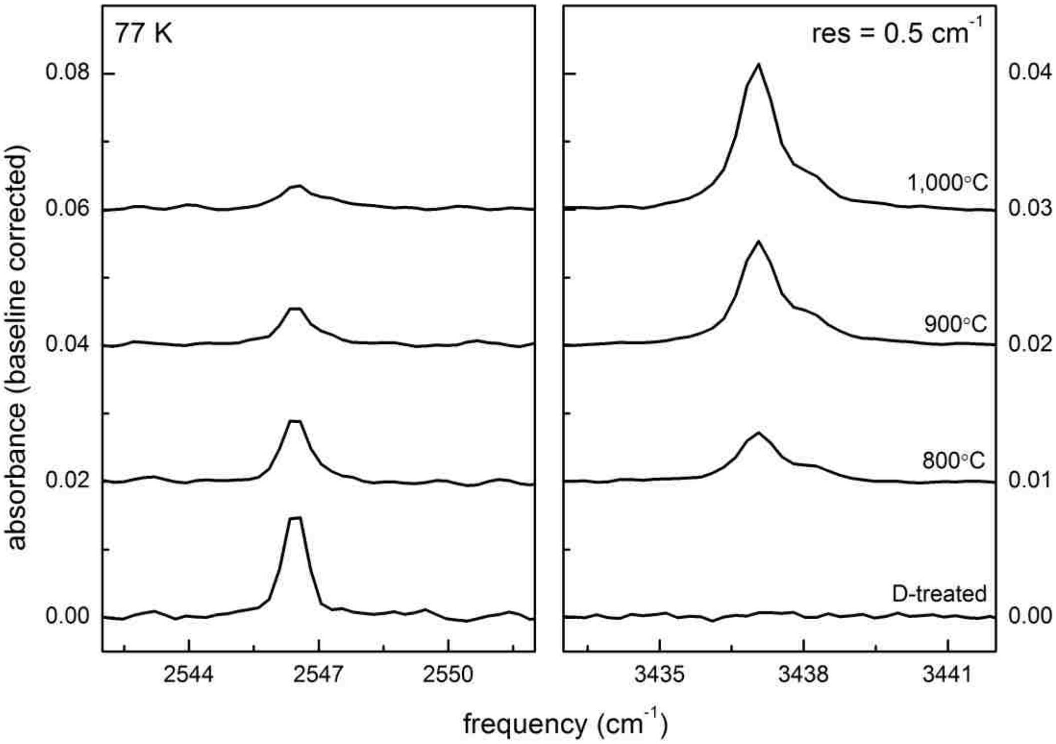

[redacted]

For anneals between 800 and 1000 °C, the absorbance spectra were also measured in the O-H spectral region. Figure 5.3.13 shows both the O-D and O-H stretching regions of the deuterated sample immediately after deuteration and after anneals at 800, 900, and 1000 °C. Only the 2546 cm^{-1} line was present after the sample is deuterated, and there are no signatures of any of the O-H lines that were observed during the O-H isochronal anneals. After the 800 °C anneal, however, both the 3437 and the 3438 cm^{-1} lines were present in the O-H stretching region. The 900 °C anneal increased the strength of both of these lines by a factor of 2. The 1000 °C anneal increased the strength of the 3437 cm^{-1} line by an additional factor of 2 while the strength of the 3438 cm^{-1} line remained unchanged. Since no O-H vibrational lines were initially present in the deuterated sample, these results suggest that hydrogen is present in the *as-grown* sample in a form that is not observed by IR spectroscopy. Presumably, these hydrogen-containing complexes dissociate during the high temperature anneals and act as a source of hydrogen for the O-H lines seen in Fig. 5.3.13. A discussion of the possible identities of the spectroscopically transparent hydrogen will be presented in Section 5.5.

The presence of hydrogen in the as-grown sample can explain the discrepancy in the apparently greater thermal stability of the 3437 cm^{-1} O-H line relative to the 2546 cm^{-1} O-D line. In the hydrogenated $\beta-Ga_2O_3$ sample, anneals between 700 and 1000 °C might dissociate the hydrogen complex not observed by IR spectroscopy, providing a source of hydrogen to form the defect that gives rise to the 3437 cm^{-1} line. Thus, the change in the intensity of the 3437 cm^{-1} line at each temperature is determined by the loss of defect population due to annealing and the gain in defect population due to the dissociation of the hydrogen complex not observed by IR spectroscopy. The monatonic increase in the strength of the 3437 cm^{-1} line in the deuterated $\beta-Ga_2O_3$ sample after anneals at 800, 900, and 1000 °C suggests that hydrogen is being released during these anneals. This hypothesis could be confirmed by annealing an as-grown piece of $\beta-Ga_2O_3$, cut from the same bulk crystal as the one used for the O-H and O-D isochronal annealing experiments above, at high temperatures in an inert ambient. If O-H vibrational lines are produced by the anneals, then the only source of hydrogen during the anneal is the sample itself.

A homogeneous distribution of H and D throughout the $\beta-Ga_2O_3$ sample should result in a statistical ratio of the intensities of the D-D:H-D:H-H lines of 1:2:1. The spectra in Fig. 5.3.13 do not follow this trend, as the strengths of both the 3437 and 2546 cm^{-1} H-H and D-D lines are greater than the strength of the mixed H-D lines at 3438 and 2547 cm^{-1}. This result implies that H and D are not distributed uniformly throughout the same region of the bulk crystal. Preliminary experiments (not shown) in which a hydrogenated sample was successively thinned showed that the strength of the 3437 cm^{-1} line decreased by a factor of two (compared to the hydrogenated sample) after 0.10 mm of material was removed from one surface of the sample. This result implies that the O-H and O-D defects that give rise to the 3437 and 2546 cm^{-1} lines are not distributed throughout the bulk and are only located in layers near the surface of the material. The source of the hydrogen present in the as-grown sample might be distributed throughout the bulk of the sample. Thus, the inhomogeneous distribution of H and D in the sample can account for the fact that the observed ratios of intensities of the H-H:H-D:D-D lines do not follow simple statistics.

5.4: Computational Results: Microscopic Structures of H Defects in $\beta-Ga_2O_3$

Professor W. Beall Fowler has used CRYSTAL06[35] to study different microscopic structures and their relative formation energies for hydrogen-related defects in $\beta-Ga_2O_3$. These first-principles calculations employed Gaussian basis functions and used density functional theory (DFT) with B3LYP exchange-correlation. These calculations used 80 atom supercells for the host $\beta-Ga_2O_3$ lattice plus the hydrogen atoms. The two inequivalent Ga sites and the three inequivalent O sites present many possibilities for defect structures.

The experimental results discussed in the preceding section provide several constraints on potential hydrogen-related defect structures. The defect giving rise to the 3437(2546) cm^{-1} line is composed of two equivalent hydrogen (deuterium) atoms. A defect involving two equivalent atoms bonded to a central atom can give rise to two types of stretching modes: symmetric and antisymmetric. Only one IR line is seen when a single isotope is present in the sample, which implies that only one of these stretch modes has a non-zero change in its electric dipole moment. The polarization results also force the direction of the transition moment for that mode to only have components perpendicular to the (-2 0 1) plane and parallel to the [0 1 0] axis.

Figure 5.4.1 shows the structures of two potential H_i sites (shown in blue) at O(1) (red) and O(2) (yellow) in $\beta-Ga_2O_3$. The direction of the incident light in the experiments and the crystalline axes that the light is polarized along are shown in the figure. For both types of H_i defects, the net electric dipole moments of the hydrogen stretching modes (symmetric or antisymmetric) have components along the [1 0 2] direction and no components along the [0 1 0] direction. The non-zero [1 0 2] component and the lack of a [0 1 0] component eliminate both H_i structures as candidates for the 3437 cm^{-1} line.

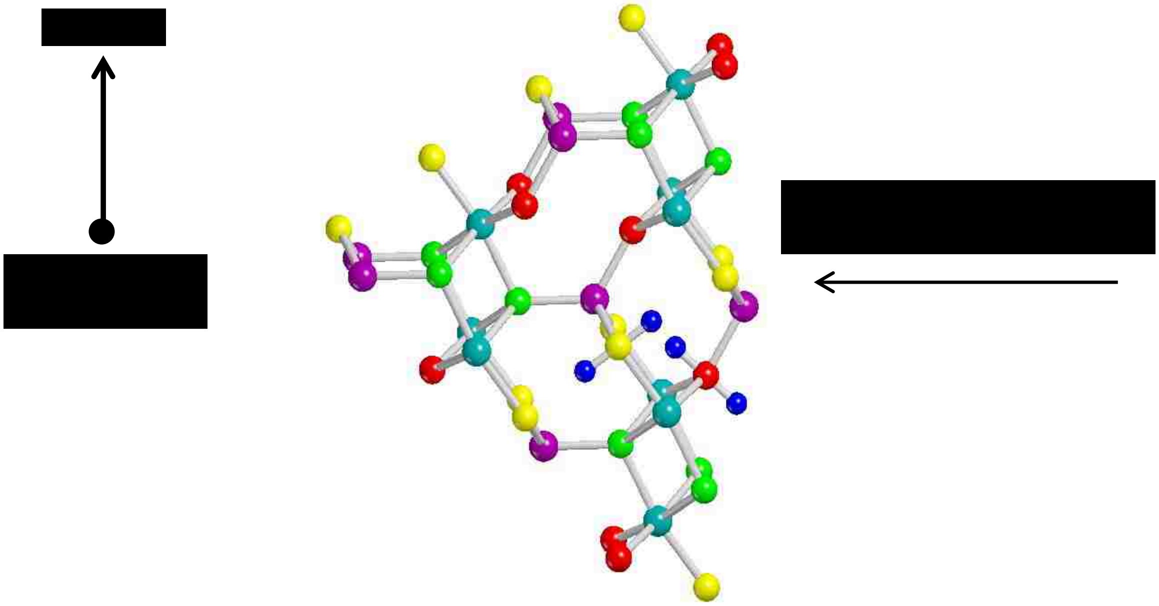

[redacted]

First-principles calculations by Varley and coworkers[23] predicted that hydrogenated gallium vacancies have lower formation energies than isolated gallium vacancies. They found that a vacancy at a tetrahedrally coordinated Ga(1) is energetically preferable to a vacancy at an octahedrally coordinated Ga(2). In addition, the Ga(1) vacancy ($V_{Ga(1)}$) can achieve a lower energy configuration by shifting towards its neighboring Ga(1) site. The structures shown in Fig. 5.4.2 show this shift. Figure 5.4.2(a) shows the perfect $\beta-Ga_2O_3$ crystal, Fig. 5.4.2(b) highlights both the $V_{Ga(1)}$ and the neighboring Ga(1) with dashed circles, and Fig. 5.4.2(c) shows the minimum energy configuration where the neighboring Ga(1) atom shifts to a site that is midway between the two "normal" Ga(1) sites. Professor Fowler's calculations reproduce this behavior, and ongoing calculations will confirm whether the shifted $V_{Ga(1)}$ is energetically preferable in the presence of hydrogen. That is, is a $V_{Ga(1)}$-H complex with a shifted $V_{Ga(1)}$ still lower in energy than the same type of complex with an unshifted $V_{Ga(1)}$? These calculations require a larger supercell (120 atoms instead of 80 atoms) to mitigate the effects of interactions between neighboring supercells.

[redacted] [redacted] [redacted]

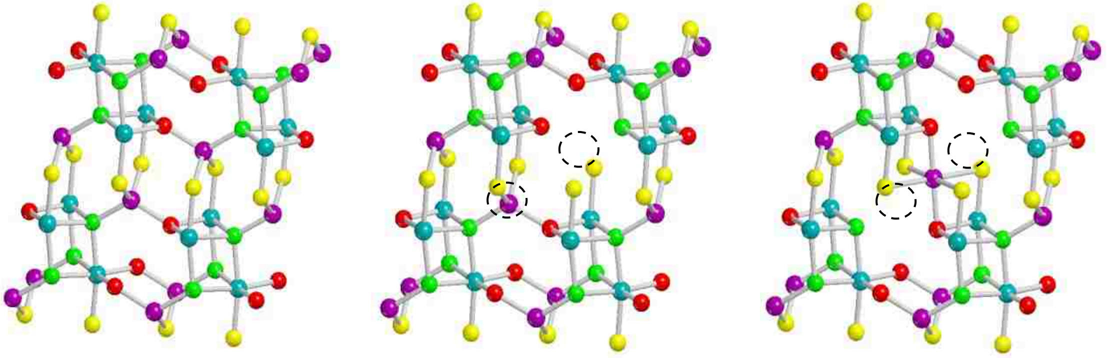

[redacted]

Figure 5.4.3(a) shows a possible configuration for the shifted $V_{Ga(1)}$ complexed with two hydrogen atoms that is consistent with the experimental data. The hydrogen atoms (shown in blue) are bonded to the O(2) atoms (yellow) on opposite sides of the shifted Ga(1) atom. Neither O-H bond has a component along the [1 0 2] direction, which is consistent with the results of the polarized-absorption experiments in Section 5.3.3.

Figures 5.4.3(b) and (c) show the displacements of the hydrogen atoms for the symmetric and antisymmetric stretching modes, respectively.

[redacted]

[redacted]

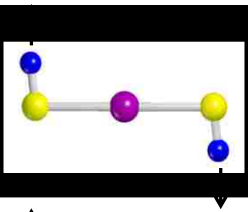

[redacted]

[redacted]

For this defect configuration, it is clear that the symmetric stretch has a net change in its electric dipole moment equal to zero, and the antisymmetric stretch has a non-zero change in its electric dipole moment. This result could potentially explain why only one vibrational line is seen for β–Ga_2O_3 samples containing a single isotope.

The $V_{Ga(1)}$-2H model presented in Fig. 5.4.3 is consistent with the experimental data, but it is possible that other energetically favorable configurations of this defect may exist. Although there are numerous defect complexes, e.g. $V_{Ga(2)}$-2H complex, V_{Ga} complexed with a single hydrogen, and interstitial Ga (Ga_i) complexed with hydrogen, which could also form, the common polarization properties of these lines suggest they *all* arise from the *same* general type of defect and not simply H_i.

5.5: Discussion

The progression of this discussion is as follows. First, the identity of the defect giving rise to the 3437/2546 cm^{-1} and the 3438/2547 cm^{-1} lines is discussed. Second, the nature of the other O-H and O-D lines seen after the 100, 250, and 1050 °C anneals is examined. Possible identities of the source of hydrogen in the as-grown samples are presented last.

Single crystals of β–Ga_2O_3 treated in pure H_2 (D_2) at 800 or 900 °C showed a single O-H (D) vibrational line with a frequency at 77 K of 3437 (2546) cm^{-1}. Two additional lines with frequencies of 3438 and 2547 cm^{-1} were observed for samples treated in a mixture of H_2 and D_2 gasses. The number of lines and the dependence of the relative intensities on the ratio of H_2 to D_2 gas in the ampoule during treatment suggest that these lines originate from a defect that contains two weakly coupled, *equivalent* hydrogen atoms. The polarized absorption data restrict the O-H bonds to have projections along the [0 1 0] axis and the direction perpendicular to the (-2 0 1) surface; no projection is permitted along the [1 0 2] axis. The observation of only one stretch mode for the H_2-(D_2-) treated samples implies that either the symmetric or the antisymmetric stretch mode has no change in its net electric dipole moment, which further restricts the orientation of the O-H (D) bonds. The electric dipole transition moment of the allowed stretch mode is at an angle of 47±11° with respect to the [0 1 0] axis. The isochronal annealing of the deuterated β–Ga_2O_3 sample shows that the 2546 cm^{-1} line begins to decay after annealing the sample at temperatures between 700-800 °C. The free-carrier absorption seen for the as-grown sample was unchanged after either hydrogenation or deuteration, and remained unchanged during the isochronal anneals.

The free-carrier absorption of the as-grown $\beta\text{–}Ga_2O_3$ sample is presumably due to the Sn donors incorporated during crystal growth. The Sn concentration, [Sn], in the as-grown samples was ~10^{18} cm^{-3}. A semi-quantitative estimate of the hydrogen concentration, [H], in a hydrogenated $\beta\text{–}Ga_2O_3$ sample is needed to understand whether the null change in the free-carrier absorption is due to the fact that the hydrogen-defects are not shallow donors, or due to the fact that [H] << [Sn]. If [H] << [Sn], then the contribution to the free carrier absorption by hydrogen should be negligible compared to the contribution by Sn. The relationship between the defect concentration and the integrated absorption coefficient of the vibrational line associated with that defect was given in Chapter 2 by Eq. (2.2.10),

$$N = \frac{\mu n c^2}{\pi q^2} \int \alpha(\sigma) d\sigma = A \int \alpha(\sigma) d\sigma, \qquad \textbf{Eq. (5.5.1)}$$

where $\alpha(\sigma)$ is the absorption coefficient at a particular wavenumber σ (reciprocal wavelength), μ is the reduced mass of the oscillator, *n* is the refractive index in the transparent spectral region, *c* is the speed of light (in cm/s), and *q* is the effective charge for the defect written in terms of CGS units ($e = 4.804\text{x}10^{-10}$ $g^{1/2}$ $cm^{3/2}$ s^{-1}). Independent measurements of both the defect concentration using, for example, SIMS or Hall effect, and the integrated absorption coefficient using IR spectroscopy to determine *q* for that defect. If no independent measurement of the defect concentration is available, then one can assume that $q = e$, which introduces an uncertainty in the defect concentration of at least a factor of two.[36] Independent measurements of the hydrogen concentration for the $\beta\text{–}Ga_2O_3$ samples used in these experiments have not been made. However, recent calibrations of the hydrogen concentration in ZnO[37] and In_2O_3[38] have determined values for the effective charge q = ~0.27e in these cases. This value can be used to estimate the concentration of hydrogen introduced by hydrogenation. We also assume that the integrated absorption coefficient of a vibrational line is related to the integrated absorbance by,

$$\int \alpha(\sigma)d\sigma = \frac{1}{d\log_{10} e}\int A(\sigma)d\sigma, \qquad \textbf{Eq. (5.5.2)}$$

where $A(\sigma)$ is the absorbance at a particular wavenumber and d is the thickness of the sample (in cm). The β–Ga_2O_3 is optically biaxial, i.e., refractive index is different along each of the three dielectric axes. To simplify the calculation, an average "isotropic" refractive index of n = 1.88 is assumed. This approach leads to a calibration factor of,

$$\frac{\mu_{\mathrm{OH}}nc^2}{\pi q^2} = \frac{1.58 \times 10^{-24}\ \mathrm{g} \cdot 1.88 \cdot (2.998 \times 10^{10}\mathrm{cm/s})^2}{\pi \cdot (0.27 \cdot 4.803 \times 10^{-10}\mathrm{g}^{1/2}\mathrm{cm}^{3/2}\mathrm{s}^{-1})^2} = 5.1 \times 10^{16}\mathrm{cm}^{-1}.$$

The integrated absorbance of the 3437 cm^{-1} O-H line present in a β–Ga_2O_3 sample after hydrogenation at 900 °C (Fig. 5.3.1) is ~0.030 cm^{-1}. The β–Ga_2O_3 sample had a thickness of 0.680 mm. Therefore, the estimated concentration of hydrogen present in the hydrogenated sample given by,

$$\begin{aligned} \mathrm{N}_H &= (5.1 \times 10^{16}\ \mathrm{cm}^{-1})\int \alpha_{3437}(\sigma)d\sigma \\ &= (5.1 \times 10^{16}\ \mathrm{cm}^{-1})\frac{0.030\ \mathrm{cm}^{-1}}{\log_{10} e \cdot 0.068\ \mathrm{cm}} = 5.2 \times 10^{16}\ \mathrm{cm}^{-3}. \end{aligned} \qquad \textbf{Eq. (5.5.3)}$$

Since the [H] in the hydrogenated sample was ~5% of the [Sn], it would be difficult to detect changes in the free-carrier absorption due to hydrogen-related donors in competition with the free-carrier absorption due to the impurities present in the as-grown sample. Therefore, it is unclear whether the defect responsible for this O-H vibrational line contributes significantly to the *n*-type conductivity of the sample.

The first-principles calculations by Prof. Fowler clearly show that the most energetically favorable configuration for two weakly coupled H_i defects do not satisfy the polarization properties determined from experiment. The H_i is predicted to act as a shallow donor in this material, which means its production (decay) should result in an increase (decrease) in the free-carrier absorption. No such changes were observed in our experiments. Therefore, H_i is eliminated as a candidate for this defect.

The properties of the shifted $V_{Ga(1)}$ defect decorated with two hydrogen atoms, however, are consistent with the experimental data. The orientations of the O-H bonds in the crystal do not contribute to a transition moment along the [1 0 2] direction, which agrees with the polarized absorption results. Furthermore, the symmetric stretching mode for this defect does not change the electric dipole moment of this defect, meaning this mode would be invisible to IR spectroscopy. The transition moment angle of the allowed stretching mode with respect to the [0 1 0] axis of the crystal is predicted to be ~64°. This angle is qualitatively consistent with the experimental angle of 47±11°, i.e., the transition moment has a significant component along the direction perpendicular to the (-2 0 1) plane. The calculations by Varley and coworkers[23] predict that gallium vacancies complexed with a single hydrogen atom are thermally stable for anneals up to 700 or 800 °C, which is consistent with the thermal stability of the 2546 cm^{-1} line. Therefore, the 3437/2546 and 3438/2547 cm^{-1} lines are assigned to a $V_{Ga(1)}$-2H defect complex.

The thermal anneals at 100 and 250 °C of $\beta-Ga_2O_3$ samples that were hydrogenated or deuterated at 900 °C reveal two additional weak lines with frequencies of 3492/2584 and 3563/2633 cm^{-1}. These lines are not as thermally stable as the $V_{Ga(1)}$-2H defect and anneal away at 200 and 500 °C, respectively, which indicates that they originate from two different hydrogen-containing defects. The current experimental data do not permit us to draw conclusions about the number of hydrogens contained in these defects. In principle, this information could be determined from isochronal anneals of a H+D co-doped sample. However, the weak intensities of these lines relative to the 3437 and 2546 cm^{-1} lines could make such an experiment difficult. The four vibrational lines present in the hydrogenated sample after the 1050 °C anneal have the same polarization properties as the other O-H/O-D lines, which means they are likely to be stretching modes of other O-H defects. However, a definitive assignment is not possiblebecause the O-D isotopic partners have not been observed. As only a fraction of the deuterium present in the deuterated sample remains after the 1000 °C anneal, it could be difficult to produce large enough O-D isotopic partners that give a detectable signal.

The isochronal annealing experiments for both the hydrogenated and the deuterated β−Ga_2O_3 samples suggest that hydrogen may be trapped in the as-grown samples in a form that is invisible to IR spectroscopy. A semi-quantitative estimate of the concentration of hydrogen present in the as-grown β−Ga_2O_3 can be made from,

$$\mathrm{N}_H = (5.1 \times 10^{16}\ \mathrm{cm}^{-1})\left[\int \alpha_{3437}(\sigma)d\sigma + \int \alpha_{3438}(\sigma)d\sigma\right]. \qquad \textbf{Eq. (5.5.4)}$$

All of the hydrogen present in the as-grown β−Ga_2O_3 sample prior to deuteration is assumed to be released by the 1000 °C anneal. Using the integrated absorbances for the 3437 and 3438 cm^{-1} H-H and H-D lines after the 1000 °C anneal (Fig 5.3.13) of 0.0147 and 0.0017 cm^{-1}, respectively, N_H is estimated to be,

$$\mathrm{N}_H = (5.2 \times 10^{16}\ \mathrm{cm}^{-1}) \frac{[0.0147 + 0.0017]\ \mathrm{cm}^{-1}}{\log_{10} e \cdot 0.068\ \mathrm{cm}} = 2.8 \times 10^{16}\ \mathrm{cm}^{-3}. \qquad \textbf{Eq. (5.5.5)}$$

The obvious candidates for the source of the “invisible” hydrogen in β–Ga_2O_3 are H_O or H_2 molecules. As with the [H] in the hydrogenated samples, the [H] in the as-grown sample is much lower than the [Sn], making it difficult to detect changes in the free-carrier absorption due to hydrogen-related donors. The vibrational signature of a H_O defect occurs in the far IR spectral region where it can be obscured by either free-carrier or multiphonon absorption. The stretching motion of a homonuclear, diatomic molecule does not give rise to a change in its electric dipole moment. Consequently, its detection using IR spectroscopy is impossible, which explains why no vibrational signatures are detected in the absorbance spectra. Consequently, we cannot draw any conclusions about the identity of the defect that acts as a source of hydrogen in as grown β–Ga_2O_3.

5.6: Summary

The atomic composition, polarization properties, and thermal stability of various hydrogen centers found in hydrogenated β–Ga_2O_3 single crystals have been investigated using FTIR spectroscopy. The as-grown sample shows no O-H vibrational lines, but hydrogenating the sample at a temperature of 800 or 900 °C for 1 hour produces a strong vibrational line with a frequency of 3437.0 cm^{-1}. Isotopic-substitution experiments with pure D_2 and mixed H_2+D_2 isotopes suggest that the center responsible for this defect contains two weakly coupled, *equivalent* hydrogen atoms. Additional O-H lines produced after annealing the hydrogenated sample at 100, 250, and 1050 °C have the same polarization properties as the 3437 cm^{-1} line, which suggests that these lines might arise from the same general type of defect. A comparison of the experimental data for the polarization and thermal stability of the 3437 cm^{-1} line with microscopic models determined from first principles calculations leads to an assignment of this defect to a $V_{Ga(1)}$-2H complex. The as-grown samples seem to contain a source of hydrogen that is invisible to IR spectroscopy, which is dissociated by annealing the sample at 800 °C or above. Both molecular hydrogen and substitutional hydrogen are possible candidates for this source, but additional experiments would be necessary to elucidate the identity of this source.

Acknowledgement: I gratefully acknowledge Sigma Xi, the Scientific Research Honors Society, for partial support of this research through a Grant-in-Aid of Research.

5.7: References

1. M. Orita, *et al.* Deep-ultraviolet transparent conductive β-Ga_2O_3 thin films. *Appl. Phys. Lett.* **77**, 4166 (2000).

2. M. Higashiwaki, *et al.* Recent progress in Ga_2O_3 power devices. *Semicond. Sci. Technol.* **31**, 034001 (2016).

3. B. J. Baliga. Semiconductors for high-voltage, vertical channel field-effect transistors. *J. Appl. Phys.* **53**, 1759 (1982).

4. A. J. Green, *et al.* 3.8-MV/cm Breakdown Strength of MOVPE-Grown Sn-Doped β-Ga_2O_3 MOSFETs. *IEEE Electron Device Lett.* **37**, 902 (2016).

5. S.-D. Lee, *et al.* Thermal stability of single crystalline alpha gallium oxide films on sapphire substrates. *Phys. Status Solidi* **10**, 1592 (2013).

6. S. Geller. Crystal Structure of β-Ga_2O_3. *J. Chem. Phys.* **33**, 676 (1960).

7. J. Åhman, *et al.* A Reinvestigation of β-Gallium Oxide. *Acta Crystallogr. Sect. C* **52**, 1336 (1996).

8. H. Peelaers & C. G. Van De Walle. Doping of Ga_2O_3 with transition metals. *Phys. Rev. B* **94**, 195203 (2016).

9. Z. Galazka, *et al.* Czochralski growth and characterization of β-Ga_2O_3 single crystals. *Cryst. Res. Technol.* **45**, 1229 (2010).

10. Z. Galazka, *et al.* Scaling-Up of Bulk β-Ga_2O_3 Single Crystals by the Czochralski Method. *ECS J. Solid State Sci. Technol.* **6**, Q3007 (2017).

11. N. Ueda, *et al.* Synthesis and control of conductivity of ultraviolet transmitting β-Ga_2O_3 single crystals. *Appl. Phys. Lett.* **70**, 3561 (1997).

12. H. Aida, H. *et al.* Growth of β-Ga_2O_3 single crystals by the edge-defined, film fed growth method. *Jap. J. Appl. Phys.* **47**, 8506 (2008).

13. A. Kuramata, *et al.* High-quality β-Ga_2O_3 single crystals grown by edge-defined film-fed growth. *Jap. J. Appl. Phys.* **55**, 1202A2 (2016).

14. S. Stepanov, *et al.* Gallium Oxide: Properties and Applicataions - A Review. *Rev. Adv. Mater. Sci* **44**, 63 (2016).

15. Z. Hajnal, *et al.* Role of oxygen vacancy defect states in the *n*-type conduction of beta-Ga_2O_3. *J. Appl. Phys.* **86**, 3792 (1999).

16. J. B. Varley, *et al*. Oxygen vacancies and donor impurities in β-Ga_2O_3. *Appl. Phys. Lett.* **97**, 142106 (2010).

17. J. L. Lyons, *et al*. Carbon as a shallow donor in transparent conducting oxides. *Phys. Rev. Appl.* **2**, 1 (2014).

18. E. G. Villora, *et al.* Electrical conductivity and carrier concentration control in β-Ga_2O_3 by Si doping. *Appl. Phys. Lett.* **92**, 202120 (2008).

19. K. Iwaya, *et al*. Atomically resolved silicon donor states of β-Ga_2O_3. *Appl. Phys. Lett.* **98**, 142116 (2011).

20. N. T. Son, *et al.* Electronic properties of the residual donor in unintentionally doped β-Ga_2O_3. *J.Appl. Phys.* **120**, 235703 (2016).

21. S. Ahn, *et al*. Thermal Stability of Implanted or Plasma Explosed Deuterium in Single Crystal Ga_2O_3. *ECS J. Solid State Sci. Technol.* **6**, Q3026 (2017).

22. P. D. C. King, *et al*. Observation of shallow-donor muonium in Ga_2O_3: Evidence for hydrogen-induced conductivity. *Appl. Phys. Lett.* **96**, 062110 (2010).

23. J. B. Varley, *et al*. Hydrogenated cation vacancies in semiconducting oxides. *J. Phys. Condens. Matter* **23**, 334212 (2011).

24. E. Korhonen, *et al.* Electrical compensation by Ga vacancies in Ga_2O_3 thin films. *Appl. Phys. Lett.* **106**, 242103 (2015).

25. E. V. Lavrov, *et al.* Hydrogen-related defects in ZnO studied by infrared absorption spectroscopy. *Phys. Rev. B* **66**, 165205 (2002).

26. C. Sturm, *et al*. Dielectric tensor of monoclinic Ga_2O_3 single crystals in the spectral range 0.5-8.5 eV. *APL Mater.* **3**, 106106 (2015).

27. C. Sturm, *et al.* Dipole analysis of the dielectric function of color dispersive materials: Application to monoclinic Ga_2O_3. *Phys. Rev. B* **94**, 35148 (2016).

28. M. Schubert, *et al.* Anisotropy, phonon modes, and free charge carrier parameters in monoclinic β-gallium oxide single crystals. *Phys. Rev. B* **93**, 125209 (2016).

29. E. V. Lavrov, *et al.* Copper dihydrogen complex in ZnO. *Phys. Rev. B* **77,** 155209 (2008).

30. D. Bastin, *et al*. Metastable state of the $V_{Zn}H_2$ defect in ZnO. *Phys. Rev. B* **83**, 195210 (2011).

31. S. Koch, *et al.* Interplay between interstitial and substitutional hydrogen donors in ZnO. *Phys. Rev. B* **89**, 235203 (2014).

32. F. Herklotz, *et al*. Charge states of a hydrogen defect with a local vibrational mode at 3326 cm^{-1} in ZnO. *Phys. Rev. B* **82**, 115206 (2010).

33. B. N. J. Persson & R. Ryberg. Brownian motion and vibrational phase relaxation at surfaces: CO on Ni(111). *Phys. Rev. B* **32**, 3586 (1985).

34. F. Herklotz, *et al.* Infrared absorption on a complex comprising three equivalent hydrogen atoms in ZnO. *Phys. Rev. B* **92**, 155203 (2015).

35. M. Stavola, Vibrational Spectroscopy of Light Element Impurities in Semiconductors, Chapter 3 in Identification of Defects in Semiconductors (ed. M. Stavola), Vol. 51B in *Semiconductors and Semimetals* (Academic Press, Boston, 1999).

36. E. V. Lavrov, *et al.* Identification of two hydrogen donors in ZnO. *Phys. Rev. B* **79**, 165210 (2009).

37. W. Yin, *et al.* Hydrogen centers and the conductivity of In_2O_3 single crystals. *Phys. Rev. B* **91**, 075208 (2015).

Appendix A: MATLAB Program

The following program, which was written by Andrew Shapiro (Lehigh University, Class of 2016), splices together transmission vs. wavelength spectra across different spectral regions. The user selects the transmission spectra (in order of increasing wavelength, i.e., Si/Quartz/Quartz response is file #1, InSb/Quartz/Quartz is #2, etc.) and selects the cutoff wavelengths (in μm) for each setup. For example, the transmission spectrum for the InSb/Quartz/Quartz setup is cut off at 5,000 cm^{-1} and joined to the transmission spectrum for the InSb/Glob/KBr setup. Thus, a cutoff wavelength of 2.0 μm is entered for the InSb/Quartz/Quartz transmission vs. wavelength spectrum. After splicing together the transmission vs. wavelength spectra, the absorption coefficient across the entire spectral range (in m^{-1}) is calculated.

```
function absSet = Absorbance_Main()
    clear;
    close all;
    clc;

    absSet = Mode_CalculateAbsorbance();
end

function absSet = Mode_CalculateAbsorbance()

    numfiles = 1;

    while(true)
        display('How many files need to be spliced?');
        temp = input('Enter the number of files.  Press [ENTER] for default of 1: ');
        if isempty(temp)
            break;
        end
        if temp >= 1
            numfiles = temp;
            break;
        end
        display('Please enter an integer larger than 0');
    end

    fileSet = cell(numfiles, 2);
```

```
for i = 1:numfiles
    [file, path] = uigetfile('./*.prn', 'Input File');
    fullname = [path file];
    display(['File Selected: ' fullname]);
    cutoff = input('Enter cutoff wavelength. Press [ENTER] for no cutoff: ');
    if isempty(cutoff)
        cutoff = inf;
    end
    fileSet(i, :) = {fullname cutoff};
end

params.d = input('What is the thickness of the sample (mm): ') / 1000;
params.n = input('What is the refractive index: ');
params.k = input('What is the extinction coefficient: ');
params.shift = input('Automatically shift data? (Y/N): ', 's');

switch(params.shift)
    case 'Y'
        params.zero = input('Which file would you like to center? ');
    otherwise
end

display('Reading Files...');
rawSets = FileIO('read', fileSet, 0);
display('DONE!');

display('Splicing Data...');
dataSet = spliceData(rawSets, params.shift, params.zero);
display('DONE!');

display('Calculating Absorbance Coefficient...');
absSet = calculateAbsorbance(dataSet, params, 'linear');
display('DONE!');

fig_thru = figure();plot(dataSet.x, dataSet.y);title('Transmission');
fig_abs = figure();plot(absSet.x, absSet.y);title('Absorption Coefficient');
fig_log = figure();loglog(absSet.x, absSet.y);title('LogLog Absorption Coefficient');

[fout, pout] = uiputfile('*./.prn', 'Output Trans File');
fileout = [pout fout];
FileIO('write', dataSet, fileout);
[fout, pout] = uiputfile('*./.prn', 'Output Abs File');
fileout = [pout fout];
FileIO('write', absSet, fileout);

fit = input('Would you like to fit the data? (Y/N): ', 's');
switch fit
    case 'Y'
        l_start = input('Input starting wavelength: ');
        l_end = input('Input ending wavelength: ');

        display('Selecting Region...');
        x_start = find(absSet.x >= l_start, 1);
```

```
            x_end = find(absSet.x <= l_end, 1, 'last');

            fitSet.x = log10(absSet.x(x_start:x_end));
            fitSet.y = log10(absSet.y(x_start:x_end));

            figure();plot(fitSet.x, fitSet.y);title('Selected Data To Fit');
            coeff = polyfit(fitSet.x, fitSet.y, 1);
            r_mat = corrcoef(fitSet.x, fitSet.y);
            display(sprintf('Exponent: %0.5f, Fit Factor: %0.5f, R^2: %0.5f\n', coeff(1), 10 ^ coeff(2),
r_mat(2)^2));

            calcSet.x = absSet.x(x_start:x_end);
            calcSet.y = 10 ^ coeff(2) * calcSet.x .^ coeff(1);
            figure(fig_abs);hold;plot(calcSet.x, calcSet.y);hold;
        otherwise
    end
end

function dataSet = spliceData(rawSets, shift, zero)
    offset = 0;
    x_full = [];
    y_full = [];
    start = 0;
    for i = 1:size(rawSets, 2)
        cutoff = rawSets(i).cutoff;
        i_start = find(rawSets(i).x >= start, 1, 'first');
        i_end = find(rawSets(i).x < cutoff, 1, 'last');
        x_temp = rawSets(i).x(i_start:i_end);
        y_temp = rawSets(i).y(i_start:i_end);

        switch shift
            case 'Y'
                s = 0;
                if(i ~= 1)
                    x_fit_full = x_full(max(1, end - 100):end);
                    y_fit_full = y_full(max(1, end - 100):end);
                    x_fit_temp = x_temp(1:min(end, 100));
                    y_fit_temp = y_temp(1:min(end, 100));

                    full_coef = polyfit(x_fit_full, y_fit_full, 1);
                    temp_coef = polyfit(x_fit_temp, y_fit_temp, 1);
                    diff_coef = full_coef - temp_coef;

                    s = diff_coef(1) * x_temp(1) + diff_coef(2);

                    if i == zero
                        offset = s;
                    end
                end
                display(sprintf('Set %i shifted: %0.5f\n', i, s));
                y_temp = y_temp + s;
            otherwise
        end
```

```
        x_full = [x_full x_temp];
        y_full = [y_full y_temp];
        start = cutoff;
    end
    dataSet.x = x_full;
    dataSet.y = y_full - offset;
    minY = min(dataSet.y);
    if minY < 0
        dataSet.y = dataSet.y - minY + eps;
    end
    dataSet.y(dataSet.y <= 0) = 0;
end

function absSet = calculateAbsorbance(dataSet, params, mode)
    switch mode
        case 'linear'
        otherwise
    end

    R = ((params.n - 1) ^ 2 + params.k ^ 2) / ((params.n + 1) ^ 2 + params.k ^ 2);
    A_2 = (1 - R) ^ 2 / (2 * R ^ 2);

    x = dataSet.x;
    y = dataSet.y * 0.01;

    x1 = sqrt(1 + (y / (A_2 * R)) .^ 2);
    x2 = (A_2 ./ y) .* (x1 - 1);
    a = -1 / params.d * log(x2);

    absSet.x = x;

    minA = min(a);
    if(minA < 0)
        a = a;% - minA + eps;
    end

    absSet.y = a;
end
------------------------------------------------------------------------------------------------------------------------
```

```
function rawSets = FileIO(rw, set, fileout)
    rawSets = [];

    switch rw
        case 'read'
            rawSets = FileRead(set);
        case 'write'
            FileWrite(set, fileout);
        otherwise
            display('Error - Unknown file interaction mode');
            exit();
    end
end

function FileWrite(set, fileout)
    out = num2cell([set.x; set.y]);%thru should change based on set being entered
    fout = fopen(fileout, 'w');
    fprintf(fout, '%0.6f\t%0.3f\n', out{:});
    fclose(fout);
end

function rawSets = FileRead(set)
    rawSets = [];
    for i = 1:size(set, 1)
        temp = fscanf(fopen(set{i, 1}), '%f');
        temp = reshape(temp, 2, []);
        rawSets(i).cutoff = set{i, 2};
        rawSets(i).x = temp(1,:);
        rawSets(i).y = temp(2,:);
    end
    fclose('all');
end
```

```
function obj = getSettingsRoot()
    mlock;
    persistent settingsRoot

    if isempty(settingsRoot)
       settingsRoot = matlab.internal.createAndInitSettingsRoot();
    end

    obj = settingsRoot;
end
```

Philip M. Weiser – Curriculum Vitae

Education

LEHIGH UNIVERSITY, Bethlehem, PA — Aug 2012 – May 2017

Ph.D. in Physics — May 2017

M.S. in Electrical Engineering — May 2015

MORAVIAN COLLEGE, Bethlehem, PA — Aug 2008 – May 2012

B.S. in Physics and Chemistry (ACS certified)

Summa cum laude with Honors in Chemistry

Research Experience

LEHIGH UNIVERSITY, Bethlehem, PA — May 2013 – 2017

Graduate Research Assistant (Advisor: Prof. Michael J. Stavola) — PhD Research

Dissertation: "Studies of Hydrogen Defects and Free Carrier Absorption in Transparent Conducting Oxides using Fourier Transform Infrared Spectroscopy."

- Used FTIR spectroscopy with uniaxial stress to determine the symmetry and diffusivity of the interstitial-hydrogen shallow donor in cubic indium oxide.
- Studied atomic composition, thermal stability, and polarization properties of hydrogen centers in monoclinic gallium oxide.
- Developed experimental method to measure transmission spectra of materials in the near- and mid-infrared spectral regions quantitatively using an FTIR spectrometer.

Summer Research Assistant (Advisor: Prof. A. Peet Hickman) — June – July 2012

Used Generalized Atomic and Molecular Electronic Structure System (GAMESS) code to calculate the approximate potential energy curves of a NaK molecule with a perturbing He atom for different inelastic scattering configurations.

MORAVIAN COLLEGE, Bethlehem, PA

Senior Honors Thesis (Advisor: Prof. O. Carl Salter) — Fall 2011 – Spring 2012

Modified chemistry department's Raman spectrometer to measure absorbance spectra of solid inorganic powders at cryogenic temperatures.

Student Opportunities for Academic Research — Spring 2011, Summer 2010

Examined decay kinetics of iron (III) thiosulfate complex and the effect of counter ions using OceanOptics UV/VIS spectrometer.

Leadership Experience

LEHIGH UNIVERSITY, Bethlehem, PA

Vice President, Graduate Student Senate (GSS)	May 2015 – May 2016
Graduate Representative, Graduate Research Committee	Aug 2015 – May 2016
GSS Physics Dept. Representative	May 2014 – May 2015
President, Physics Graduate Student Association	May 2014 – May 2015

MORAVIAN COLLEGE, Bethlehem, PA

Member	
American Chemical Society Student Chapter	Aug 2008 – May 2012
Society of Physics Students Student Chapter	Aug 2009 – May 2012
President, ACS Student Chapter	Aug 2009 – May 2011

Publications in Refereed Journals

1. P. Weiser, Y. Qin, W. Yin, M. Stavola, W. B. Fowler, and L. A. Boatner. "Symmetry and diffusivity of the interstitial hydrogen shallow-donor center in In_2O_3." Appl. Phys. Lett. **109**, 202105 (2016).

2. W. Yin, K. Smithe, P. Weiser, M. Stavola, W. B. Fowler, L. A. Boatner, S. Pearton, D. Hays, and S. Koch. "Hydrogen centers and the conductivity of In_2O_3 single crystals", Phys. Rev. B **91**, 075208 (2015).

3. R. F. Malenda, T. J. Price, J. Stevens, S. L. Uppalapati, A. Fragale, P. M. Weiser, A. Kuczala, D. Talbi, and A. P. Hickman. "Theoretical Calculations of Rotationally Inelastic Collisions of He with NaK ($A^1\Sigma^+$): Transfer of Population, Orientation, and Alignment", J. Chem. Phys. **142**, 224301 (2015).

Conference Presentations

"Vibrational properties of an O-H center in β-Ga_2O_3" W. B. Fowler, P. Weiser, M. Stavola. (Oral, W. B. Fowler) APS March Meeting 2017. New Orleans, LA.

"Interstitial hydrogen shallow donor and its diffusivity in In_2O_3 single crystals." P. Weiser, Y. Qin, W. Yin, W. B. Fowler, M. Stavola, and L. Boatner.

1. (Oral, M. Stavola) APS March Meeting 2017. New Orleans, LA.
2. (Oral, M. Stavola) The 7th International Symposium on Advanced Science and Technology of Silicon Materials (JSPS Si Symposium). Nov. 21-25, 2016, Kona, HI.

"Uniaxial stress studies of H centers in In_2O_3" P. Weiser, W. Yin, Y. Qin, M. Stavola, W. B. Fowler, and L. A. Boatner.

1. (Poster) Gordon Research Conference & Gordon Research Seminar in Defects in Semiconductors 2016. Colby-Sawyer College, New London, NH. Aug. 2016.
2. (Oral) APS March Meeting 2016, Baltimore, MD.

"Low frequency excitations of the 3326 cm^{-1} OH center in ZnO" P. Weiser, E. Farmer, M. Stavola, and W. B. Fowler.

1. (Poster) 28th International Conference in Defects in Semiconductors. Aalto University, Espoo, Finland, July 2015.
2. (Oral, M. Stavola) APS March Meeting 2015. San Antonio, TX.
3. (Poster, E. Farmer) APS March Meeting 2015. San Antonio, TX.
4. (Poster) 2014 Annual Meeting of the Mid-Atlantic Section of the APS. Pennsylvania State University, University Park, PA, Oct. 2014.
5. (Poster) Gordon Research Conference in Defects in Semiconductors 2014. Bentley College, Waltham, MA, Aug. 2014.

"OH centers and the conductivity of hydrogen-doped In_2O_3 single crystals." W. Yin, K. Smithe, P. Weiser, M. Stavola, W. B. Fowler, and L. A. Boatner.

1. (Poster, W. Yin) Gordon Research Conference on Defects in Semiconductors 2014. Bentley College, Waltham, MA. Aug. 2014.
2. (Oral, M. Stavola) APS March Meeting 2014. Denver, CO. March 2014.

"Effect of Counter Ions on Reaction of Iron (III) and Thiosulfate." P. Weiser, C. McCarl, O. C. Salter.

1. Undergraduate Research Poster Conference. Harrisburg, PA. March 2012.
2. 24th National Conference on Undergraduate Research. University of Montana, Missoula, MT, April 2010.

Teaching Experience

LEHIGH UNIVERSITY, Bethlehem, PA	Aug 2012 – present
Teaching Adjunct, PHY 031 (Introduction to Quantum Mechanics)	Spring 2016
Recitation Instructor, PHY 011 (Introductory Physics I) 4 appointments: Fall 2013, Spring 2014, Fall 2015, and Spring 2017	
Laboratory Instructor, PHY 012 (Introductory Physics I)	Fall 2012
Undergraduate Research Supervisor – Experimental Condensed Matter Physics	
Andrew Shapiro (Lehigh University)	Fall 2015/Spring 2016
Karla Villata (Mount Holyoke College)	Summer 2015
Ellen Farmer (Truman State University)	Summer 2014

MORAVIAN COLLEGE, Bethlehem, PA	
Academic Tutor	
CHEM 113/114 (General Chemistry I/II)	Fall 2009 – Spring 2012
PHYS 011/012 (Introductory Physics I/II)	Fall 2010 – Spring 2012
Laboratory/Teaching Assistant	
CHEM 332 (Physical Chemistry II)	Spring 2012
CHEM 113/114 (General Chemistry I/II)	Fall 2011 – Spring 2012
CHEM 108 (Fundamentals of Chemistry)	Spring 2010
BIOL 112 (General Zoology)	Spring 2009
BIOL 104 (Human Anatomy & Physiology II)	Spring 2009

Professional Organizations

Member	
Scientific Research Honors Society: Sigma Xi	Mar 2015 – present
Physics Honors Society: Sigma Pi Sigma	Mar 2011 – present
National Leadership Honors Society: Omicron Delta Kappa	Mar 2011 – present
American Physical Society (APS)	Oct 2014 – present
American Chemical Society (ACS)	Oct 2008 – Oct 2012
Secretary, Lehigh Valley Section of the ACS	Jan 2010 – Dec 2010

Industry Experience

PURITAN PRODUCTS, Bethlehem, PA	Jan – May 2012

Analytical Laboratory Technician (Supervisor: Stephanie Pinho)

Performed quality analysis on main products using wet chemical techniques and instrumental analysis.

SPECIALTY MINERALS INC., Bethlehem, PA	Summer 2011, Dec 2011- Jan 2012

Research Assistant (Supervisor: Dr. Sherman Cox)

Developed and standardized procedure to determine specific surface area of samples by measuring proton relaxation times of key product using NMR.

Awards and Fellowships

LEHIGH UNIVERSITY, Bethlehem, PA	
Best Student Poster, Gordon Research Seminar in Defects in Semiconductors 2016	Aug 2016
Sigma Xi Grant-In-Aid of Research	Dec 2015
Doctoral Travel Grant for Global Opportunities	July 2015
Sherman Fairchild Fellowship	Aug 2014 – Aug 2015
College of Arts and Sciences Dean's Fellowship	July – Aug 2014
Outstanding Teaching Assistant Award	Apr 2013

Level I Certificate of Participation, Teacher Development Series Spring 2013
Graduate Assistantship in Areas of National Need Fellowship Aug 2012 – Sept 2013

MORAVIAN COLLEGE, Bethlehem, PA
American Chemical Society Award Spring 2012
Stuart S. Kulp ScholarshipSpring 2012
ACS Leadership AwardJan 2010
Dean’s List (all semesters)Fall 2008 – Spring 2012

Public Outreach

HANOVER ELEMENTARY SCHOOL, Bethlehem, PA
Static Electricity and Magnetism Demonstration Apr 2014
Grades 3-5, 124 students
Amazing Air Demonstration Mar 2013
Grades 1-2, 82 students

FARMERSVILLE ELEMENTARY SCHOOL, Bethlehem, PA
Electrical Circuits Demonstration Oct 2012
Grade 3, 50 students

MARVINE ELEMENTARY SCHOOL, Bethlehem, PA
Annual Science Exploration Day Oct. 2010, 2009, and 2008
Chemistry and Physics Demonstrations “Cool Lights and Big Bangs”

Short Courses

1. “Strategic Planning.” ACS Leadership Development Feb 2012
   Lehigh Valley Section of the ACS, Bethlehem, PA.

2. “Engaging Colleagues in Dialogue.” ACS Leadership Development Jan 2010
   ACS Leadership Conference, Fort Worth, TX.

3. “Engaging and Motivating Volunteers.” ACS Leadership Development Jan 2010
   ACS Leadership Conference, Fort Worth, TX.
